

The high resolution $^{16}\text{O}(\gamma, \text{pn})^{14}\text{N}$
reaction at MAMI

EBERHARD KARLS
UNIVERSITÄT
TÜBINGEN



Dissertation

zur Erlangung des Grades eines Doktors
der Naturwissenschaften
der Fakultät für Mathematik und Physik
der Eberhard-Karls-Universität Tübingen

vorgelegt von
Federica Moschini
aus Cavalese (TN) Italien

2007

Tag der mündlichen Prüfung: 11.05.2007

Dekan: Prof. Dr. Nils Schopohl

1. Berichterstatter: Prof. Dr. Peter Grabmayr

2. Berichterstatter: Prof. Dr. Derek Branford

A mamma e papà

Abstract (English)

In this work measurements of the $^{16}\text{O}(\gamma, \text{NN})$ reactions, performed in 2002 at the MAMI facility in Mainz in collaboration with the Mainz, Glasgow and Edinburgh Universities are presented and discussed. Photon-induced two-nucleon knock-out reactions are very suitable for the study of the different NN interaction mechanisms inside nuclei. The aim of the experiment was to achieve a good enough missing energy resolution to be able to resolve the different final states of the residual nucleus. For this reason new Germanium detectors from Edinburgh University with an high intrinsic energy resolution were used for the detection of charged particles. The neutrons were detected in the Glasgow-Tübingen scintillator bars. The photons are produced via Bremsstrahlung from the electrons accelerated to 855 MeV in the mainzer microtron impinging on a 4 μm thick nickel radiator. The photon energy is indirectly measured from the position of the post-Bremsstrahlung electrons in the Glasgow tagging spectrometer which has an energy resolution of 2 MeV in the photon energy range 114-792 MeV. In order to reach a higher energy resolution the microscope, a tagging spectrometer with thinner scintillator fibres, was used in the energy range 170-220 MeV. Here a photon energy resolution of 0.6 MeV was achieved.

In this work results of the $^{16}\text{O}(\gamma, \text{pn})^{14}\text{N}$ reaction are presented. With the energy resolution of the experimental set-up it was not possible to distinguish individual excited states in the residual nucleus but it was possible to distinguish groups of states. The missing momentum distribution for the second and the third excited states combined of ^{14}N are shown. This distribution is comparable to previous missing momentum distributions from the $^{12}\text{C}(\gamma, \text{pn})^{10}\text{B}$ reaction presented in Ref. [73, 74], confirming that the two nucleons are emitted from a 1p-shell.

During the same beam-time the $^6\text{Li}(\gamma, \pi^+)^6\text{He}$ reaction was measured. This is a double coincidence experiment where the pions were detected in the Germanium array and the photons in the microscope. With this measurement it was possible to resolve separate excited states in the residual nucleus. Population of the ground and first excited states of ^6He was observed. The differential cross section for this reaction is presented and compared to previous results and to theoretical calculations.

Abstract (Deutsch)

Das Experiment zur Untersuchung der Reaktion $^{16}\text{O}(\gamma, \text{NN})$ wurde 2002 am MAMI, Mainz, in Kooperation mit den Universitäten Mainz, Glasgow und Edinburgh durchgeführt. Die Untersuchung der beide Reaktionskanäle pn und pp mit reellen Photonen kann weitergehende Einsicht in den komplexen Mechanismus der Nukleon-Nukleon Interaktion bringen. Das Ziel des Experiments war eine hohe Energieauflösung, 2 MeV, zu erreichen, um die Zustände des Restkerns aufzulösen.

Um diesen Zweck zu erfüllen, wurden neue hochauflösende Germanium Detektoren der Universität Edinburgh, für den Nachweis geladener Teilchen, eingesetzt in Kombination mit den "Glasgow-Tübingen Szintillator-Detektoren" zum Neutronennachweis. Die Photonen wurden durch Bremsstrahlung erzeugt. Dazu wurde der MAMI Elektronenstrahl (855 MeV) auf eine 4 μm dicke Ni-Folie gerichtet. Die Photonenenergie wurde indirekt über die Messung der gestreuten Elektronen im "Glasgow tagging Spektrometer" bestimmt. Die Energieauflösung des Photons im Bereich von 114 bis 792 MeV war 2 MeV. Um die hohe Auflösung zu erreichen, wurde ein zweites tagging Spektrometer, "microscope", das aus dünneren Szintillatoren besteht, für Photonenenergie im Bereich 170-220 MeV angeschaltet. Hier ist die Energieauflösung für das Photon 0.6 MeV.

In dieser Arbeit werden Ergebnisse für die $^{16}\text{O}(\gamma, \text{pn})^{14}\text{N}$ Reaktion präsentiert. Mit der Energieauflösung dieses Experiments konnten Gruppen von Zuständen des ^{14}N -Kerns unterscheiden werden. Dazu wird die missing momentum Verteilung der angeregten Zustände 3.95 MeV und 7.03 MeV des ^{14}N dargestellt. Diese Verteilungen könnten die Ergebnisse eines früheren Experiments zur Reaktion $^{12}\text{C}(\gamma, \text{pn})^{10}\text{B}$ [73, 74] bestätigen.

Parallel zu der $^{16}\text{O}(\gamma, \text{NN})$ Messung wurde auch die Reaktion $^6\text{Li}(\gamma, \pi^+)^6\text{He}$ gemessen. Diese Messung war eine zweifache Koinzidenz, bei der die Pionen im Germanium-Detektor und die Photonen im microscope nachgewiesen wurden. Bei dieser Messung konnten der Grundzustand und der erste angeregte Zustand identifiziert werden. Die Ergebnisse werden sowohl mit früheren Messungen als auch mit theoretischen Rechnungen verglichen.

Contents

1	Motivation	1
1.1	Introduction	1
1.2	NN correlations	3
1.3	Kinematic variables	5
1.4	Previous $^{16}\text{O}(\gamma, \text{NN})$ and $^{16}\text{O}(e, e'\text{NN})$ experiments	7
1.4.1	$^{16}\text{O}(\gamma, \text{pn})^{14}\text{N}$	8
1.4.2	$^{16}\text{O}(e, e'\text{pp})^{14}\text{C}$	11
1.4.3	$^{16}\text{O}(e, e'\text{pn})^{14}\text{N}$	12
2	Models for 2N emission	15
2.1	Nuclear Matter	16
2.1.1	Comparison with the exclusive $(e, e'\text{p})$ reaction	20
2.2	Pavia model	21
2.2.1	The hadron current operator	22
2.2.2	The initial state function	25
2.2.3	The final state function	26
2.2.4	Comparison with results from $^{16}\text{O}(e, e'\text{pp})^{14}\text{C}$ at MAMI	28
2.3	Gent model	29
2.3.1	Comparison with results from $^{16}\text{O}(e, e'\text{pp})^{14}\text{C}$ at MAMI	30

3	Experimental setup	33
3.1	The Microtron MAMI at Mainz	33
3.2	Photon tagging	36
3.2.1	The Glasgow-Mainz Tagging Spectrometer	36
3.2.2	The Tagger Microscope	37
3.3	Target	38
3.4	The solid state detectors	39
3.4.1	Double Sided Silicon Detectors	40
3.4.2	The Germanium hodoscope	41
3.5	The scintillation detectors	42
3.5.1	TOF and Veto counters	44
3.6	Trigger Electronics and Data acquisition	46
3.6.1	The trigger	46
3.6.2	TOF electronics	49
3.6.3	Data acquisition system	51
4	Detector calibration	53
4.1	Start detector	53
4.2	The Tagger	54
4.2.1	Tagging efficiency	54
4.2.2	Photon Time	55
4.2.3	Photon energy	57
4.3	DSSD	58
4.3.1	Pulse-height calibration	58
4.4	Germanium hodoscope	59
4.4.1	Linearity	59
4.4.2	Energy calibration	60
4.4.3	Particle identification	63
4.4.4	Test at the PSI	67

4.4.5	Proton detection efficiency	67
4.5	TOF	67
4.5.1	Walk correction	68
4.5.2	The t_0 calibration	69
4.5.3	Position calibration	70
4.5.4	The pulse-height calibration	73
4.5.5	The neutron detection efficiency	76
5	Data Analysis	79
5.1	Particle four-vectors	79
5.1.1	Photon	79
5.1.2	Proton	80
5.1.3	Neutron	83
5.2	Background subtraction	84
5.3	Calculation of the cross section	85
5.3.1	Experimental uncertainties	87
5.4	Photo-disintegration of ^2H	87
6	Results and discussion	93
6.1	$^2\text{H}(\gamma,\text{pn})$ reaction	93
6.2	$^{16}\text{O}(\gamma,\text{pn})$ ^{14}N reaction	94
6.2.1	Missing energy distribution	95
6.2.2	Missing momentum distribution	98
6.3	Comparison with $^{12}\text{C}(\gamma,\text{pn})^{10}\text{B}$ reaction	98
6.4	$^6\text{Li}(\gamma,\pi^+)^6\text{He}$ reaction	103
7	Conclusions and outlook	109

Chapter 1

Motivation

1.1 Introduction

Since the discovery of the nucleus by Rutherford, Geiger and Morsden in 1911, a description of the interaction between the constituents of the nucleus has been a matter of scientific research. One of the early nuclear models was introduced in the late thirties by Bohr [1] and Weizsäcker [2], namely the liquid drop model. In this model the nucleus is seen as an almost incompressible liquid droplet. Many liquid droplets of the same size compose the matter. This model was able to correlate binding energy and atomic number and to explain nuclear phenomena like fission, but it could not explain the experimental observation of the so called magic numbers, i.e. the atomic number of nuclei which have a local maximum in the binding energy curve.

Independent particle models (IPM) in which a single nucleon feels a mean field potential due to the other nucleons were implemented in the forties. In an IPM the Hamiltonian of the system in the Schrödinger equation is composed of the kinetic energy of one particle and a two-body potential, which could be a potential-well like in a Fermi gas model or a harmonic oscillator.

The nuclear shell model (SM) proposed by Mayer [4] and also Haxel, Jensen and Suess [3] was able to describe the magic numbers and the experimentally observed ground-state properties, like spin and parity, and excitations at low energies of the nuclei. In the SM the neutrons and the protons occupy energy levels, shells; they do not collide since their relative separation is of the order of their diameter, according to the Pauli principle. The mean field potential used is an effective central potential plus a spin-orbit potential.

From nucleon-nucleon scattering experiments it was possible to learn about the interaction of free nucleons but not of a bound system. Realistic potentials created by fitting these data can be used in a SM calculation, namely a Hartree-Fock (HF) calculation. Nowadays several realistic potentials describing the scattering data are

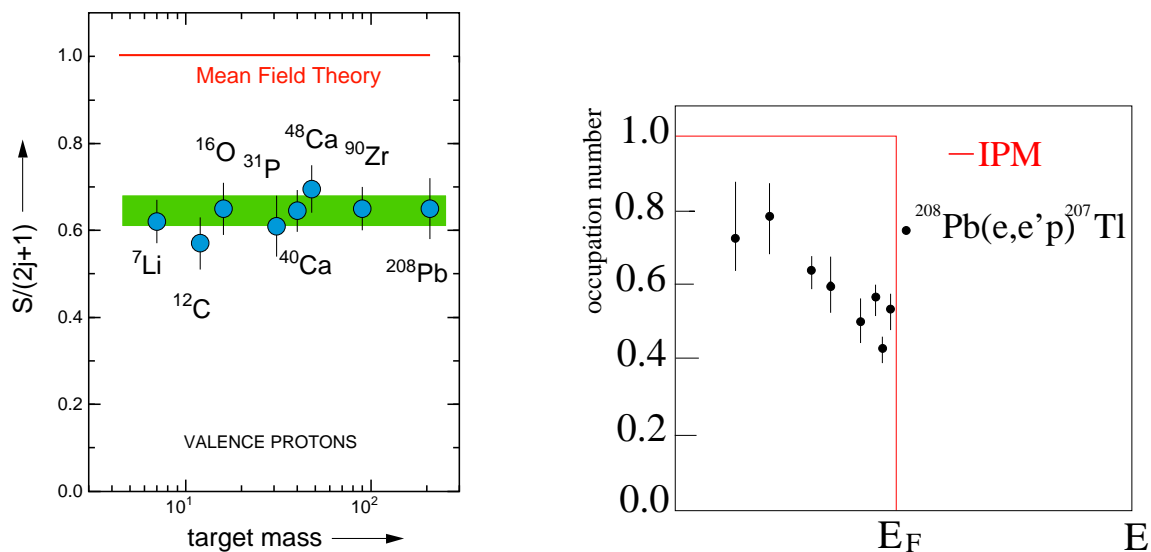


Figure 1.1: Left panel: strength for valence orbitals observed in $(e,e'p)$ experiments performed at NIKHEF [6, 7]. Right panel: Occupation number for several orbits in ^{208}Pb observed in $(e,e'p)$ experiments performed at NIKHEF [8]. The red line is the result of a pure mean field calculation.

available. The binding energy per nucleon obtained in a HF calculation with realistic potential for the nuclear matter [5] turned out to be positive, i.e. no bound system is created. This inability to describe a bound system arises from the interaction between two individual nucleons at short relative separation, needed in order to realistically reproduce the behaviour of the NN dynamics in a nucleus. Recently with the advent of new experimental methods such as the detection of one nucleon emitted through electron-scattering, the importance of the NN correlations became evident when looking at the experimental results, i.e. the spectroscopic strength of the valence orbitals for the knock-out of one proton from nuclei with $A > 4$ [6]. In Fig. 1.1, left panel, we see that the strength for some closed shell nuclei from $A=7$ to $A=208$ is around 65% of that predicted by an independent particle model. Furthermore, one can look at experimental observation of the occupation number for the closed shell of Pb, right panel. The data points lie under the full occupation line (occupation number = 1) below the Fermi level predicted from the IPM. The data points show a depletion of the occupation number of about 25% for the low energy shells; for states with energies close to the Fermi level the depletion is even bigger. The lack of strength below the Fermi level proves the occupation of nucleon states above the Fermi level due to high momenta caused by mutual interactions of NN pairs at short distances.

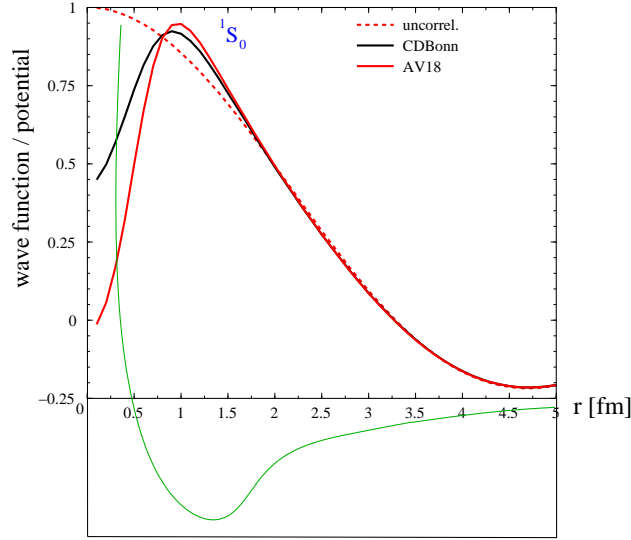


Figure 1.2: Relative wave function for the 1S_0 partial wave [9]. The uncorrelated wave function (dashed line) reaches the maximum amplitude at the zero NN separation. The different reduction of the wave function for the different potentials is due to the fact that CDBonn (black) is a non-local potential, while the AV18 (red) is a local one. The green curve is a sketch of the NN potential.

1.2 NN correlations

The effect of NN correlations can be better understood theoretically by looking at the relative wave function of the NN system, which represents the two nucleons in the bound system (finite or infinite such as nuclear matter). In Fig. 1.2 a recent calculation [9] of the two nucleon wave function for a infinite bound system for the partial wave 1S_0 is shown. If the two nucleons are considered as not-interacting with each other the relative wave function is the uncorrelated one, the dashed red line, where an amplitude of 1 is observed for zero relative separation. The correlated wave function is created by introducing an effective 2-body interaction, the G matrix, in the Hamiltonian of the system, a Bruckner-Hartree-Fock (BHF) calculation is performed. The amplitude of the relative wave function for the correlated pair is now reduced for small relative separation, as shown by the solid black and red lines, were two different realistic NN potentials were used for the calculation. This dip reflects the repulsive core of the NN potential, the green line sketched in Fig. 1.2, at a relative separation smaller then 0.5 fm. Due to the uncertainty principle, two nucleons, which are at a short relative separation can have high relative momentum. This is reflected by the so called short range correlations (SRC) which are part of the interaction that has been neglected in the SM.

In order to investigate NN interactions the most suitable probe is an electromagnetic

one, i.e. a virtual or a real photon. There are several advantages in using this type of probe. The initial state interaction is well known (QED) so that distortion effects of the incident projectile can easily be calculated. Moreover with the improvement of continuous-wave electron accelerators comprehensive measurements can be taken. The main difference between virtual and real photon is the nature of the probe. The cross section for the virtual photon has a longitudinal and a transverse response, while for the real photon only the transverse part contributes. The experiments with virtual photon have the advantage of the flexibility in the choice of the kinematics since the momentum of the photon can be varied independently to its energy since the mass is non zero. On the other hand, in experiments with virtual photons, spectrometers have to be used for the detection of the scattered electrons; these have usually a small solid angle and small momentum acceptance. With real photon detectors with a wider angular acceptance and energy range can be employed.

The possible experiments that one can perform are studies of:

- the exclusive (e,e') reaction, where only the out-going electron is detected and the emitted particles and the residual nucleus state are extracted via kinematical considerations,
- the exclusive $(e,e'N)$ and (γ,N) reaction where the emitted particles involved are detected,
- the inclusive $(e,e'N)$ and (γ,N) experiment where it is possible that the detected nucleon is coupled to a second nucleon, not detected, which is also ejected due to their high relative momentum and therefore the residual nucleus is left in a high excited state,
- the exclusive $(e,e'NN)$ and (γ,NN) where the second emitted nucleon is detected and the residual nucleus is left in either the ground state (g.s.) or an excited energy states.

The exclusive two-nucleon emission reaction is good for the study of the final state interactions since the residual nucleus is left in a known and quite easily calculable state. Moreover in a plane wave impulse approximation (PWIA) where the two emitted nucleons are the only active part of the reaction with the $A-2$ nucleus acting as a spectator, the initial quantum numbers of the NN pair coupled to the probe are the same quantum numbers of the residual nucleus in the final state from conservation of the quantum numbers.

For two-nucleon emission SRC is not the only mechanism by which the two nucleons can be ejected. Other processes can take place such as interaction with meson exchange currents (MEC) and the virtual excitation of the nucleons to a Δ , the isobar current (IC). In MEC the photon either interacts with a meson that is exchanged between the two nucleons (pion-in-flight) or the photon is absorbed by one nucleon that exchanges a pion with the correlated nucleon (pion seagull). Two types

of processes contribute to the Δ -isobar current: either the nucleon is excited into a Δ by photon absorption and it subsequently decays by exchanging a meson or the nucleon is first excited to a virtual Δ by meson exchange with a second nucleon and then de-excites by photon absorption. There can be also final state interactions (FSI) which include the interaction of an ejected nucleon with the residual nucleus or the mutual interaction between the two out-going nucleons. Three-body interaction mechanisms can also contribute to the cross-section. However it has been shown that their contribution is smaller than 1/3 of the total cross section for low photon energies and it can be neglected at high energy [10]. In Fig. 1.3 a sketch of the above mechanisms is drawn.

The investigation of the four types of reactions is very important in order to disentangle the different NN interaction mechanisms. For example in the emission of two protons the MECs are almost negligible. In some special kinematics, see section 1.4.2, the $(e, e'pp)$ reaction is the most suitable to study the SRCs.

1.3 Kinematic variables

In a two-nucleon knockout reaction using real photons the known observables are the directly measured four-momenta of the two outgoing nucleons and the four-momentum of the photon. The latter is calculated from the difference of the ingoing electron and the scattered electron after the bremsstrahlung, as it will be explained in section 3.2. The momentum of the photon, \vec{k} , has the absolute value of its energy, E_γ , and in our reference system its direction of motion is along the z-axis. In Fig. 1.4 a schematic drawing of the kinematical variables for a two-nucleon knock-out experiment is shown. The momenta of the outgoing nucleons are labelled \vec{p}'_i , $i = 1$ or 2 . The angles γ_1 and γ_2 are the polar angles of the outgoing nucleons with respect to the photon axis, i.e. the polar axis; Φ_1 and Φ_2 are the respective azimuthal angles. From the above observables we can reconstruct the missing momentum, which is the momentum not seen in the detectors:

$$\vec{p}_m = \vec{k} - \sum \vec{p}'_i \quad (1.1)$$

Correspondingly the missing energy (non-relativistic) is defined:

$$E_m = E_\gamma - \sum T'_i - T_{rec} = Q - E_x \quad (1.2)$$

where Q is the energy threshold to emit the nucleons, E_x is the excitation energy of the recoil nucleus of mass M_{rec} , T'_i are the kinetic energies of the outgoing nucleons and T_{rec} is the kinetic energy of the recoil nucleus which is calculated from its momentum, which for exclusive two-nucleon knockout corresponds to the missing

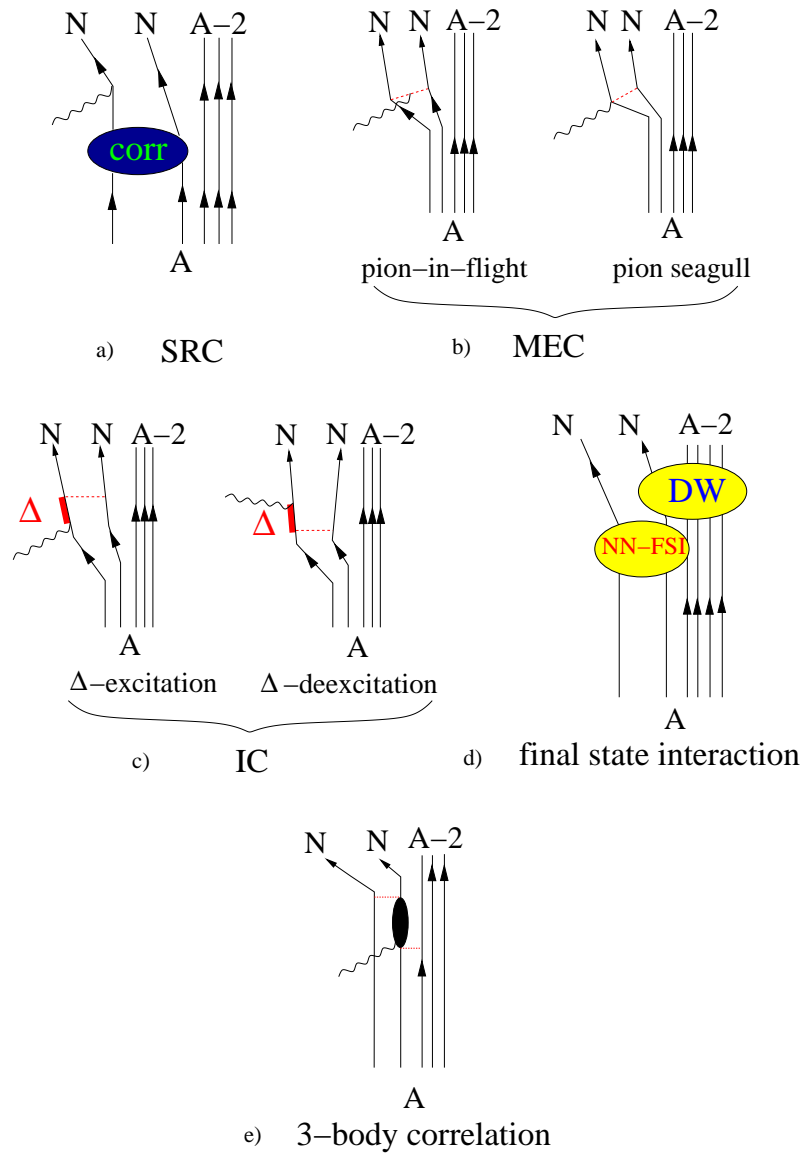


Figure 1.3: Possible 2N emission mechanisms: a) absorption of the gamma on a nucleon that is correlated with another one; b) absorption on a meson that is exchanged between 2N (MEC); c) a nucleon and a Δ interact via photon (IC); d) interaction between the two nucleons after one has absorbed the photon (FSI); e) absorption on a three-body correlation, where the bold ellipse represents anything except a nucleon.

momentum:

$$T_{rec} = \sqrt{p_m^2 + M_{rec}^2} - M_{rec}. \quad (1.3)$$

In PWIA the missing momentum is opposite to the c.m. momentum of the two initially nucleons coupled to the photon, because the target was at rest before the

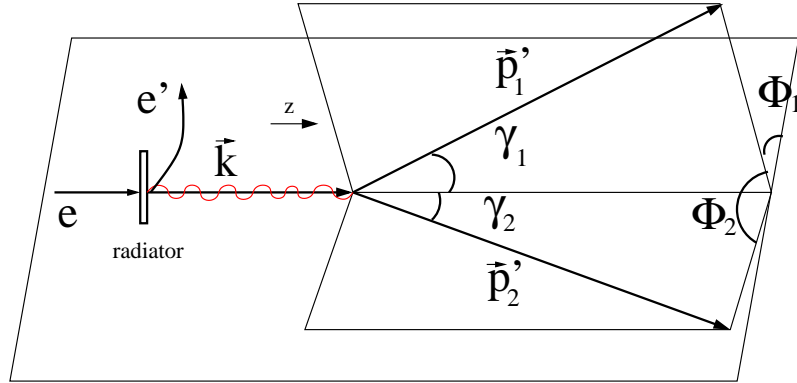


Figure 1.4: Schematic drawing of the kinematical variables.

interaction:

$$\vec{P}_{pair} = \vec{p}'_1 + \vec{p}'_2 = -\vec{p}_m$$

The short-range correlations are related to the relative momentum of the initial pair of nucleons: $\vec{p}_{rel} = 1/2 (\vec{p}_1 - \vec{p}_2)$. Unfortunately, \vec{p}_{rel} can not be determined unambiguously from the measured final momenta since \vec{p}'_1 and \vec{p}'_2 depend on the absorption mechanism of the photon.

1.4 Previous $^{16}\text{O}(\gamma, \text{NN})$ and $^{16}\text{O}(\text{e}, \text{e}'\text{NN})$ experiments

Among all the possible many-body systems ^{16}O is a good candidate to be used as a target for a two-nucleon emission experiment. The use of H_2O and D_2O make such targets relatively easy to handle as there is no need of a cryo-target. Also, the energy separation of the excited states in the recoil nucleus is relatively large so that with high resolution experiments it is possible to resolve the different final states. This is important in order to learn about the state of the NN pair coupled to the photon, as explained in section 1.2. As one can see from Fig. 1.5 for the (γ, pp) reaction there is a 7 MeV spacing between the g.s. and the first excited state, while between the other excited states and also for the (γ, pn) reaction the minimum spacing between the states is about 2 MeV. In the past years several two-nucleon knock-out experiments, using both virtual and real photons, have been performed. In this section I will briefly present the results and a comparison with some theoretical calculation in order to explain the reason for the present experiment. The $(\text{e}, \text{e}'\text{NN})$ reactions have been investigated in the A1 hall at MAMI [15], in Mainz; which provides the only possibility in the world to use three high resolution spectrometers in coincidence. The kinematics investigated were the so called super-parallel kinematics, where the

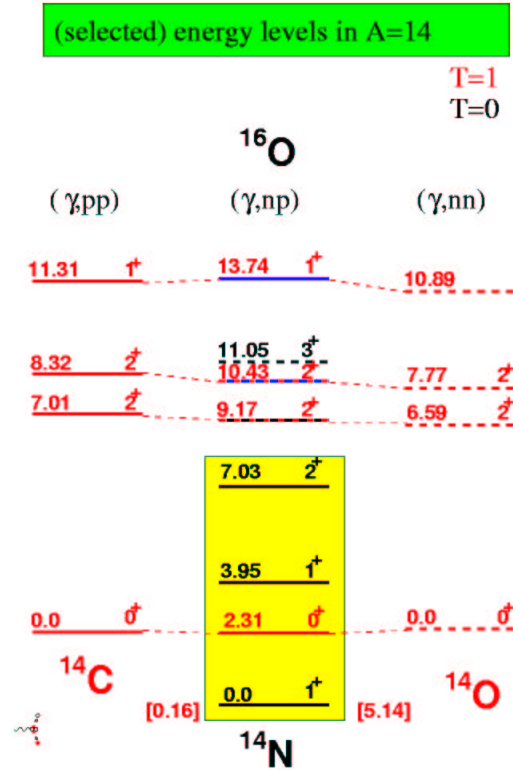


Figure 1.5: Selected energy levels of the residual nucleus for the $^{16}\text{O}(\gamma,NN)$ reactions.

two outgoing nucleons are emitted parallel and antiparallel to the momentum transfer, i.e. $\gamma_1 = 0$ and $\gamma_2 = \pi$. In such kinematical conditions contributions from IC are completely negligible in the pp channel and are reduced in the pn channel, as explained in details in section 2.2. Moreover with the three spectrometers it is possible to achieve a high energy resolution in order to resolve the different final states of the recoil nucleus. This is also an intention of the present experiment.

1.4.1 $^{16}\text{O}(\gamma,pn)^{14}\text{N}$

In the early nineties a high resolution $^{16}\text{O}(\gamma,pn)^{14}\text{N}$ experiment was performed at the tagged-photon facility at the Max-lab accelerator in Lund [16]. The photon energy was around 72 MeV and the 1.5 MeV resolution in missing energy was sufficient to resolve separate final states in the residual nucleus. The principal aim of the experiment was to determine the quantum numbers of the pn pair at the instant of photon absorption [17]. In PWIA the quantum number of the pn pair coupled to the photon are equal to the quantum number of the A-2 nucleus as already mentioned in section 1.2, since the ^{16}O system in its g.s. has isospin T=0

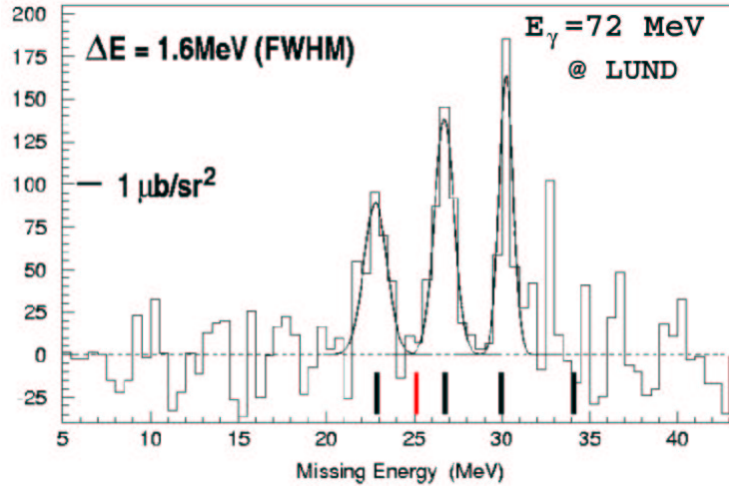


Figure 1.6: Missing energy distribution for the $^{16}\text{O}(\gamma, \text{pn})^{14}\text{N}$ experiment in Lund [17]. The g.s., the second excited state and the third excited state are strong populated.

and $J^\pi=0^+$, where J is the angular momentum and π the parity. In Fig. 1.6, where the missing energy distribution is shown, it is possible to distinguish the ground state, the 3.95 MeV state and the 7.03 MeV state.

Gaussian functions were fitted to the peaks in order to obtain the cross section strength. In Table 1.1 the first column lists the measured values as in ref. [17]. Since the detector system did not cover the entire phase space the values are corrected for this using a Monte Carlo simulation. The g.s. and the second excited state, both 1^+ , are populated indicating that the absorbed photon mainly couples to $L = 0$ and $L = 2$ pn pairs, where L represents the total orbital angular momentum of the pair, since the g.s. is mainly reached by $L = 2$ transfer and the second excited state by $L = 0$ [18]. The 2.31 MeV state is populated with a strength of less than 5% relative to its neighbour state with a confidence limit of 1σ . This means that the absorption probability on a pn pair in a 1S_0 state, i.e isospin triplet ($T=1$) and $J^\pi = 0^+$, is 5% smaller than the probability of absorption on a pair in a 3S_1 state, which is an isospin singlet ($T=0$) like the ground and the second excited state. This suggests that the photon absorption on a pn pair in an isospin triplet state play a minor role compared to the absorption on a pn pair in a deuteron state supporting the validity of the quasi-deuteron model. Calculations of the cross section based on a shell model [39], which do not include the predominance of the 3S_1 state also shows a little strength for the 2.31 MeV state; the third column of the Table 1.1 lists the calculated values. The 7.03 MeV, 2^+ , state is measured to be strongly populated which is in contrast with the theoretical calculation, which predicted the cross section to be much lower.

State	$(d^2\sigma/d\Omega_p d\Omega_n)_{meas}$ ($\mu b/sr^2$)	$(d^2\sigma/d\Omega_p d\Omega_n)_{calc}$ ($\mu b/sr^2$)
g.s.	1.4 ± 0.5	0.34
2.31 MeV	<0.1	0.09
3.95 MeV	1.7 ± 0.5	0.80
7.03 MeV	1.6 ± 0.4	0.15

Table 1.1: Cross sections value for the different final states of the $^{16}\text{O}(e,e'pn)^{14}\text{N}$ reaction measured at Lund [17]. The values are corrected for the phase space using a Monte Carlo simulation; the uncertainties are statistical. In the last column are reported the value for the calculation in a shell model framework [39].

Later in the nineties another high resolution $^{16}\text{O}(\gamma,pn)^{14}\text{N}$ experiment was realised at the Saskatchewan Accelerator Laboratory (SAL) in Canada [19] with photon energies from 98.5 MeV to 141 MeV. The aim of this experiment was, besides gaining knowledge on the MEC and SRC, to have more understanding of the photo-absorption mechanism on the pn pair. For this last aim the data were taken in quasi-free deuteron kinematics, i.e. proton and neutron were detected in the forward direction. In these kinematics the angular momentum transfer to the pn pair is predominantly $L=0$. As Cohen and Kurath [18] showed with their calculation of the coefficient of fractional percentage the g.s. is mainly reached with $L=2$ transfers, the 2.31 MeV state is pure $L=0$ transfers and the 3.95 MeV is mainly reached with $L=0$ transfers. The yield of the excitation energy are shown in Fig. 1.7. Only a peak at 3.9 MeV is visible. At around 20 MeV the continuum starts. The g.s. does not appear as expected since the kinematics favours the $L=2$ transfer. The peak is identified as the 3.95 MeV, 1^+ $T=0$, excited state. The 7.03, 2^+ $T=0$, and the 11.05 MeV, 3^+ $T=0$, states are predicted to be reached by pure $L=2$ transfer and in agreement with the prediction are not seen in the excitation energy spectrum. The 2.31 MeV, 0^+ $T=1$, state even if the angular momentum transfer is pure $L=0$ is not clearly distinguishable from the main peak. It could be that it is on the left shoulder of the peak. This result is interpreted as the photo-absorption probability on a pn pair in a $T=1$ state leading to the 2.31 MeV final state being less than 10% of the probability to go to the 3.95 MeV state.

The results of both experiments show that the photon almost does not couple with the pn pair in a $T=1$ state. Unfortunately for the Lund experiment the photon energy range was only 10 MeV, too low to obtain a missing momentum distribution and the momentum range was too small. For the SAL experiment the energy resolution was not high enough to really separate the first excited state, if populated, from the 3.95 MeV state. This is one of the reasons for the experiment described in this work. A new high resolution $^{16}\text{O}(\gamma,pn)^{14}\text{N}$ experiment could confirm the low population of the 2.31 MeV state and provide more information on the absorption mechanism and missing momentum distributions.

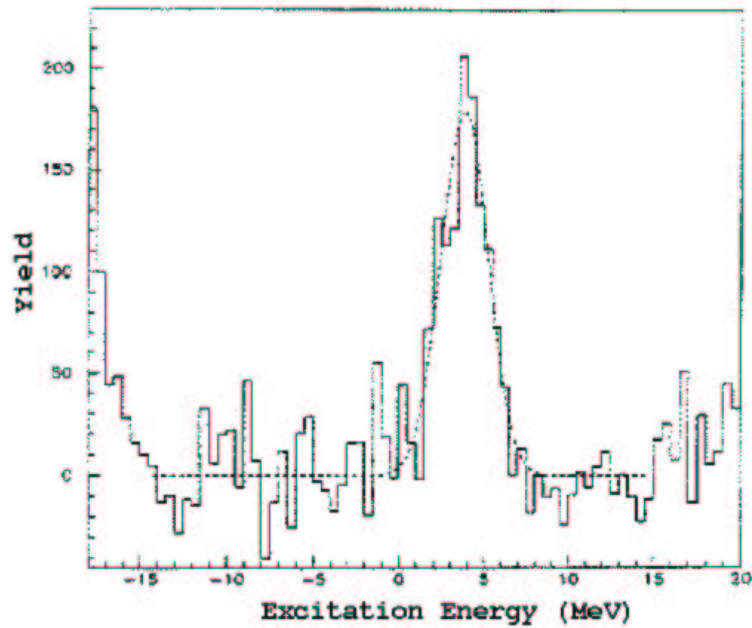


Figure 1.7: Excitation energy distribution for the $^{16}\text{O}(\gamma, \text{pn})^{14}\text{N}$ experiment at SAL. The peak centred at 3.9 MeV with FWHM 2.8 MeV is identified to be the 3.95 MeV ($1^+, 0$) state. The 2.31 MeV ($0^+, 1$) state could be present in the left shoulder of the main peak. The continuum starts at around 20 MeV.

1.4.2 $^{16}\text{O}(e, e'\text{pp})^{14}\text{C}$

The $^{16}\text{O}(e, e'\text{pp})^{14}\text{C}$ experiment was performed in the A1 hall at MAMI, in Mainz. The experiment was run in super-parallel kinematics [20] at an energy transfer $\omega = 215$ MeV and momentum transfer $|\vec{q}| = 316$ MeV/c. The proton emitted in the direction of the momentum transfer was detected in spectrometer A and the second proton in spectrometer C, while the scattered electron was measured in spectrometer B. The high resolution of the 3 spectrometers allowed the individual excited states in the residual ^{14}C nucleus to be resolved as shown in Fig. 1.8; the excitation energy resolution achieved was about 1 MeV. The data analysed were taken in a missing momentum range of -90 MeV/c to 90 MeV/c; the random coincidences have been subtracted and corrections for detector efficiencies taken into account. The g.s. is the strongest populated state which is opposite to its isobaric analog state, the 2.31 MeV in the pn channel.

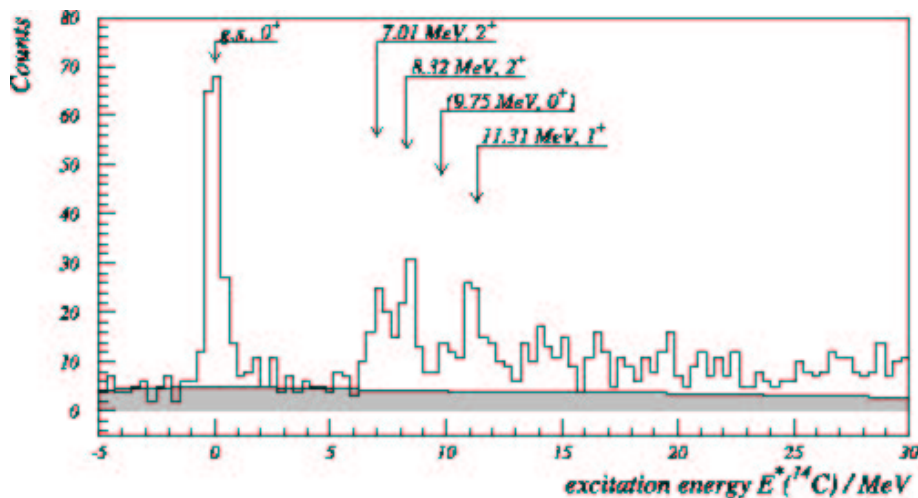


Figure 1.8: Cross section for the $^{16}\text{O}(e,e'pp)^{14}\text{C}$ reaction at MAMI [20] in super-parallel kinematics for $-90 \text{ MeV}/c \leq p_m \leq 90 \text{ MeV}/c$.

1.4.3 $^{16}\text{O}(e,e'pn)^{14}\text{N}$

The first high resolution $^{16}\text{O}(e,e'pn)^{14}\text{N}$ experiment was performed at the MAMI facility, in the A1 hall. Spectrometer B was used to detect the outgoing electron. The Tübingen-Glasgow TOF detectors were employed to detect the neutron and spectrometer A was used to detect the proton. Data were taken in the same kinematics as in the $^{16}\text{O}(e,e'pp)^{14}\text{C}$ experiment so a direct comparison could be made between results [21]. In Fig. 1.9 the excitation energy of the residual nucleus is shown. The energy resolution, $\leq 3 \text{ MeV}$ FWHM, was not good enough to resolve the individual excited states. In Fig. 1.9 we see a peak which covers the 2.31 MeV, the 3.95 MeV and the 7.03 MeV states, all three of which could contribute to the observed strength. The second strong peak centred around 11 MeV may correspond to excitation of states in the continuum. In contrast to the $(e,e'pp)$ measurement [20] there is no clear strength from the ground state in ^{14}N . Theoretical calculations [22, 23] suggest that the transitions to 3.95 MeV excited state give the greatest contribution of strength to the peak centred at around 4 MeV.

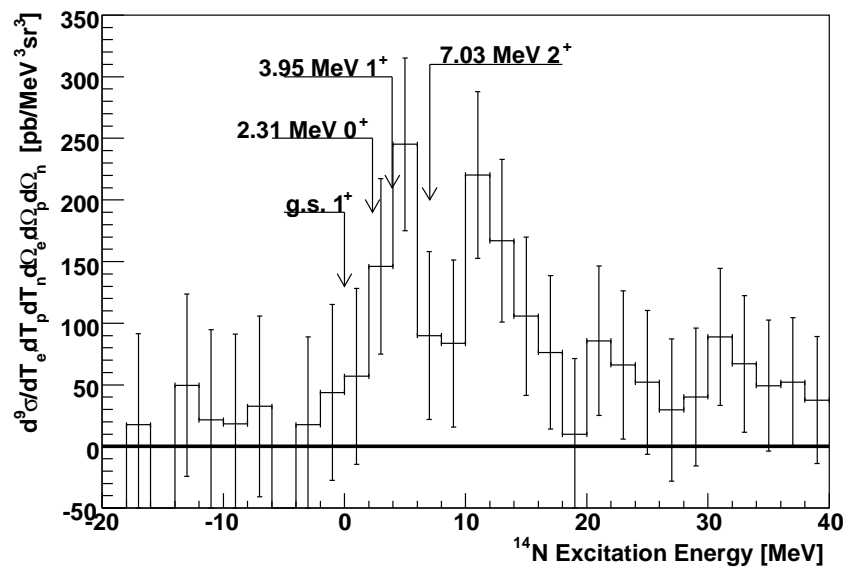


Figure 1.9: Cross section as function of the excitation energy for the $^{16}\text{O}(e, e'\text{pn})^{14}\text{N}$ experiment at MAMI [21] in the same kinematical conditions as in figure 1.8.

Chapter 2

Models for 2N emission

The cross section for the emission of two nucleons by an unpolarised real photon [24, 25] is calculated from the contraction of the lepton tensor, representing the electromagnetic probe, and the hadron tensor, representing the target and residual nucleus in the final state with the outgoing nucleons. By applying lepton and hadron current conservation and integrating over the total energy E'_2 of one of the two outgoing nucleons the cross section can be written as [24, 28]:

$$\frac{d^5\sigma}{dE'_1 d\Omega_1 d\Omega_2} = \frac{2\pi^2\alpha}{E_\gamma} \Omega_f f_{rec} W_T \quad (2.1)$$

where $\Omega_f = |\vec{p}'_1|E'_1|\vec{p}'_2|$ is the phase space factor and the recoil factor is:

$$f_{rec}^{-1} = 1 - \frac{E'_2}{E_{rec}} \frac{\vec{p}'_2 \cdot \vec{p}_{rec}}{|\vec{p}'_2|^2}. \quad (2.2)$$

The W_T is the pure transverse structure function which is a linear combination of the components of the hadron tensor $W^{\mu\nu}$ [24]. The hadron tensor is obtained from the Fourier transform of the transition matrix [24] S_{fi} :

$$S_{fi} = i e_T \frac{1}{\sqrt{2E_\gamma}} \epsilon_\lambda J \cdot (2\pi)^4 \delta^{(4)}(p' - p - k) \quad (2.3)$$

where e_T is the target charge, ϵ_λ the polarisation of the real photon with $\lambda = \pm 1$ as the real photon has only transverse polarisation and J is the four-vector of the target current. The components, J^μ , of the target current vector are the matrix elements of the charge-current density operator between the initial and the final nuclear states:

$$J^\mu(\vec{k}) = \int \langle \Psi_f | \hat{J}^\mu(\vec{r}) | \Psi_i \rangle e^{i\vec{k} \cdot \vec{r}} d\vec{r}. \quad (2.4)$$

The nuclear states $|\Psi\rangle$ are determined by solving the Schrödinger equation for the initial and for the final nuclear system where the Hamiltonian has the general form:

$$H = T_1 + T_2 + V_{12} + \mathcal{V}. \quad (2.5)$$

Here T_1 and T_2 are the kinetic energies of the two emitted nucleons, V_{12} represents the mutual interaction of the two nucleons and \mathcal{V} is a potential including some omitted interaction between each of the emitted nucleons and the residual nucleus. The structure of the mutual potential is derived from the experimental results of the free nucleon-nucleon scattering. Different realistic potentials are modelled to fit these data and are available to be used in the Hamiltonian of eq. 2.5.

The three-body potential V_{123} representing the interaction between three nucleons is either completely neglected or simplified via an average potential. Recent Green Function Monte Carlo calculations [29] including a three-body potential for nuclei up to $A=10$ have been carried out. The calculation of the binding energy showed a better agreement with the experimental values than the calculation without the three-body interactions. For heavier nuclei, $A=12$, experimental results of the $^{14}\text{C}(\gamma, ppN)$ reaction [10] are compared to calculations including the three-body potential. As already mentioned in section 1.2 the three-body force contribution is low for low photon energies and is negligible for higher photon energies. Since this result depends on the choice of the kinematics, more experiments must be carried out to get a general understanding of the importance of the three-body force for nuclei with $A>10$.

Even without the introduction of a three-body potential, the calculation of the exact solution of the Hamiltonian is a three body problem and therefore complicated. For this reason approximations are applied and several approaches to the problem are followed. The starting point to calculate the photo-absorption cross section is always the hadron current of eq. 2.4; different methods to calculate the hadron current, the initial and the final state are used from different theoretician groups. In this section I will start by introducing the NN interaction in nuclear matter, since due to translation invariant the calculations are simplified making it is a very good starting point to understand the pair behaviour in finite matter. The model used by the Pavia group [25, 27, 28] is briefly explained with a comparison to the data taken in Mainz presented in Ref [20]. A different model proposed by the Gent group [39, 40, 41], is also presented with differences to the Pavia model being discussed; a comparison with the same data is made.

2.1 Nuclear Matter

Nuclear matter (NM) is an infinite translation invariant system of interacting nucleons. In symmetric nuclear matter there is an equal number of protons and neutrons

and as an approximation the Coulomb interaction can be neglected. The translation invariance allows sophisticated many-body calculations making it easy and useful to study the nucleon-nucleon interaction in nuclear matter.

The Hamiltonian which describes the nuclear matter system is the same as in eq. 2.5. Also in NM a strong repulsive potential core causes the failure of standard perturbation methods [24]. Other approaches are necessary and thus in the last years the Self Consistent Green's Function (SCGF) method has been developed. Advantages of the SCGF approach is that the spectral function comes out naturally and the calculations can be performed at 0 and finite temperatures. The first is important for direct comparison to results of (e,e'p) experiments, as it will be reported in section 2.1.1, and the second for comparison with NM in astrophysics. The SCGF method of [42, 43, 44, 45] uses a diagrammatic approach, where the single particle Green's function is expanded in terms of diagrams. In a grand-canonical formulation the one-particle Green's function for real time t and imaginary time t' is written:

$$ig(\vec{x}t, \vec{x}'t') = Tr \left\{ \rho_G \mathcal{T} \left[\Psi(\vec{x}t) \Psi^\dagger(\vec{x}'t') \right] \right\}, \quad (2.6)$$

where \mathcal{T} is the time ordering operator acting on the Heisenberg product of creation and annihilation field operator $\Psi(\vec{x}t) = e^{itH} \Psi(\vec{x}) e^{-itH}$. \mathcal{T} puts the field operator with the biggest time on the left side. The statistical operator $\rho_G = \frac{1}{Z} e^{-\beta(H - \mu N)}$ contains the inverse temperature β the chemical potential μ and the operator counting the total number of particles N . Z is the normalisation factor. The N-particle Green's function is described in the same way, for example the two-particle Green's function reads:

$$ig_{II}(\vec{x}_1 t_1, \vec{x}_2 t_2; \vec{x}'_1 t'_1, \vec{x}'_2 t'_2) = Tr \left\{ \rho_G \mathcal{T} \left[\Psi(\vec{x}_1 t_1) \Psi(\vec{x}_2 t_2) \Psi^\dagger(\vec{x}'_1 t'_1) \Psi^\dagger(\vec{x}'_2 t'_2) \right] \right\}. \quad (2.7)$$

To determine the Green's function one can start from the equation of motion, which for the one-particle Green's function contains a two-body potential and a two-particle Green's function. The general rule is that the n-body propagator is correlated to the n+1 propagator. In a similar approximation the Green's function is expanded in terms of the free propagator $g^0(k, z_\nu)$, where $z_\nu = \frac{\pi\nu}{-i\beta} + \mu$ is the Matsubara frequency, and the two-body bare potential V ; the Feynmann diagrammatic representation is used. In Fig. 2.1 the diagrams for contributions to the first order are shown. Since at the second order the expansion in the diagrams involves already 10 possible diagrams an exact solution of the motion equation is impossible. A truncation of the diagrams is made by introducing the self-energy Σ . Now the equation of motion is a Dyson equation, diagrammatically represented in Fig. 2.2 (left panel), which binds the unperturbed propagator to the dressed propagator through the self-energy. By iteration, i.e. by substituting the right hand side of the Dyson equation in the full Green's function all the n-body terms are deduced.

The self-energy is calculated in ladder approximation, where all the particle-

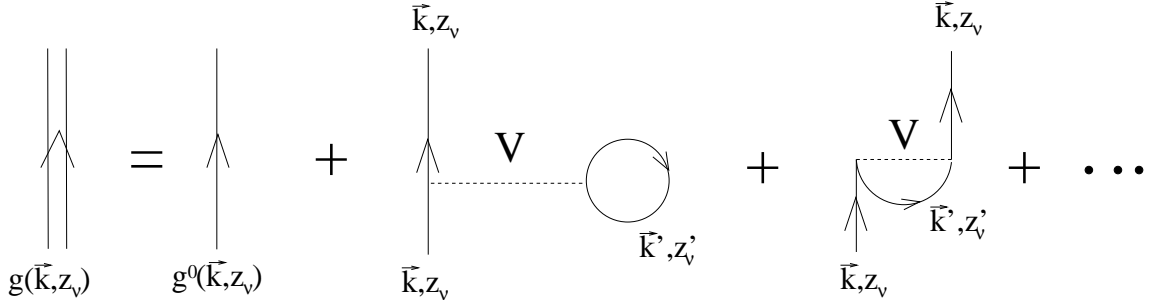


Figure 2.1: Feynmann diagrams for the 1st order expansion of the one particle Green's function. The single line represents the free propagator, the dashed line the bare potential.

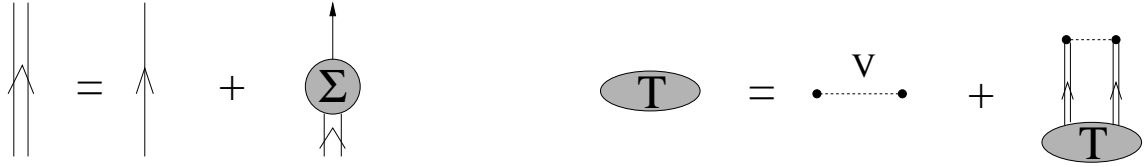


Figure 2.2: Left panel: Dyson equation for the single particle propagator, the free propagator (single line) and the self energy. Right panel: diagrammatic representation of the T matrix in ladder approximation. The effective interaction contains the bare potential (dashed line) and the iterative term which contains all the ladder diagrams.

particle and hole-hole scattering processes are taken into account and treated in the same way. The ladder self-energy involves the T matrix, that is an effective two-body interaction. The T matrix is the equivalent of the G-matrix in HF approximation, its diagram is shown in Fig. 2.2 (right panel). The one-particle Green's function can also be expressed in terms of a correlation function [43]:

$$\begin{aligned} g^>(\vec{x}t; \vec{x}'t') & \text{ if } t > t' \\ g^<(\vec{x}t; \vec{x}'t') & \text{ if } t < t' \end{aligned} \quad (2.8)$$

The Fourier transform of $g^<(\vec{x}t; \vec{x}'t')$ along the real time axis gives the probability to remove a nucleon with momentum \vec{k} at energy ω , and the Fourier transform of $g^>(\vec{x}t; \vec{x}'t')$ gives the probability to attach a nucleon, the sum of them is the single particle spectral function [43]:

$$S(\vec{k}, \omega) = g^>(\vec{k}, \omega) + g^<(\vec{k}, \omega) \quad (2.9)$$

By using the quasi periodicity condition $g(\vec{x}, t = 0; \vec{x}', t') = -e^{\beta\mu}g(\vec{x}, t = -i\beta; \vec{x}', t')$ the Fourier transformed correlation functions can be expressed as function of the

spectral function [43]

$$\begin{aligned} g^<(\vec{k}, \omega) &= f(\omega) S(\vec{k}, \omega) && \text{hole spectral function} \quad (t < t') \\ g^>(\vec{k}, \omega) &= (1 - f(\omega)) S(\vec{k}, \omega) && \text{particle spectral function} \quad (t > t'), \end{aligned} \quad (2.10)$$

where $f(\omega) = [e^{\beta(\omega - \mu)} + 1]^{-1}$ is the Fermi function. The Fourier coefficients of the imaginary time Green's function can be written [43]:

$$g(\vec{k}, z_\nu) = \int_{-\infty}^{+\infty} \frac{d\omega}{2\pi} \frac{S(\vec{k}, \omega)}{z_\nu - \omega}. \quad (2.11)$$

By replacing the Matsubara frequency with an imaginary number z and introducing a retarded propagator $g(\vec{k}, \omega + i\eta)$ the spectral function reads:

$$S(\vec{k}, \omega) = -2 \operatorname{Im} g(\vec{k}, \omega + i\eta). \quad (2.12)$$

The solution of the Dyson equation gives the perturbed Green's function as a function of the self-energy. If one inserts it in the retarded propagator one obtains the following expression for the single particle spectral function [43]:

$$S(\vec{k}, \omega) = \frac{-2 \operatorname{Im} \Sigma(\vec{k}, \omega + i\eta)}{\left[\omega - \frac{k^2}{2m} - \operatorname{Re} \Sigma(\vec{k}, \omega) \right]^2 + \left[\operatorname{Im} \Sigma(\vec{k}, \omega + i\eta) \right]^2} \quad (2.13)$$

Without the ω dependence the spectral function would be a Lorentzian. The upper term in eq. 2.13 is interpreted to be the spectral width of the function. For non-interacting particles like in HF approximation the spectral function would be a δ function centred at the value of the single particle energy, which depends on its momentum \vec{k} .

In order to compare the result of SCGF with the $(e, e'p)$ experiment, where finite nuclei are the target and a different energy region is investigated, the SCGF approach needs some modifications [45]. Eq. 2.13 is still valid but the self-energy is calculated in a different way; it becomes the sum of a non-interacting and a perturbation term, the two-hole-one-particle self-energy [45]:

$$\Sigma(\vec{k}, \omega) = \Sigma^{HF}(\vec{k}, \omega) + \Delta \Sigma^{2h1p}(\vec{k}, \omega + i\eta), \quad (2.14)$$

where the G-matrix replaces the T matrix in the $\Delta \Sigma^{2h1p}(\vec{k}, \omega + i\eta)$. Also here the ladder approximation is used with attention being paid to the pairing instability problem. It has been shown [46] that the ladder approximation method leads to pairing instability, meaning that complex eigenvalues appear in the ladder self-energy. To bypass the problem, the Green's function can be calculated at finite temperature,

since up to $T=5$ MeV the instability is localised in a small energy range [45]. The imaginary component of the ladder self-energy contains the imaginary part of the T matrix and the spectral function weighted by the Fermi function and the Bose function $b(\Omega) = \left[e^{\beta(\Omega-2\nu)} - 1 \right]^{-1}$. The real part of the ladder self-energy is the sum of a HF term and an energy dependent term.

For the comparison of the so calculated spectral function with the one extracted from (e,e'p) experiments the calculations were performed for an energy ω below the Fermi level or chemical potential [45] and at the lowest possible temperature, 2 MeV. The bare potential used is the CD-Bonn. The comparison can be done only when the data are taken at high missing momenta and energy since for the low range the spectral function is dominated by single particle wave functions, which have a different behaviour in finite nuclei than in infinite NM. Moreover in order to see an effect due to SRCs and long-range correlations one has to perform exclusive one-nucleon emission reactions where the residual nucleus is left in an high excitation energy state, i.e. high missing energy and high missing momentum (at least 250 MeV/c). Indeed, it has been demonstrated [11] that the exclusive (e,e'p) reaction at high missing momenta for the transition to the ground state of the residual nucleus, shows no signature of correlations. In reference [11] the missing momentum distribution for the $^{16}\text{O}(e,e'p)^{15}\text{N}$ reaction, leaving the ^{15}N in the g.s., from an exclusive experiment at MAMI [12] has been compared to HF calculations and calculations including a full correlated spectral function with long-range correlations, SRC and FSI. The data from 100 MeV/c missing momentum to 700 MeV/c can be fitted within a HF picture and even the inclusion of the correlations does not give any deviation from the mean field.

2.1.1 Comparison with the exclusive (e,e'p) reaction

Exclusive $^{12}\text{C}(e,e'p)$ reaction at high missing momenta and energy have been performed by our collaborators in Basel [13] at JLAB. On the right side of Fig. 2.3 the spectral function, as a function of the missing energy for different missing momenta is shown. The data (solid line) are compared with the SCGF method [42] calculation (dashed line) for NM at the lowest possible temperature, 2 MeV, and at a density corresponding to the average density of ^{12}C . Even if the calculations do not include long-range correlations and are calculated for infinite nuclei there is good agreement between the data and the calculation for the lowest missing momenta up to 410 MeV. For the low missing energy there is a lack of strength in the calculation. This implies that the SRC are not sensitive to surface effects and are more important for the interior nucleon states. The depletion of 25% of the occupation number shown in the right hand side of Fig. 1.1 is then due only to SRC whereas the more pronounced depletion for the states closer to the Fermi level is due to long-range correlations. The distribution of the spectral strength calculated in Correlated Basis

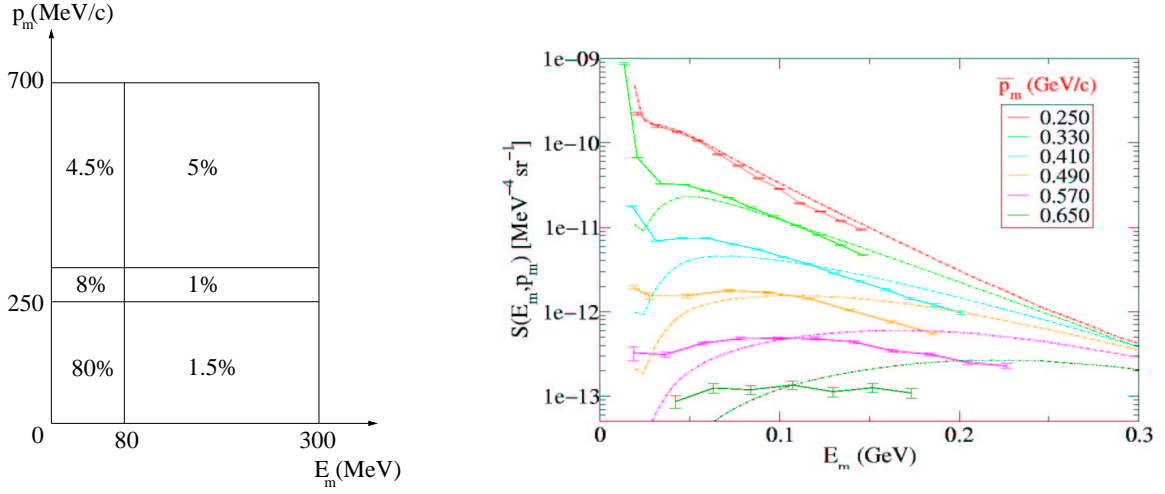


Figure 2.3: Left panel: distribution of the single-particle spectral function strength in missing momentum and energy region as calculated in CBF theory [14]. Right panel: spectral function extracted from $^{12}\text{C}(e,e'p)$ experiment at JLAB compared with SCGF method for nuclear matter at $T=2$ MeV [45].

Function theory [14] (CBF) in dependence of the missing momentum and missing energy is shown in Fig. 2.3 (left panel). The CBF theory predicts an 80% strength for moderate missing energy and missing momentum corresponding to the emission of a nucleon. The spectral function is also sensitive to SRC for a wide range of missing momentum up to 700 MeV/c, where the strength is 4.5%. The calculations also show that for high missing energy and missing momentum the strength of the spectral function is enough to investigate SRC, while for moderate missing momentum and large missing energy the strength is so low that it is difficult to make experiment in such a region.

2.2 Pavia model

In this model the calculation of the hadron current is based on the projection-operator method defined by Feshbach [26]. The entire Hilbert space is divided into two complementary subspaces. The problem becomes less complicated when it is restricted to a part of the Hilbert space. In this simplification the eigenvalues of the problem are projected onto these two subspaces through the projection operators P and $Q=1-P$. The calculations are done only in the P -subspace including the Q contribution in an effective way [24]. In this way the matrix elements of eq. 2.4, for a residual nucleus left with excitation energy E and a set of quantum numbers α ,

can be written as

$$J^\mu(\vec{k}) = \int d\vec{r} \int d\vec{r}_1 \int d\vec{r}_2 e^{i\vec{k}\cdot\vec{r}} \chi_{E\alpha}^*(\vec{r}_1, \vec{r}_2) \times \hat{J}_{eff}(\vec{r}; \vec{r}_1, \vec{r}_2) \Phi_{E\alpha}(\vec{r}_1, \vec{r}_2) [S_\alpha(E)]^{1/2}. \quad (2.15)$$

The operator \hat{J} in eq. 2.4 is computed in the P-subspace. Therefore the effective hadron operator \hat{J}_{eff} takes its place in eq. 2.15. The $\chi_{E\alpha}$ is the scattering state, i.e. the final state $|\Psi_f\rangle$ in eq. 2.4, and the initial state $|\Psi_i\rangle$ is represented by the bound state $\Phi_{E\alpha}$ normalised by the spectral strength $S_\alpha(E)$, which gives the probability to remove two nucleons. Both states are eigenfunctions of an energy dependent non-hermitian Hamiltonian [24, 27] but it is too complex to treat them in the same way so different approximation are used for the calculation of these.

2.2.1 The hadron current operator

Assuming a direct two-nucleon knockout mechanism, which means only the two emitted nucleons are involved in the reaction while the rest act as spectators, the effective nuclear current operator does not couple different subspaces, $P\hat{J}Q = 0$. It therefore can be replaced by the bare current operator \hat{J} which is the sum of a one-body current operator and a two-body current operator. The one-body term contains a convective and a spin-magnetic contribution and it is written as:

$$J^{(1)}(\vec{r}) = \langle \Psi_f | \sum_j \frac{e_j}{2M} [\vec{p}_j, f_j(\vec{r} - \vec{r}_j)] + \sum_j \frac{e_j}{2M} i \vec{\sigma} \times [\vec{p}_j, g_j(\vec{r} - \vec{r}_j)] | \Psi_i \rangle, \quad (2.16)$$

where e_j is the nucleon charge, the f_j represents the internal charge of the nucleon and g_j describes its magnetisation.

The two-body current operator arises mainly from the exchange of charged mesons between the two nucleons in the nucleus, the meson exchange current. The MEC contributes to the longitudinal and transversal component of the nuclear current operator [24]. The IC, where a virtual excitation of one nucleon takes place, contributes only to the transverse component of the hadron current operator. The NN potential is derived from an effective Lagrangian, where the isospin dependence is given by the exchange of a meson with isospin 1. The long-range part of the potential arises from the lightest meson, the pion, while heavier mesons like the ρ and the ω contribute to the short range part of the potential. In the approach of the Pavia group only the contribution of the π is considered. The one-pion exchange

potential [24] (OPEP), in coordinate space, is written:

$$V_{exc}(\vec{r}_1, \vec{r}_2) = \frac{f_{\pi NN}^2}{m_\pi^2} \vec{\tau}^{(1)} \cdot \vec{\tau}^{(2)} (\vec{\sigma}^{(1)} \cdot \vec{\nabla})(\vec{\sigma}^{(2)} \cdot \vec{\nabla}) \frac{e^{-m_\pi r}}{4\pi r} \quad (2.17)$$

where $f_{\pi NN}$ is the pion-nucleon-nucleon coupling constant and $\vec{r} = \vec{r}_1 - \vec{r}_2$. The exchange current operator \hat{J}_{MEC} has to satisfy the continuity equation [30]:

$$\vec{\nabla} \cdot \vec{J}_{MEC} = -i [\hat{V}_{exc}, \rho_0] - i [\hat{H}, \rho_{exc}], \quad (2.18)$$

where $\rho(\vec{r}) = (\rho_0(\vec{r}), \rho_{exc}(\vec{r}); \vec{r}_1, \vec{r}_2)$ is the four-vector of the charge density for the two nucleons exchanging a pion and the Hamiltonian operator is the sum of the kinetic term, the one-body potential and the OPEP. The exchange current operator which satisfies eq. 2.18 can be split into two terms, the seagull operator and the pion-in-flight operator. The seagull current in coordinate space is written [24, 28]:

$$\begin{aligned} \vec{J}_{MEC}^{sea}(\vec{x}, \vec{r}_1, \vec{r}_2) = & -\frac{f_{\pi NN}^2}{4\pi} \left[\vec{\tau}^{(1)} \times \vec{\tau}^{(2)} \right]_3 \left[\vec{\sigma}^{(1)} \delta(\vec{r}_1 - \vec{x}) (\vec{\sigma}^{(2)} \cdot \hat{r}) \right. \\ & \left. + \vec{\sigma}^{(2)} \delta(\vec{r}_2 - \vec{x}) (\vec{\sigma}^{(1)} \cdot \hat{r}) \right] \left(1 + \frac{1}{m_\pi r} \right) \frac{e^{-m_\pi r}}{m_\pi r} + (1 \leftrightarrow 2) \end{aligned} \quad (2.19)$$

and the pion-in-flight current is written [24, 28]:

$$\begin{aligned} \vec{J}_{MEC}^\pi(\vec{x}, \vec{r}_1, \vec{r}_2) = & -\frac{f_{\pi NN}^2}{16\pi^2} \left[\vec{\tau}^{(1)} \times \vec{\tau}^{(2)} \right]_3 \\ & \times (\vec{\nabla}_1 - \vec{\nabla}_2) (\vec{\sigma}^{(1)} \cdot \vec{\nabla}_1) (\vec{\sigma}^{(2)} \cdot \vec{\nabla}_2) \frac{e^{-m_\pi |\vec{r}_1 - \vec{x}|}}{m_\pi |\vec{r}_1 - \vec{x}|} \frac{e^{-m_\pi |\vec{r}_2 - \vec{x}|}}{m_\pi |\vec{r}_2 - \vec{x}|} \\ & + (1 \leftrightarrow 2). \end{aligned} \quad (2.20)$$

The Δ current does not satisfy the continuity equation. The two processes, the excitation by photon absorption (I) and the excitation by the exchange of the pion (II) have different propagators since the invariant energy \sqrt{s} of the virtual Δ is different. In the case of process (II) the invariant energy of the virtual resonance is low so that a static approximation [31] can be made in which only the baryon mass difference is considered. The propagator of the resonance for the (II) process can be written [28]:

$$G_\Delta^{\text{II}} = (M_\Delta - M_N)^{-1}, \quad (2.21)$$

where $M_\Delta = 1232$ MeV. In the case of the excitation by photon absorption the propagator depends on the invariant energy [28]:

$$G_\Delta^{\text{I}} = \left(M_\Delta - \sqrt{s_1} - \frac{i}{2} \Gamma_\Delta(\sqrt{s_1}) \right)^{-1}, \quad (2.22)$$

where $\sqrt{s_1} = \sqrt{s_{NN}} - M_N$, with $\sqrt{s_{NN}}$ being the experimentally measured invariant mass of the two outgoing nucleons, and Γ_Δ the width of the Δ decay. In space coordinates the Δ -current operator is written:

$$\begin{aligned} \vec{J}^\Delta(\vec{r}, \vec{r}_1 \vec{\sigma}^{(1)}, \vec{r}_2 \vec{\sigma}^{(2)}) = & \frac{f_{\gamma N \Delta} f_{\pi N N} f_{\pi N \Delta}}{36\pi m_\pi} \delta(\vec{r} - \vec{r}_1) \left\{ i(G_\Delta^I + G_\Delta^{II}) \right. \\ & \left[4\tau_3^{(2)} \left(Y^{(1)}(\vec{r}) (\vec{k} \times \hat{r}) (\vec{\sigma}^{(2)} \cdot \hat{r}) - Y^{(2)}(\vec{r}) (\vec{k} \times \vec{\sigma}^{(2)}) \right) \right. \\ & - [\vec{\tau}^{(1)} \times \vec{\tau}^{(2)}]_3 \left(Y^{(1)}(\vec{r}) \vec{k} \times (\vec{\sigma}^{(1)} \times \hat{r}) (\vec{\sigma}^{(2)} \cdot \vec{r}) \right. \\ & \left. \left. - Y^{(2)}(\vec{r}) \vec{k} \times (\vec{\sigma}^{(1)} \times \vec{\sigma}^{(2)}) \right) \right] + 2(G_\Delta^I - G_\Delta^{II}) \left[(\vec{\tau}^{(1)} \times \vec{\tau}^{(2)})_3 \right. \\ & \left. \times \left(Y^{(1)}(\vec{r}) (\vec{k} \times \hat{r}) (\vec{\sigma}^{(2)} \cdot \hat{r}) - Y^{(2)}(\vec{r}) (\vec{k} \times \vec{\sigma}^{(2)}) \right) \right. \\ & \left. \left. + \tau_3^{(2)} \left(Y^{(1)}(\vec{r}) \vec{k} \times (\vec{\sigma}^{(1)} \times \hat{r}) (\vec{\sigma}^{(2)} \cdot \vec{r}) - Y^{(2)}(\vec{r}) \vec{k} \right. \right. \right. \\ & \left. \left. \left. \times (\vec{\sigma}^{(1)} \times \vec{\sigma}^{(2)}) \right) \right] \right\} + (1 \leftrightarrow 2), \end{aligned} \quad (2.23)$$

where

$$\begin{aligned} Y^{(1)}(\vec{r}) &= \left(1 + \frac{3}{m_\pi r} + \frac{3}{m_\pi^2 r^2} \right) \frac{e^{-m_\pi r}}{m_\pi r} \\ Y^{(2)}(\vec{r}) &= \left(\frac{1}{m_\pi r} + \frac{1}{m_\pi^2 r^2} \right) \frac{e^{-m_\pi r}}{m_\pi r}. \end{aligned} \quad (2.24)$$

For the emission of two protons the term $(\vec{\tau}^{(1)} \times \vec{\tau}^{(2)})_3$ vanishes so that for the (γ, pp) and $(e, e'pp)$ reactions MEC do not contribute and only a part of the Δ -current contributes, while for the pn channel both currents play an important role. For the reaction (γ, pn) the contribution of the J^Δ depends on the type of the transition. When the pn pair is coupled in a $T=0$ state the Δ -process (I) is the only one contributing, while for $T=1$ state the process (II) is the non-vanishing one [31]. For the pp emission both processes contribute to the Δ -current with the same strength.

In section 1.4 it was said that in superparallel kinematics the IC do not contribute to the (γ, pp) reaction nor in the transverse response of the $(e, e'pp)$ reaction. This is evident from looking at eq. 2.23. The terms with the cross product of the momentum transfer \vec{k} with the relative motion vector of the outgoing nucleons \vec{r} vanish. The terms with $(\vec{\tau}^{(1)} \times \vec{\tau}^{(2)})_3$ also vanish. For the pn emission only the terms with the cross product of \vec{k} and \vec{r} vanish.

2.2.2 The initial state function

Based on the direct knockout assumption, the initial state can be projected in the P-subspace and possible terms due to coupling with different channel subspace can be neglected. The initial nuclear function in the case of the $^{16}\text{O}(\gamma, \text{pp})^{14}\text{C}$ reaction is calculated from the two-hole spectral function [33]. The long-range correlation and the SRC are both included in the initial overlap integral and are treated in a separate but consistent way. The basis space of the initial function is divided into a shell model (SM) space, \mathcal{M} , for the calculation of the long-range correlations and the complementary space, $\overline{\mathcal{M}}$, for the SRCs. The second step is then to treat the long-range correlations in the SM space with an effective interaction and introduce the SRC as a ladder approximation. The effective interaction is obtained by solving the Bethe-Goldstone equation (BGE) for the correlated pair wave function Ψ , with the method described in [34], where the Pauli operator \hat{Q} prohibits interaction between the two model spaces:

$$|\Psi\rangle = |\Phi\rangle + \frac{\hat{Q}}{W - \hat{H}_0} \hat{V} |\Psi\rangle. \quad (2.25)$$

In this equation $|\Phi\rangle$ is the uncorrelated shell model wave function. The defect wave function is obtained from the BGE solution above as the difference between the correlated and uncorrelated wave functions:

$$|\chi\rangle = |\Psi\rangle - |\Phi\rangle. \quad (2.26)$$

The effective interaction is then introduced by the G-matrix in the \mathcal{M} space as $\langle\Phi|G|\Phi\rangle = \langle\Phi|G|\Psi\rangle$. The two-hole spectral function becomes [33]:

$$S_j(\vec{p}_1, \vec{p}_2, \vec{p}'_1, \vec{p}'_2, \omega) = \sum_{nM} \sum_{ab, cd \in \mathcal{M}} \psi_{cd}^{*JM}(\vec{p}'_1, \vec{p}'_2) X_{cdJ}^{n*} X_{abJ}^n \times \Psi_{ab}^{JM}(\vec{p}_1, \vec{p}_2) \delta(\omega - E_j^{n, A-2}) \quad (2.27)$$

where n indicates the n th excited state of the residual nucleus with $E_j^{n, A-2}$ excited energy. The other indexes are the quantum numbers defining the orbit in the shell model space \mathcal{M} , X are the shell model amplitudes which contain the long-range correlations. The SRC are considered in the correlated wave functions, which replace the uncorrelated one in the usual formula of the two hole spectral function. Since the defect functions are calculated for partial waves of the relative motion of the two nucleons, the uncorrelated shell model wave function $|\Psi\rangle$ must be expanded in a harmonic oscillator wave function of the relative and centre of mass motion. The SRC are introduced by adding a defect function. For the relative coordinate \vec{r} and the centre of mass \vec{R} coordinate the initial two nucleon overlap, $|\Psi_i\rangle$ of eq. 2.4, is

then written [25]:

$$\begin{aligned} \Psi(\vec{r}_1\vec{\sigma}^{(1)}, \vec{r}_2\vec{\sigma}^{(2)}) = & \sum_{nlSjNL} c_{nlSjNL} \Phi_{nlSj}(\vec{r}) R_{NL}(\vec{R}) \\ & \times \left[\mathcal{F}_{lS}^j(\Omega_r, \vec{\sigma}^{(1)}, \vec{\sigma}^{(2)}) Y_L(\Omega_R) \right]^{JM}, \end{aligned} \quad (2.28)$$

where the upper case refers to the c.m. quantum numbers and variables and the lower case to the relative quantum numbers and variables. R_{NL} is the radial function for the c.m. motion representing the harmonic oscillator wave function, and $Y_L(\Omega_R)$ are the spherical harmonics. The radial wave function for the relative motion is written:

$$\Phi_{nlSj}(\vec{r}) = R_{nl}(\vec{r}) + \chi_{lSj}(\vec{r}). \quad (2.29)$$

The \mathcal{F} is the angular and spin wave function of the relative motion, whose angular momentum is coupled to the spherical harmonic of the c.m..

For the calculation of the initial two-nucleon overlap integral for the pn emission another method, explained in [28], has to be used since no spectral function is available. The initial function is written:

$$\Psi(\vec{r}_1\vec{\sigma}^{(1)}, \vec{r}_2\vec{\sigma}^{(2)}) \simeq \Phi_{JM}(\vec{r}_1\vec{\sigma}^{(1)}, \vec{r}_2\vec{\sigma}^{(2)}) f(r) X_{TT_3}(\vec{\tau}^{(1)}\vec{\tau}^{(2)}) \quad (2.30)$$

where $\Phi_{JM}X_{TT_3}$ is the SM wave function of the couple and X_{TT_3} is the isospin part. The function f contains only the SRC, the long-range correlations are neglected.

2.2.3 The final state function

The $\chi_{E\alpha}$ of eq. 2.15 are eigenfunctions of a Hamiltonian which contains an optical potential V^{OP} used to simulate the interaction between one nucleon and the residual nucleus and a nucleon-nucleon potential V^{NN} which describes their mutual interaction [35, 36]:

$$V_f = V^{OP}(1) + V^{OP}(2) + V^{NN}(12). \quad (2.31)$$

In distorted wave impulse approximation (DW) no mutual interaction between the two ejected nucleons is considered. The optical potential [24] used is a phenomenological one modelled on nucleon-nucleus scattering data and always contains a central, a Coulomb and a spin-orbit term. The isospin dependent term, responsible for the exchange current, is included only in the case of photo-absorption reactions, since it has been shown [32] that in the (e,e') reaction its effect is negligible. For the pp channel the potential used is the Bonn OBEPQ-A [37] and for pn emission the AV14 potential [38]. Since the nucleus has a larger mass than the nucleon, it can be considered infinite mass so the scattering function can be written as the product of

two uncorrelated single particle distorted-wave functions Φ^{OP} :

$$\chi^{DW} = |\Phi^{OP}(\vec{p}'_1)\rangle |\Phi^{OP}(\vec{p}'_2)\rangle. \quad (2.32)$$

The single particle distorted-wave function is the solution of the single particle Lippmann-Schwinger equation and reads [36]:

$$|\Phi^{OP}(\vec{p}'_i)\rangle = \left[1 + g_0^i(z_i) t^{OP,i}(z_i) \right] |\vec{p}'_i\rangle, \quad (2.33)$$

where $|\vec{p}'_i\rangle$ represents the plane-wave state of one nucleon with momentum \vec{p}'_i (the outgoing momentum) solution of the unperturbed Hamiltonian H_0 with eigenvalue $z_i = \frac{(\vec{p}'_i)^2}{2m_i} - i\epsilon$. The single particle Green-function $g_0^i(z_i)$ and the single particle scattering amplitude $t^{OP,i}(z_i)$ are written:

$$\begin{aligned} g_0^i(z_i) &= \frac{1}{z_i - H_0(i)} \\ t^{OP,i}(z_i) &= V^{OP}(i) + V^{OP}(i) g_0^i(z_i) t^{OP,i}(z_i). \end{aligned} \quad (2.34)$$

In plane wave impulse approximation (PW) the scattering function becomes a delta function centred on the momentum of the outgoing nucleon.

In the recent work of [35] and [36] the mutual interaction between the two outgoing nucleons has also been taken into account. In the two-particle Lippmann-Schwinger equation one has to consider higher perturbative orders of the scattering amplitude $t^{OP,12}(z_{12})$ and the NN scattering amplitude $t^{NN}(z_{12})$:

$$t^{NN}(z_{12}) = V^{NN} + V^{NN} g_0^{12}(z_{12}) t^{NN}(z_{12}), \quad (2.35)$$

where $z_{12} = z_1 + z_2$ and the two particle Green function is defined as:

$$g_0^{12}(z_{12}) = \frac{1}{z_{12} - H_0(1) - H_0(2)}. \quad (2.36)$$

Again making the assumption that the mass of the recoil nucleus is infinite the final state function is given as a solution of the Lippmann-Schwinger equation:

$$\begin{aligned} |\Psi_f\rangle &= \left[1 + g_0^{12}(z_{12}) t^{OP,12}(z_{12}) + g_0^{12}(z_{12}) t^{NN}(z_{12}) + \right. \\ &\quad g_0^{12}(z_{12}) t^{OP,12}(z_{12}) g_0^{12}(z_{12}) t^{NN}(z_{12}) + \\ &\quad \left. g_0^{12}(z_{12}) t^{NN}(z_{12}) g_0^{12}(z_{12}) t^{OP,12}(z_{12}) + \dots \right] |\vec{p}'_1\rangle |\vec{p}'_2\rangle. \end{aligned} \quad (2.37)$$

For the calculation in [35, 36] only the first three perturbative terms, which are depicted in the diagram of Fig. 2.4, were considered. The first term in eq. 2.37 is the plane wave approximation, diagram a) in Fig. 2.4 while the second term is the DW

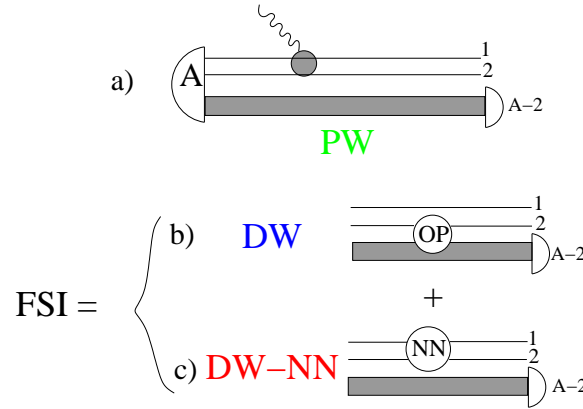


Figure 2.4: Diagrams of the interaction of the photon with the nucleus, the open circles represent the final state interaction. Diagram a) is the plane wave approximation, b) the DW approximation where one nucleon interacts with the residual nucleus through an optical potential operator and c) the mutual interaction between the two emitted particles is represented by the nucleon-nucleon potential operator.

approximation, diagram b), and the third term is the DW-NN where the mutual interaction of the two out-going nucleons is approximated by the nucleon-nucleon potential, diagram c) in the picture.

2.2.4 Comparison with results from $^{16}\text{O}(e,e'pp)^{14}\text{C}$ at MAMI

For the $^{16}\text{O}(e,e'pp)^{14}\text{C}$ reaction high resolution data are available [20]. The cross section for the transition to the ground state as a function of the missing momentum is shown in Fig. 2.5. The data were taken at MAMI in the A1 hall using the three high resolution spectrometers in super-parallel kinematics as described in [20]. The data points are compared with calculations presented in [35], where the MEC and the Δ -currents are neglected as explained in section 2.2.1, the overlap integral has the form of eq. 2.28 and the scattering states are represented from the first three terms of eq. 2.37. In Fig. 2.5 the solid lines show these three different contributions with the same colour legend as in Fig. 2.4. The green line is the PW approximation contribution and it is evident that the calculations over predict the data over the whole the missing momentum range. The DW approximation, blue line, reproduces the data very well for missing momentum up to circa 150 MeV/c but underestimates the data at higher missing momenta. The introduction of the mutual interaction between the two outgoing nucleons, red line, shows an enhancement at high momenta of a factor 20 giving a better description of the data. SRC are included in the initial overlap integral for all the approximations, as explained in section 2.2.2, so they are not responsible for the better agreement with the data. One can conclude that even

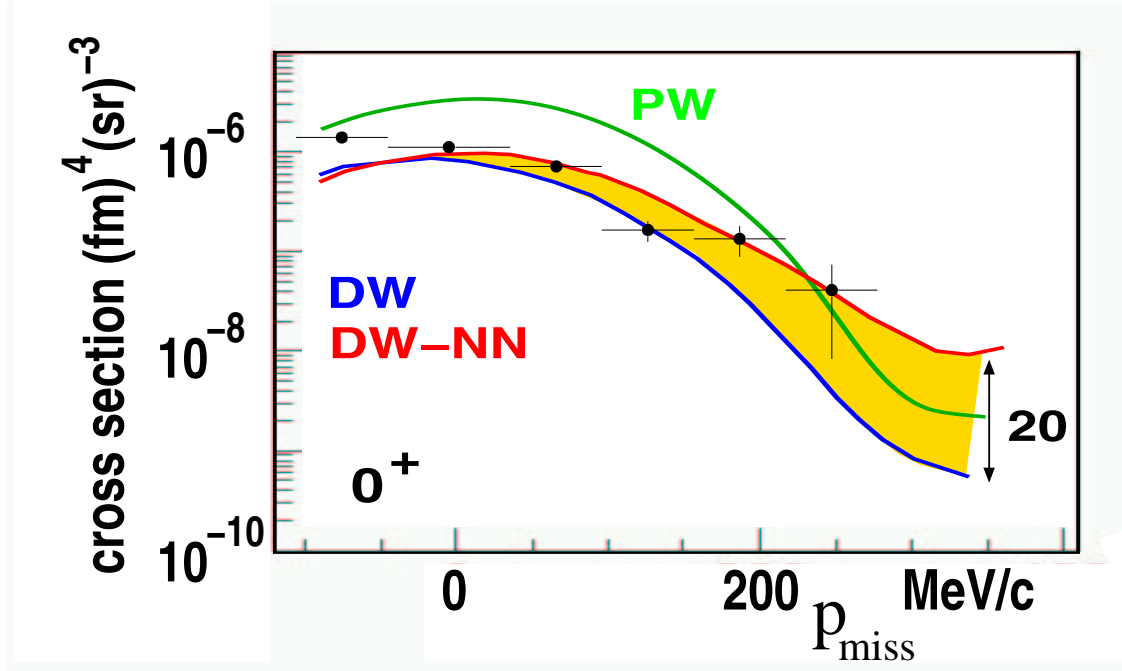


Figure 2.5: Missing momentum distribution for $^{16}\text{O}(e,e'pp)^{14}\text{C}$ reaction at MAMI for the transition to g.s. compared with theoretical calculation from [35].

when the two outgoing nucleons are ejected back-to-back their mutual interaction is not a small effect and therefore non-negligible as has been treated in all the calculations.

2.3 Gent model

The group of the University of Gent has also dealt with the calculation of the cross sections for two-nucleon emission as reported in [39, 40, 41]. Their approach to the problem is, in some aspects, the same as the one of Pavia. The approach is non-relativistic and they also work with the direct knockout approximation. They considered the simplest final state: the two nucleons are ejected in the continuum. Only the distorted wave is considered, the mutual interaction of the two nucleons is neglected. This constraint preserves the orthogonality of the initial and final wave functions, so that no interference terms appear in the scattering matrix.

The final $(A-2)$ -nucleon state is expanded in terms of the two-particle two-hole eigenstates of the Hartree-Fock Hamiltonian. The residual nucleus, as spectator, remains in the state with J_R and M_R angular and magnetic momentum and can be expressed by the two-hole state $|(\hbar\hbar')^{-1}J_R M_R\rangle$. The final state wave function is

then written [41]:

$$\begin{aligned}
|\Psi_f^{A-2}(E_x, J_R M_R)\rangle &= \sum_{hh'} X_{hh'}^{E_x} |(hh')^{-1} J_R M_R\rangle \\
&= \sum_{hh'} X_{hh'}^{E_x} \sum_{m_h m_{h'}} \frac{1}{\sqrt{1 + \delta_{hh'}}} \times \langle j_h m_h j_{h'} m_{h'} | J_R M_R \rangle \quad (2.38) \\
&\times (-1)^{j_h + m_h + j_{h'} + m_{h'}} \times c_{h-m_h} c_{h'-m_{h'}} |\Psi_0\rangle.
\end{aligned}$$

The ground state of the target nucleus is $|\Psi_0\rangle$ which corresponds also to the chosen initial state Ψ_i ; $X_{hh'}^{E_x}$ are the two-hole overlap amplitudes which determine the two overlap functions between the ground state of the initial nucleus and each of the states of the residual nucleus. The overlap amplitudes are treated as input parameters.

The hadron current operator contains the pion seagull, the pion-in-flight and the Δ -isobar operators as in the Pavia approach with a one-body operator that is the product of one-body charge and a current-density operator with a central correlation function $g(|\vec{r}|)$ [41]:

$$\left(J^{(1)}(\vec{r}_1) + J^{(1)}(\vec{r}_2) \right) g(|\vec{r}|) + g^\dagger(|\vec{r}|) \left(J^{(1)}(\vec{r}_1) + J^{(1)}(\vec{r}_2) \right) \quad (2.39)$$

In the correlation function $g(|\vec{r}|)$ the SRC for the initial state are inserted, while the $g^\dagger(|\vec{r}|)$ accounts for the SRC in the final state, the correlation between the two out-going nucleons.

2.3.1 Comparison with results from $^{16}\text{O}(e, e'pp)^{14}\text{C}$ at MAMI

The recent results for the $^{16}\text{O}(e, e'pp)^{14}\text{C}$ experiment performed at MAMI [20] in super-parallel kinematics are also compared to the calculations [41]. In Fig. 2.6 the pair momentum in the c.m. distribution for the transition to the g.s. of ^{14}C is shown. The dashed line are calculations using the distorted-wave approximation where only the Δ -current is included; they underestimate the data and do not even reproduce the shape. When SRC are added, solid line, the calculations reproduce the data well but underestimate them by a factor 2. The dot-dashed line is a plane-wave approximation with Δ -current and SRC, the shape of the data is not reproduced. These results just underline the importance of SRC in the two-nucleon knockout process. The lack of agreement with the data may be due to the not inclusion of the relativity or the mutual NN interaction, which are included in the Pavia-Mainz model reported in the previous section (Fig. 2.5).

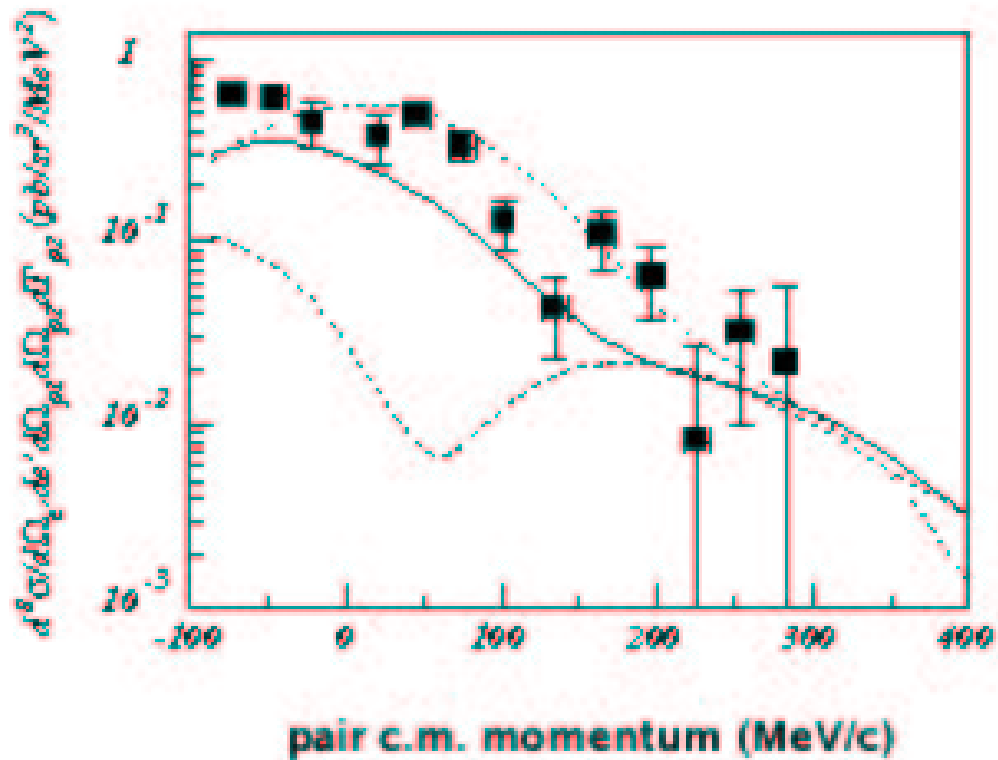


Figure 2.6: Pair momentum in the c.m. distribution for $^{16}\text{O}(e,e'pp)^{14}\text{C}$ reaction at MAMI [20] for the transition to g.s. compared with theoretical calculation from [41]. The dashed line contains the Δ -current in a distorted wave calculation. The solid line is a distorted-wave calculation including the Δ -current and central SRC. The dot-dashed line is a plane wave calculation with Δ -current and central SRC.

Chapter 3

Experimental setup

The high resolution (γ, NN) experiments were carried out at the Mainzer Microtron (MAMI) [47] facility in the summer of 2002 in collaboration with Edinburgh, Mainz and Glasgow universities. The electron beam was directed to the experimental hall, where bremsstrahlung photons were produced on a thin nickel foil and their energy was determined using the Glasgow tagging spectrometer (tagger). The photon beam was collimated onto a thin water target, placed on an angular correlation table near the shielding wall which separates the experimental area from the magnets of the tagger and an electron beam dump. This was the first time the new high resolution high purity germanium (*HpGe*) detectors, provided by the University of Edinburgh, was used to detect charged particles. In combination with *HpGe* double sided silicon strip detectors (DSSD), from Edinburgh and Glasgow University, were used to reconstruct the vertex of the reaction. For the detection of the neutrons, five stand of the Glasgow-Tübingen time-of-flight scintillators (TOF) were used. These were positioned at forward angles at a distance of about 15 m from the target. In Fig. 3.1 a drawing of the experimental apparatus in the reaction area in the experimental hall is shown. The tagger and the shielding wall are not depicted. In this chapter the detector features, with particular attention to the motivation for their choice, are described.

3.1 The Microtron MAMI at Mainz

MAMI [47] is a 100% duty factor accelerator which effectively produces a continuous electron beam. The electrons are accelerated up to the maximum energy 855 MeV by three successive racetrack microtrons (RTM). In Fig. 3.2 a floor plan of the MAMI facility is shown. The electrons, pre-accelerated to 3.5 MeV in a linac, are injected into the first RTM, MAMI A, where they are accelerated up to 14.35 MeV through 18 turns. In Fig. 3.3 a schematic drawing of a typical RTM is shown. The

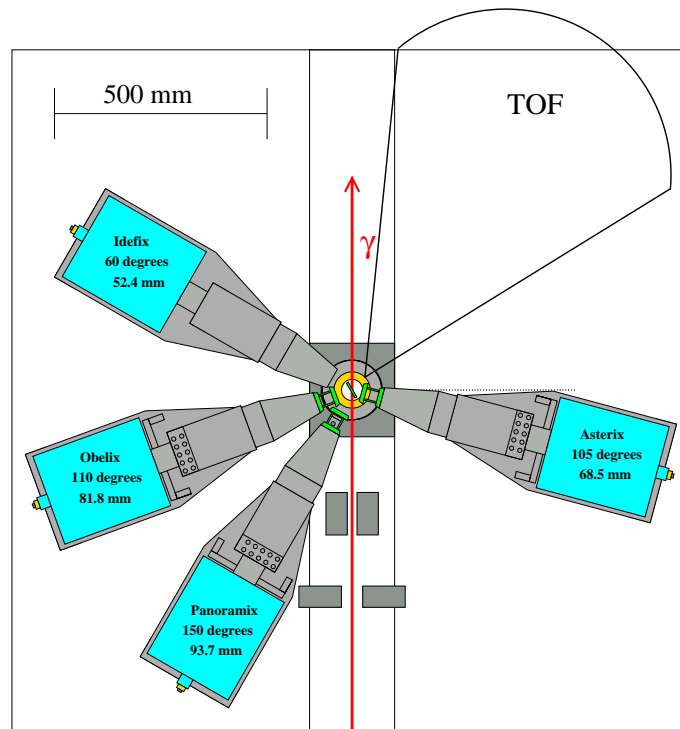


Figure 3.1: Correlation table where the germanium detectors were fixed on a movable guide rail. The target is fixed in the middle of the table. The photon beam impinges on it after emerging from the collimator in the shielding wall. The TOF were placed at a distance of about 15 m from the target.

electrons are accelerated in the linear acceleration section and are bent by the two return magnet so that the electrons are re-circulated several times until their orbit reaches the extractor magnet and the beam is directed away from the RTM. In the second microtron MAMI A2 the electrons are accelerated to 180 MeV before they are injected into the final microtron MAMI B. Here the beam is recirculated 90 times, each of which increases the electron energy by 7.5 MeV; the beam can be extracted from each even number of return path up to the largest path corresponding to the maximum energy of 885 MeV. After extraction from MAMI B the beam can be directed into several experimental halls, X1, A1, A2, A3 and A4. The mean energy at the third stage has been measured with a precision of ± 160 keV. The energy spread, mainly due to synchrotron radiation, is about 50 keV (FWHM). For the present experiment a beam energy of 855 MeV a current of 50 nA was used.

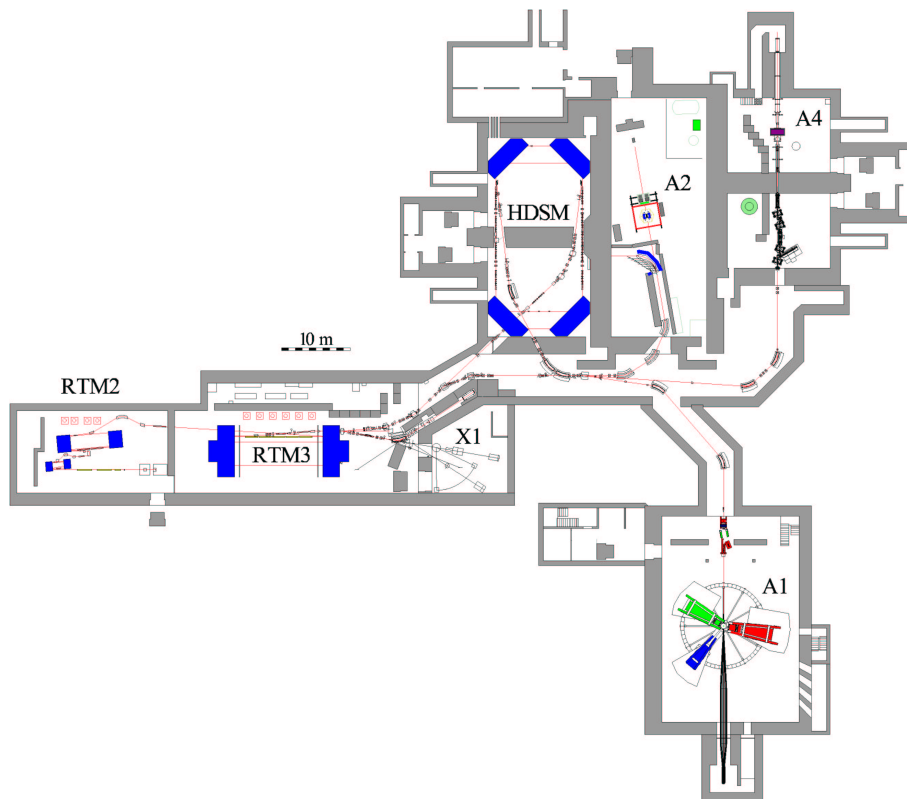


Figure 3.2: Floor plan of the Mainz Microtron. After the three stage of RTM the beam is directed to the experimental halls. The present experiment took place in the A2 hall, close to it the MAMI C, which is going to operate soon, is shown.

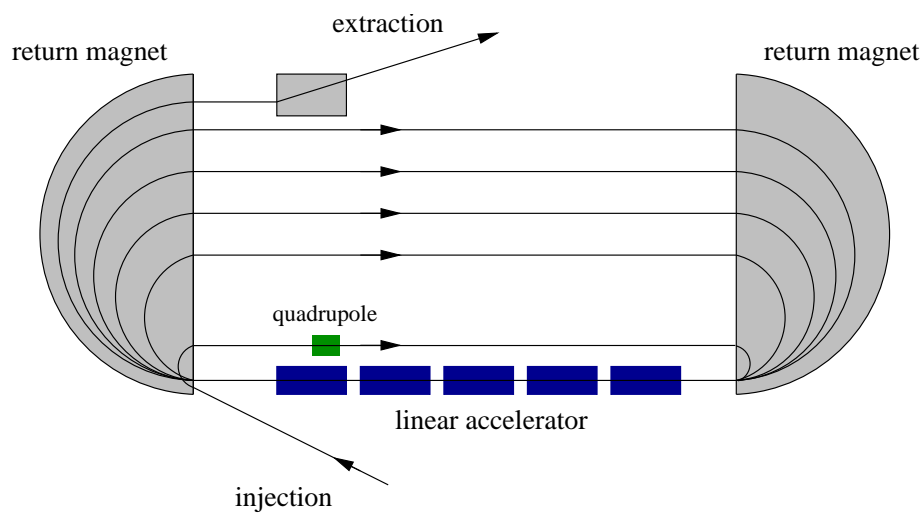


Figure 3.3: Schematic diagram of a typical RTM.

3.2 Photon tagging

The electron beam with a energy E_0 strike a 4 μm thick nickel foil radiator. At the energy range of MAMI B the electrons loose the energy predominantly by the bremsstrahlung process generating radiative photons with energy E_γ . The scattered electrons travel through the magnetic field of the spectrometer and are detected at the focal plane; the position of detection gives the deflected electron energy E_e so that the energy E_γ of the photon is easily determined by:

$$E_\gamma = E_0 - E_e$$

The Glasgow-Mainz Tagging Spectrometer and the tagged microscope work following this principle.

3.2.1 The Glasgow-Mainz Tagging Spectrometer

In Fig. 3.4 a schematic drawing of the tagging spectrometer is shown. The tagger [48] consists of a quadrupole-dipole magnet system and a focal plane detector. The quadrupole positioned after the radiator is used to vertically focus the electrons and to correct for some aberration. The focused electrons traverse the dipole magnet, which provides an homogeneous magnetic field and its shape is designed so that the electrons are focused into the same plane, the focal plane, where the focal plane detector [49] is housed. Electrons which do not interact with the radiator are collected in a Faraday cup outside the experimental hall.

The focal plane detector consists of an array of 353 2 mm thick scintillators set perpendicular to the direction of the scattered electrons. They are placed at always the same separation and the width of each element varies in a way that each of it half-overlaps with its neighbour in order to make a coincidence with the adjacent scintillator; this is required to distinguish the electron with the right trajectory from the background. In Fig. 3.5 a schematic drawing of some scintillators of the focal plane detector is shown. Each scintillator is read out with one of the smallest photomultiplier tube (PM) available to fit in the restrict geometry of the detector layout. The Hamamatsu Photonics R1635 with 9 mm diameter photocatode [49].

The tagger can tag photons from 40 to 800 MeV energy at an overall rate of 2×10^8 photon pro second with an energy resolution which varies over the focal plane due to scintillator widths, in average it is around 2 MeV. The cone of the tagged photon is forward peaked and covers a characteristic angle of about m_e/E_0 , with m_e the rest mass of the electron. In order to have a defined photon spot at the target the photon beam travels trough a collimator before reaching the experimental area, as shown in Fig. 3.4. This collimation prevents the photons in the tails of the angular distribution to reach the target, therefore the photon flux at the target is reduced. The photon

flux diameter is around 8 mm. This means that the number of post-bremsstrahlung electrons counted at the focal plane does not correspond to the number of photons reaching the target. A correction for the photon transmission efficiency called tagging efficiency must be done and it is explained in section 4.2.1.

The image of the photon beam can be monitored during the experiment with a photon camera placed behind the experimental area. If a variation in the position of the centre of the beam spot with respect the collimator centre was observed an immediate steering of the electron beam was carried out.

Since the purpose of this experiment is to resolve final states in the residual nucleus, as explained in section 1.4, we needed a energy resolution of circa 1.7 MeV. In order to reach this resolution the microscope tagging spectrometer, a high resolution electron detector in the focal plane of the dipole magnet, was used in coincidence with the tagger.

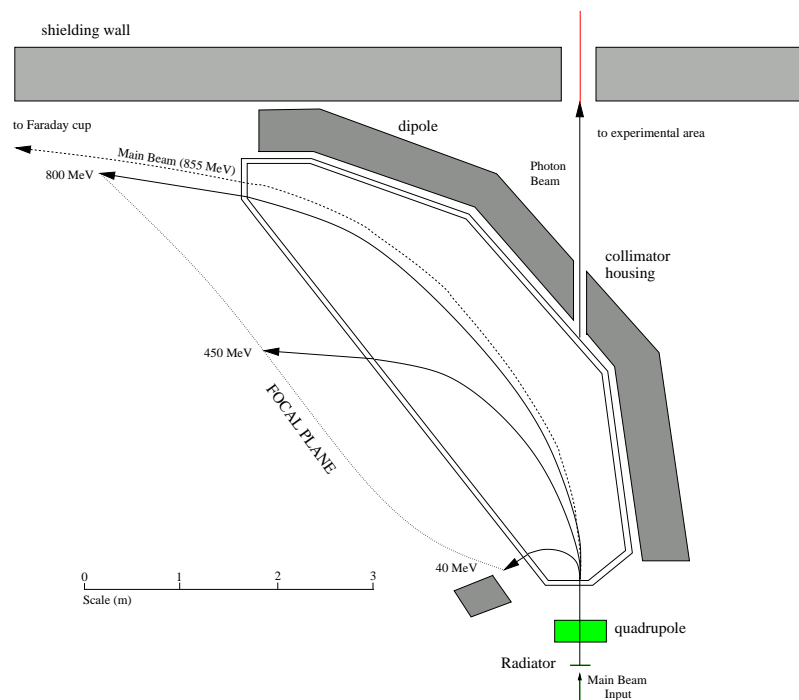


Figure 3.4: Sketch of the tagger. The layout of the scintillators in the tagger focal plane is shown in Fig. 3.5.

3.2.2 The Tagger Microscope

The tagger microscope [51, 52] works according to the same principle as the tagger focal plane detector. It is a position sensitive detector consisting of an array of 96 scintillation fibres positioned on the focal plane of the dipole magnet, just behind

the tagger scintillators. The energy resolution of the tagger can be improved by a factor six over an energy range of 65 MeV at a beam energy of 855 MeV. Each scintillator is 2 mm thick and 3 mm wide and overlaps the adjacent scintillators by a third of its own width. The energy range used for this experiment was from 170 to 220 MeV. For this energy range the microscope is bent 23° with respect to the tagged electron path due to the focal plane shape. This lead to an energy resolution of 0.6 MeV (FWHM) [52] when two adjacent fibres were fired. Only when one fibre was fired the energy resolution is a factor 6 better than the resolution of the main tagger, 0.3 MeV (FWHM) [52]. Since the most of the electrons hit two fibres the photon energy resolution for $E_\gamma=170\text{-}220$ MeV is 0.6 MeV. The microscope has its own readout, so that microscope and tagger can be used simultaneously and independently. As we used a high beam current a coincidence with the channel of the tagger in front is required to reduce the background. This means the microscope is always used in conjunction with the tagger in this experiment.

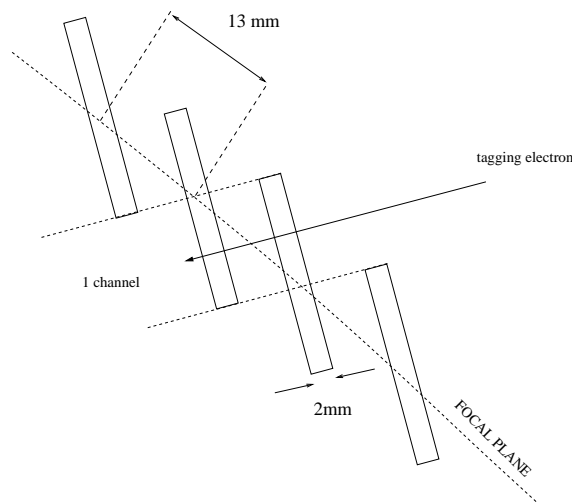


Figure 3.5: Schematic drawing of some elements of the tagger focal plane detector. The scintillators are all 2 mm thick and at a separation of 13 mm, while the width varies.

3.3 Target

Fig. 3.6 shows a picture of the target area. The photon beam enters the experimental area from the hole in the shielding wall seen at the back. After a short flight path it strikes the target, which is fixed on the correlation table. The target was aligned with the beam so that the centre of the beam spot hits the geometrical centre of the target. An aluminium frame of 1 mm thickness has an opening of 40×40 mm²; on each side a thin polyethylene foil was glued to contain the water. Using a syringe

the target can be filled with either normal or heavy water. In order to decrease the energy loss of the ejected particles the target was rotated to form an angle of 30 degrees with respect to the beam line, the z - axis in the lab reference system. The target was refilled regularly during the experiment because of the formation of a small air bubble due to evaporation.

Solid targets were used for the investigation of the halo nucleus ${}^6\text{He}$ [54]. A 95.5% enriched ${}^6\text{Li}$ target was used for the ${}^6\text{Li}(\gamma, \pi^+){}^6\text{He}$ reaction and a CH_2 target for calibration purposes.

3.4 The solid state detectors

To detect positively charged particles, semiconductor detectors [50] were used because of their capability to achieve a high energy resolution. Semiconductor detectors are based on a semiconductor junction also known as rectifying diodes, where a p-type and a n-type material form a contact. Because of the different concentrations of electrons and holes an initial diffusion of electrons from the n-type to the p-type and of holes in the opposite direction occurs. Since the n and p materials are initially neutral there will be a negative charge concentration on the p-type and a positive concentration on the n-type, which generates an electric field gradient across the junction. The gradient eventually stops the diffusion and a region of depleted charge is left. Because of the electric field gradient there is a potential difference across the junction. The area where the potential changes, is called depletion zone and there electrons and holes have free mobility. Electrons and holes entering this area will be swept out by the intrinsic electric field. Because of this characteristic semiconductor detectors are very good for detecting ionising particles. The intrinsic depletion zone is normally very thin, so that the application of an external reverse bias, i.e. the negative voltage applied to the p-side, is needed to increase the sensitive detection area. The ionising particle will start to produce electron-hole pairs when it enters the semiconductor material, these will be swept out by the applied electric field and will be collected at the end of the junction where metal contacts are placed. The collected current is stored in a capacitor; its charge is proportional to the voltage which is the output pulse signal of the detector. Since the number of electron-hole pairs produced by the ionising particle depends only on the energy loss of the particle, the converted pulse is a direct measurement of the energy deposited by the particle.

The charge signal from the semiconductor junctions is normally low therefore it is read out by pre-amplifiers, which amplify it and must have a low noise. Since the semiconductor junctions have an intrinsic capacitance of few picofarad the pre-amps must have a larger capacitance to guarantee stability and it must be connected as close as possible to the junctions to minimise the effects of any other capacitance from cables and associated electronics.

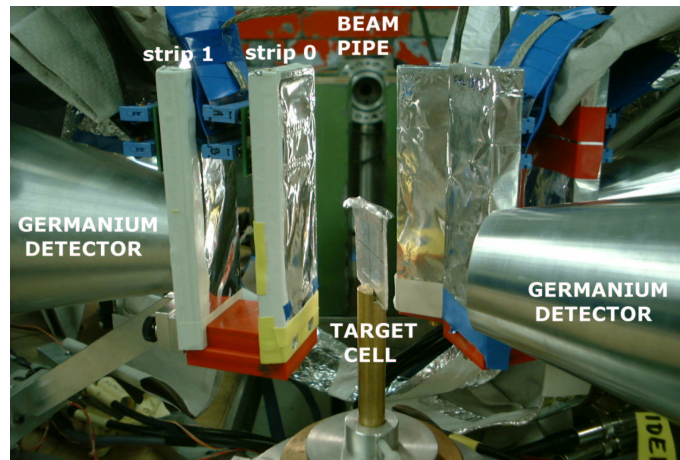


Figure 3.6: The target area viewed from downstream. The photon beam strikes the water target and the charged particles travel through the DSSD before passing through the Germanium detectors.

3.4.1 Double Sided Silicon Detectors

Two double sided silicon detectors (DSSD), mounted in front of the $HpGe$ detectors, were used to determine the incident angle of the ejected particles and to reconstruct the vertex of the reaction at the target. This is important for reduction of background caused by particles which do not originate from the reaction of interest. One double sided silicon detector consist of a n-type silicon wafer $300\ \mu\text{m}$ thick on which are implanted 24 p-type electrode strips on one side and 24 n-type electrode strip on the other side perpendicular to the p-type strips [50]. The strips are placed at a pitch of one millimetre from each other. The horizontal strips are the p-type and are connected to a pre-amplifier which provides a negative voltage and collect the electrons. The vertical strips are the n-type and connected to another pre-amplifier which provides a positive voltage and also collects the holes. In Fig. 3.7 a schematic drawing of one double sided silicon strip is shown. The vertical strips were read out individually while the horizontal strips were read out in pairs. This gives a 24×12 pixel matrix with the measured value of the in-plane angle, which gives the direction of the impinging particle, given by the horizontal strips, being more accurate than that of the out-of-plane angle. In Fig. 3.6 the two DSSDs are labelled *strip 0*, the front one, and *strip 1*, the rear one. The DSSDs were wrapped in aluminium foil to shield them from light and suppress pick up on the signals. In Fig. 3.6 the connectors of the ribbon cables on the rear of each DSSD are also visible. The other end of the ribbon cables was connected to the pre-amplifier that sits on a support on top of the Germanium hodoscopes. The pre-amps were also wrapped in aluminium foil, clipped together with the DSSDs and grounded in order to reduce pick up [53].

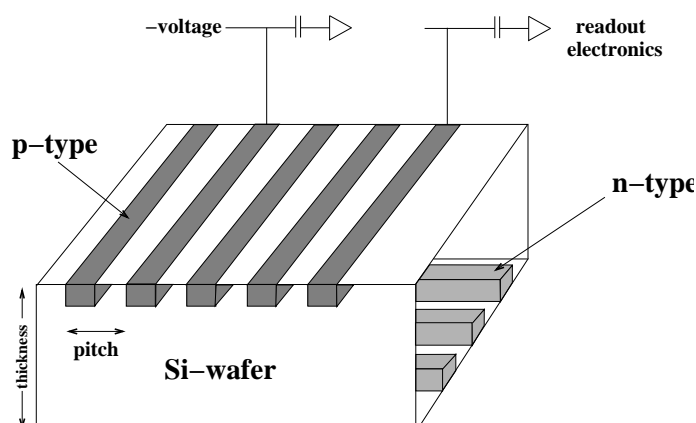


Figure 3.7: Schematic of one double sided silicon detector.

3.4.2 The Germanium hodoscope

A *HpGe* detector is also a semiconductor diode, where very high purity Germanium is implanted with p-type and n-type semiconductor on the surface of the Germanium crystal. The application of a high external reverse bias voltage causes the crystal to be fully depleted but generates a leakage current across the junction. The latter contributes to the noise in the output of the detector. If the applied voltage is too high it results in breakdown of the semiconductor, which turns to be conducting. Therefore to decrease the noise and to prevent the breakdown of the semiconductor the *HpGe* detectors are cooled down to the temperature of liquid nitrogen, namely 77 K; they can be warmed up to room temperature when the bias voltage is off.

The Edinburgh Germanium hodoscope [54, 55] is an array of five stacked *HpGe* detectors. Each stack consists of six *HpGe* planar crystals. Planar geometry leads to an uniform electric field so that, in principle, the response of the crystals is not position dependent. The crystals have an increasing diameter along the detector axis and the separation between two of them is always 2 mm. In Fig. 3.8 a plan view of one detector is shown. The diameters and the thickness of each crystals are indicated. The diameters of the crystals of each Germanium hodoscope are all the same while the thickness varies. In table 3.1 the thickness of the Germanium crystal for each hodoscope are reported.

They are placed in a vacuum holder aluminium cryostat which has a Beryllium window in the front. Beryllium is used in order to minimise particle energy losses since Beryllium has a low atomic number. In Fig. 3.6 it is possible to see the front of the detector housing. A tank for liquid nitrogen placed at the rear of the crystal housing keeps the six detectors cool for almost 24 hours. During the experiment several interruptions of the beam supply were needed in order to refill the nitrogen tank.

High voltage was applied to a pair of crystals and split between the pair such

that the adjacent surface of the two crystals was of the same electrical potential. The direct signal from the crystal goes to the pre-amplifier where it is amplified with a fixed gain, which can be chosen according to the expectation of the experiment. For each crystal two output signals come from the pre-amplifier; one of them, after attenuation and a delay, is digitised. The other output of the first crystal is divided into two signals, one which goes to the first level trigger and the second which goes to the second level trigger.

For the present experiment four Germanium hodoscopes were used. They were fixed on guide rails placed on the correlation table as can be seen in Fig. 3.1. The guide rails can be moved around the target holder so that the detectors could be placed at different in-plane angles during the beam time. Each of the detectors was named after the protagonists in the French version of the famous comic Asterix¹ since the manufacture who delivered them is in France. The detectors used for the $^{16}\text{O}(\gamma, \text{NN})$ data taking were Panoramix, Asterix, Obelix and Idefix, one other detector, named Majestic, was used for the $^6\text{Li}(\gamma, \pi^+)^6\text{He}$ experiment. Due to the limited preparation time before the start of the beam time it was not possible to equip all of the detectors with DSSDs; Panoramix, Asterix and Obelix were equipped with the two strip detectors while Idefix was not.

Crystal	Panoramix	Asterix	Obelix	Idefix
1	15.1 mm	14.2 mm	15.4 mm	15.5 mm
2	15.2 mm	14.0 mm	15.3 mm	15.2 mm
3	19.9 mm	19.7 mm	20.1 mm	19.7 mm
4	20.0 mm	19.9 mm	20.1 mm	20.1 mm
5	20.1 mm	20.0 mm	20.1 mm	20.3 mm
6	20.2 mm	20.5 mm	20.3 mm	20.3 mm
total thickness	110.5 mm	108.3 mm	111.3 mm	111.1 mm

Table 3.1: Crystal thickness for each Edinburgh Germanium hodoscope used in the experiment.

3.5 The scintillation detectors

Due to their lack of electric charge neutrons are not subject to Coulomb interaction [50] so they do not ionise matter. Neutrons only interact strongly with the nuclei so they have to come very close to the nucleus before a reaction can occur, therefore neutrons have a high penetrability. Usually scintillation material is used for the detection of neutrons, for this experiment plastic scintillators were used. These are hydrocarbon compounds; the neutrons interact with hydrogen and carbon nuclei

¹<http://www.asterix.tm.fr/>

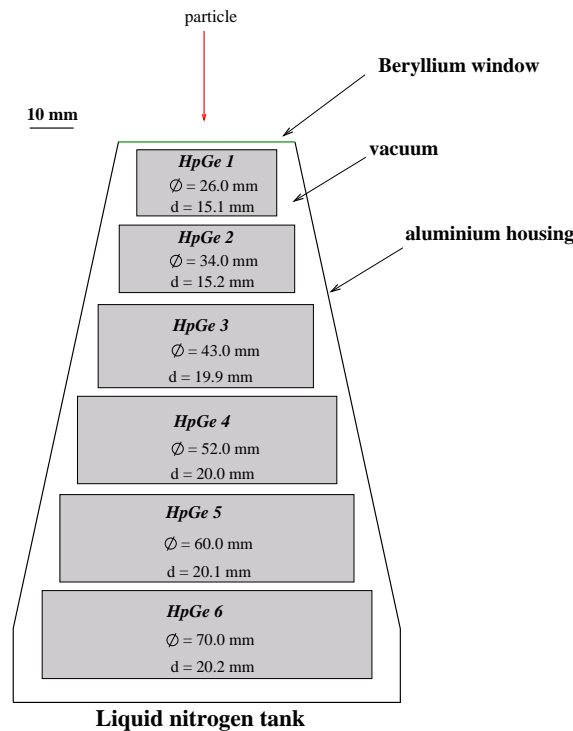


Figure 3.8: A scale cross section of one of the Germanium telescope with the active diameter Φ and the thickness d for each crystal.

in several way depending on their kinetic energy. The dominant process neutrons undergo in plastic scintillator is the elastic scattering (n, p) on hydrogen nuclei and $^{12}\text{C}(n, n)^{12}\text{C}$ [70]. The cross section of the elastic scattering decreases with increasing neutron kinetic energy till the removal of a proton or two neutron from carbon nuclei, i.e. $^{12}\text{C}(n, np)^{11}\text{B}$, $^{12}\text{C}(n, p)^{12}\text{B}$ or $^{12}\text{C}(n, 2n)^{11}\text{C}$, becomes larger [70]. A minor but not negligible neutron interaction with carbon nuclei is the production of one α particle, $^{12}\text{C}(n, \alpha)^9\text{Be}$, or three α particles, $^{12}\text{C}(n, 3\alpha)$; the latter is larger than the first [70]. In the scintillation detector, recoil protons from elastic and inelastic scattering are detected. The fact that the neutrons deeply penetrate in the matter is taken into account in the neutron-detection efficiency, which is always smaller than 1. The calculation of it is explained in section 4.5.5. The proton in a scintillation material interacts electromagnetically with the free valence electrons of the molecules [50]. These occupy electron energy levels, which have a fine structure corresponding to excited vibrational modes of the molecules. The proton entering in the material excites the electrons in the electron and vibrational levels to an excited electron levels. The electrons decay then radiatively to one of the vibrational state of the ground state; the released photons are in the visible wavelength. This is the fastest process; there is a slower decay process where the electrons first decay into a metastable levels and then to the ground state but this is not important in first

approximation for the type of scintillation material used in this experiment. Therefore the time evolution of the photon emission can be described with an exponential decay:

$$N_p(t) = \frac{N_0}{\tau} e^{-t/\tau} \quad (3.1)$$

where $N_p(t)$ is the number of photons emitted at time t and N_0 is the total number of photons emitted; the decay time, τ , depends on the material [50]. The light in the scintillator will be collected and translated into a pulse-height which is proportional to the energy deposited by the recoil proton. The energy and momentum of neutrons can be determined via their time-of-flight (ToF) along a known flight path, the flight path being the distance from the vertex of the reaction to the stop point in the scintillator. In fact the energy resolution depends [58] on the intrinsic time resolution, Δt , and on the uncertainty in the flight path, Δl . In a good approximation the relative energy resolution $\Delta E/E$ can be written as

$$\Delta E/E = \gamma(\gamma + 1) \left[(\Delta l/l)^2 + (\Delta t/t)^2 \right]^{1/2} \quad (3.2)$$

where γ is the Lorentz contraction factor, $\gamma = \frac{1}{\sqrt{1-\beta^2}}$. The energy resolution increases if Δl and Δt are minimised. The uncertainty in the flight path arises mostly from the counter thickness. In a thin scintillation material the particle impact position is determined with high precision which decreases the uncertainty in the flight path. But in a thin layer high energetic neutrons can escape and the neutron-detection efficiency decreases [59]. Therefore multi layered scintillation detectors, where several thin scintillation detectors are stacked behind each other in the direction of the neutron flight path are built nowadays and used for middle energy experiments like the present one. The solid angle covered by the scintillator hodoscope should be as large as possible in order to increase the counting rates in a restricted time of data collection [59]. This leads to the use of long scintillator bars with a length which allows the detectors to fit in the experimental hall.

3.5.1 TOF and Veto counters

An array of Glasgow-Tübingen TOF counters [59] is a collection of plastic organic scintillator (NE110) bars which are 5 cm thick, 20 cm wide and 300 cm long. The decay constant τ for NE110 is 3.3 ns, which gives a fast response to the impinging particle. The rise time from zero to the maximum of the light output is shorter than the decay constant [50]; very important to reconstruct time information with high precision, for example the time difference between two events. At both ends of the bar a lucite light guide is glued with an optical cement (NE 561) that has the same refractive index as the scintillation material, $n = 1.58$. This is used to channel the light into a photomultiplier tube (PM), which is glued to it with silicon rubber.

A PM is a device which consists of a photocathode, sensible to the light, and a series of dynodes, at which an external high voltage is applied, ending in a final anode all placed in a vacuum tube [50]. A photon impinging upon the photocathode produces by photoelectric effect an electron, which is accelerated by the external applied voltage towards the first dynode. Secondary electrons are emitted from the dynode and accelerated towards the second dynode, where the same process occurs. All the secondary electrons produced in the dynodes reach the final anode, where are read out. PM have normally a linear response, i.e. the electron current at the anode is proportional to the number of impinging photons at the photocathode. But their linear behaviour can change in the case of long periods of operation; in fact the PM gain can vary because of temperature changes, load changes or applied voltage changes [50]. Thus it is important to monitor the gain during the experiment. This was done using a light of constant intensity from an light emitting diode injected into the scintillator via a fibre-optic cable glued on the light guide [60]. This diagnostic light source was also used for calibration purposes (to find the walk correction, see section 4.5.1). One light emitting diode feeds 16 PMs.

The PMs are shielded against electromagnetic fields, that can compromise their proper operation, by μ -metal cylinders. All of the detectors are wrapped in thin Al foil in order to enhance light reflection; they are then further wrapped in black rubber sheets to eliminate the effects of outside light and to avoid mechanical damage. The scintillator bars were mounted with their long axes vertical to allow for a compact installation [59]. For that reason the two PMs per each bar and all the observables concerning them will be referred as *top*, the upper one, and *bottom*, the lower one.

Besides the TOF counters, which had been used in previous experiments, new Veto counters were assembled in Mainz in February 2000. The material used for the Vetos is EJ208 which is characteristically equivalent to NE110. A Veto bar is thinner than a TOF counter since it is used to identify whether a particle is charged. If a proton, for example, passes through the Veto it will almost immediately start to lose energy, so a signal will be registered, while we can assume a neutron will pass through the material without interacting with it. The Veto counters have the dimensions of $1 \times 23 \times 300 \text{ cm}^3$. They have, like the TOFs, light guides and PMs at both ends.

TOF and Veto bars can be mounted together on metal frames. Up to sixteen bars can be on one frame, arranged into two layers of eight bars. Two frames mounted together form a stand. A total of 32 detectors can be mounted on one stand.

For this experiment three complete stands, with three TOF layers and one Veto layer in front, and two incomplete, composed only of one frame of TOFs, were used. In picture 3.9 the five stands in the A2 hall can be seen, the picture was taken from the correlation table. The TOF stands are labelled with regressive Roman numbers from the beam line to the right, so that the very left stand in the picture is the V. Each layer is labelled alphabetically, for example the Veto of stand V is named A, the TOF layer behind is B and so on, like it is drawn in Fig. 3.10. From eq. 3.2 , for



Figure 3.9: Picture of the five TOF stands in the hall taken from the target table.

a fixed energy and known t and ΔT , in order to improve the energy resolution a long flight path is necessary. For this experiment the TOFs were placed at a distance of about 15 m from the target in the forward emission direction, as shown in Fig. 3.10. The backward direction would be kinematically favourable but in the experimental area there is not enough room to place the TOFs at a sensible distance from the target area.

3.6 Trigger Electronics and Data acquisition

The trigger electronics decide when the acquisition electronics have to be started and the decision is made using previously defined conditions, the “trigger conditions”, which characterise an event of interest. The purpose of the trigger is to record the largest possible number of valid events, supplementary reduction of the events can be done at a later stage in offline analysis.

3.6.1 The trigger

For this experiment a level-II trigger was used. The first level trigger takes the easy and fast decision as to whether an event could be accepted or not and opens the

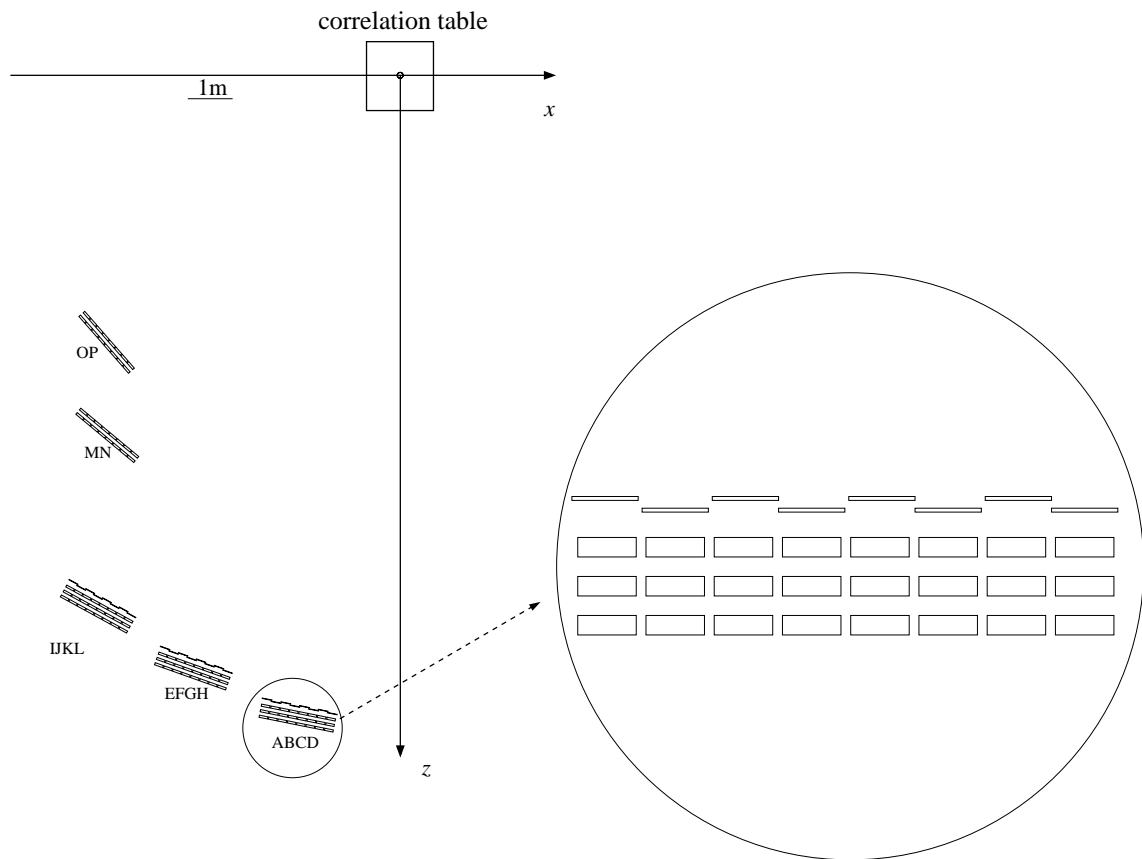


Figure 3.10: On scale sketch of the TOF stands in the hall with the used reference system with a schematical upper cross section of one TOF stand.

ADC² gates. The second level trigger can take more complex decisions which take more time. For negative results it will reset the whole system making it ready for the next event at an earlier stage then proceeding through the complete readout.

First level trigger

The first level trigger used a LRS4508 MLU, Memory Lookup Unit. A schematic drawing of the circuit is shown in Fig. 3.11. The input of the first level trigger is the signal of one of the first *HpGe* crystals. Two other input signals were used for special triggers: the pulse signal of the Pb-glass detector to calculate the tagging efficiency (section 4.2.1) and the output signal from the diagnostic light source (section 3.5.1), TOF pulser, for calibration purposes, see section 4.5.1.

The signal of the first crystal of a *HpGe* is split into two parts, one part going to

²analogue-to-digital converter

the first level trigger and the other to the second level trigger. The first part of the pulse is fed into a timing filter amplifier (TFA) where it is amplified, the pulse shorted and the noise reduced. A low-pass filter with a time constant of 20 ns smoothes the fluctuations in the noisy pulse and a high-pass filter with a time constant of 50 ns shortens the pulse. The fast pulse is then passed through two leading edge discriminators [50] (LED) that provide upper threshold (300 mV) and lower threshold (30 mV corresponding to circa 15 MeV proton). The LED issues a logical signal whenever the amplitude of the input pulse is greater than the fixed limit. The logical signal from each first *HpGe* crystal is fed into a logical OR, whose output is the input signal for the first level trigger. Whenever a hit in the first of any of the *HpGe* crystals is above the discriminator threshold the first level trigger is activated. The prompt *HpGe* QDC ³ gates are opened and the collected charge is translated into a digital value using a constant time window of 500 ns. The prompt TDC ⁴ starts counting when the signal from the first level trigger arrives. The microscope TDC is also started and the QDC gate opened. The charge signal from the DSSDs is also digitised in the QDC. The TOF QDC gates are opened for recording and the TDCs start counting. The tagger TDC starts counting whenever an electron hits the focal plane detector, the first level trigger stops it.

Second level trigger

The second level trigger also used a LRS4508 MLU. A schematic drawing of the second level trigger is shown in Fig. 3.12. At the bottom of Fig. 3.12 there is a subset of the second level trigger for the Germanium hodoscopes.

Whenever a signal from the first level trigger arrives the second level trigger is activated if the following input signals are simultaneously valid:

- tagger TDCs coincidences, which are built between two fibres in order to have prompt electrons, as explained in section 3.2.1.
- TOF coincidences between top and bottom PMs, see section 3.6.2.
- The Germanium sum trigger, which is the algebraic sum of the half of the pulse signals of the first *HpGe* crystals. The algebraic sum is determined in a linear Fan-In/Fan-Out ⁵. The output signal of the Fan-Out pass through an LED; whenever the sum of the signals of any of the Germanium hodoscope is above its specific threshold the input is valid.

The gates opened from the first level trigger are closed. The interrupt signal tells the TOF electronics and the tagger electronics to stop processing the data and to

³charge-to-digital converter; the current output is integrated over a time given by the gate width.

⁴time-to-digital converter

⁵A linear Fan-In can have several analogue or digital input signals; the algebraic sum of them is delivered at the single output. A linear Fan-Out distributes an input signal to several output leaving it unchanged. [50]

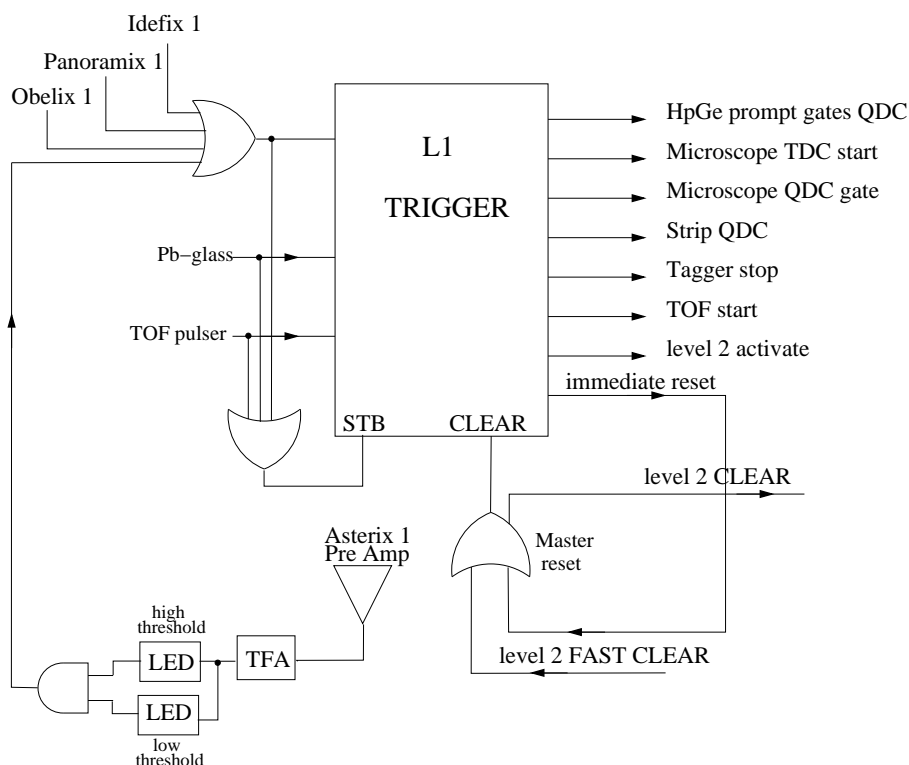


Figure 3.11: Schematic sketch of the first level trigger.

read-out the buffer where the data were temporarily stored. No further triggers can be generated as long as the event information, which are temporarily stored in the front-end computer in the experimental hall, are being sent to a back-end computer in the counting room and recorded on disc. A reset signal is sent to the first level trigger if the event is correctly recorded or if any of the second level trigger conditions are not satisfied without the data being read out (Fast clear). After the reset the system is again ready for the acquisition of a new event.

For the detection of pions, a delayed QDC is implemented. The π^+ has a life time of 26 ns in matter then it decays into a μ^+ . The muon itself decays $\mu^+ \rightarrow e^+ + \nu_e + \bar{\nu}_\mu$ with a life time of 2.2 ns. If an afterpulse is required within 7 μs from the initial signal in the Germanium the 65% of the π^+ s are detected via the decay product of the μ^+ , the positrons.

3.6.2 TOF electronics

The TOFs had supplementary electronics, a schematic of which is shown in Fig. 3.13. Each TOF PM anode signal is fed, via a 25 m long cable, to pulse-splitter, where the signal amplitude is split into two parts.

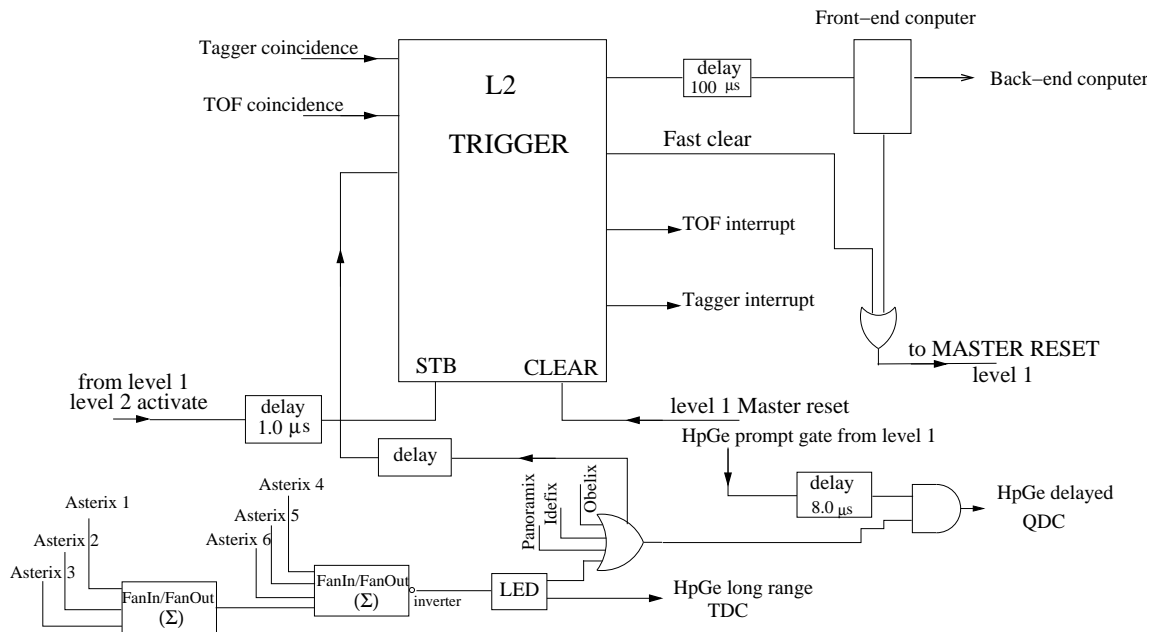


Figure 3.12: Schematic sketch of the second level trigger.

One branch is fed to an LED unit, with a common threshold for every input signal which is set by software and can be in the range 16–1024 mV. The logical output of the LED is connected to TDC units, where the scalers start counting whenever the first level trigger gives a signal and keep on counting until the end of the time window is reached. The same logical signals of the top and bottom PMs are connected to a coincidence unit where the coincidence between both is required. The result of the coincidence is passed to the second level trigger, for the identification of a valid event as explained in section 3.6.1.

The other branch, after a fixed delay of 200 ns, needed to give the trigger electronics the time to make the decision whether the event has to be taken or not, is fed to a QDC module that integrates the charge during a given period to produce the digital signal.

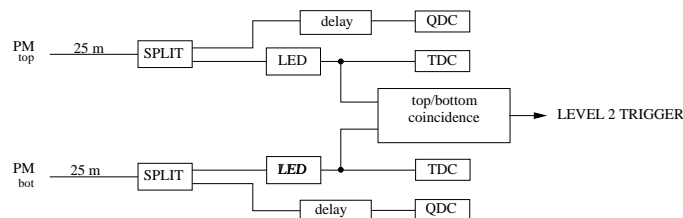


Figure 3.13: Schematic sketch of the TOF electronics.

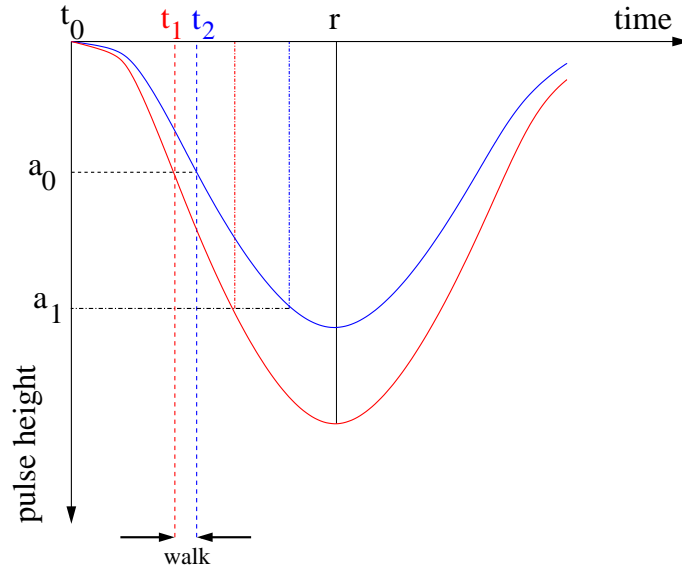


Figure 3.14: Typical behaviour of detector pulse-height as a function of the time. Two signals coincident in time but of different amplitude are drawn. The signals cross the fixed threshold at different times.

Walk correction for time signal from LED

The time signal from a leading edge discriminator depends on the pulse-height. As illustrated in Fig. 3.14 simultaneous signals with different amplitudes cross the threshold a_0 at different times t_1 and t_2 . If the threshold is higher, a_1 , the effect is larger. This time difference is the so-called walk and has to be corrected for. Assuming the detector signal shape is approximated by a parabolic-like curve, as stated in [66], the time walk can be parameterised by

$$t - t_0 = r \left(1 - \sqrt{\frac{a_0}{q}} \right) \quad (3.3)$$

where r is the rise time, i.e. the time the PM or the pre-amps needs to reach the maximum of the signal amplitude q , and a_0 is the amplitude threshold. For the Germanium hodoscopes and the TOFs a walk correction had to be made, as for both detectors, leading edge discriminators were used.

3.6.3 Data acquisition system

The data acquisition and analysis system ACQU [61] developed at Glasgow University consists of two parts.

One part controls the hardware:

- initialisation of the electronics modules like setting of the thresholds for the LEDs and the detector pedestals ⁶.
- read-out of the data from the ADC buffers.
- storage of the data in the back-end computer.

The second part allows the raw data to be displayed in real time for diagnostic purpose and for starting and stopping the acquisition system. The offline analysis of the data is also implemented in ACQU. This process decodes the content from the ADCs to build physical quantities like the momentum and the energy of the particle. This part of the software can be changed by the users.

⁶The pedestal is an offset, on which the genuine signal sits, in QDC devices due to a constant current present at the input of the QDC gate.

Chapter 4

Detector calibration

In a three-fold coincidence experiment the calibration of time signal of the detectors is a very important issue. In this chapter the calibration of the tagger, the TOF and the HpGe together with the DSSDs are presented.

4.1 Start detector

The start signal is made from the first *HpGe* crystal of any of the Germanium hodoscopes whenever one output exceeds the lower threshold of the leading edge discriminator, as explained in section 3.6. The start pulse is the origin in the time axis of an experiment, the instant at which the equipment starts recording the event. The start time Δt_{start} is the time from the start pulse to the instant the reaction took place. The start time is needed to reconstruct the actual time of flight of one particle from the reaction vertex to the detector where it is registered.

As with any time signal coming from a leading edge discriminator the start time is pulse-height dependent and therefore a walk correction, see section 3.6.2, has been made. The pulse-height of the first crystal was plotted against the time signal of the tagger still not corrected for the start time. The data used for the calibration were those collected in the tagging efficiency modus (section 4.2.2). The spectrum in Fig. 4.1 shows the plot in case of a normal triple coincidence trigger. The left panel shows the spectrum before the walk correction where the walk effect is recognisable in the slightly curvature of the peak. The right panel shows the spectrum after the walk correction. The walk correction parameters, the rise time and the walk offset, are different for different type of particle. This means that the rise time is energy and depth dependent. This is quite unusual since the response of the semiconductor detector to ionising particles is independent on the particle type. The reason for this behaviour is understood to be due to the short charge collection time used. The typical collection time for Germanium detectors is a few μs [50] but for this

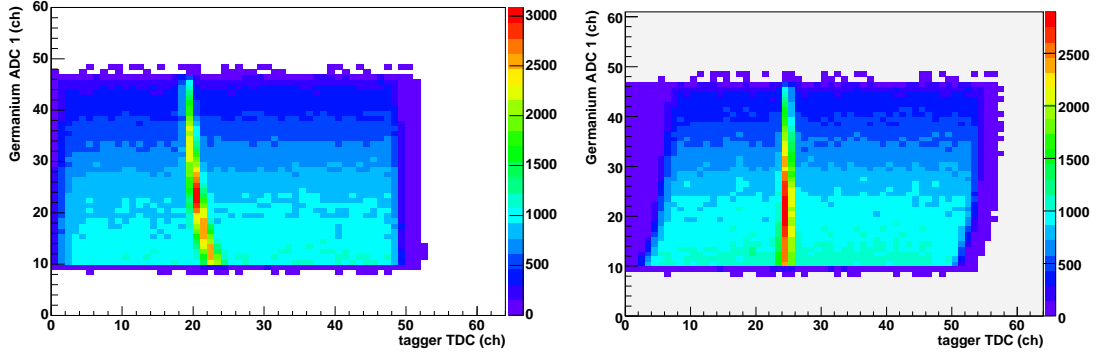


Figure 4.1: pulse-height of Germanium first disc versus the time of the tagger without any walk correction for the Germanium, left panel, and after walk correction, right panel.

experiment 500 ns, the time window for the integration of the charge, was used in order to increase the acceptable events rate. In this short time not all of the charge could be collected, particularly the holes since they have a slower mobility in the material than the electrons [50]. The mobility is defined as the magnitude of the drift velocity per unit electric field:

$$\begin{aligned}\mu_e &= |v_e|/E \\ \mu_h &= |v_h|/E\end{aligned}\tag{4.1}$$

and is temperature dependent. At room temperature, 300 K, μ_e is $3900 \text{ cm}^2/Vs$ while μ_h is $1900 \text{ cm}^2/Vs$, as stated in [50]. Moreover some of the crystals were not fully depleted hence the charge carriers got lost in the dead-layers.

4.2 The Tagger

In order to reconstruct an event the time relation between the tagged photon and the other experimental detectors is required. For this reason a good time resolution in the tagger is as important as the energy resolution. In the following two subsection time and energy calibrations are described briefly.

4.2.1 Tagging efficiency

As explained in section 3.2.1 the photon cone is reduced at the collimator so the number of the photons impinging upon the target, N_γ , is not the number of electrons

counted at the focal plane detector, N_e . The ratio of these two numbers gives a measure of the photon transmission efficiency called tagging efficiency for each tagger channel i :

$$\epsilon_t(i) = \frac{N_\gamma(i)}{N_e(i)}, \quad (4.2)$$

which is always less than 1. To calculate this ratio a direct measure of the tagged-photons and the post-bremsstrahlung electrons must be made and to do this the electron beam is operated at low intensity so that randoms are suppressed. The Pb-glass detector is placed in the beam line at a fixed distance after the photon collimator and its signal strobes the level-one trigger. The number of coincidences between the photons in the detector and the specific i th channel in the focal plane, the $N_\gamma(i)$, are counted using the Pb-glass detector. The number of electrons in the i th tagger channel, $N_e(i)$, are recorded by scaler whether in coincidence with a photon or not. Before measuring the tagging efficiency a background run is done. The beam is switched off and the Pb-glass is inserted in the photon beam line. This is a measure of the natural background present in the hall and has to be subtracted from the data collected in the tagging efficiency run. In Fig. 4.2 panel a) the spectrum of the time signal of the tagger in coincidence with the Pb-glass detector for a tagging efficiency run is shown; in panel b) the time signal of the tagger in coincidence with the Germanium detector in a triple-coincidence-trigger run is shown. At low beam intensity there is effectively no random background, which appears at high electron rates, panel b).

4.2.2 Photon Time

The tagging efficiency run is also used to align the channels of the focal plane detector with respect to the time. Each PM has a different gain and a different cable length which causes the individual signal to arrive at different times. The time from the radiator to a fixed channel in the focal plane is the same for all the electrons following that curvature. The bremsstrahlung photons from the radiator all reach the Pb-glass at the same time. The difference between these two times is constant for a given tagger channel. Therefore a plot of this time difference should give a sharp peak at the expected time s/c , s being the electron flight path in the dipole magnet and c the velocity of light. Any deviation from the expected time position is corrected for with the use of a time offset to be subtracted from the TDC value. Fig. 4.3 shows the energy of the photons as a function of the tagger time in coincidence with the Pb-glass, this is the time from when an electron is detected in the focal plane detector to the moment the corresponding photon is detected in the Pb-glass. The left panel shows the tagger channels before alignment and the right panel shows them after alignment where they now form a straight line.

The time information t from the TDC, corrected for the different cable length

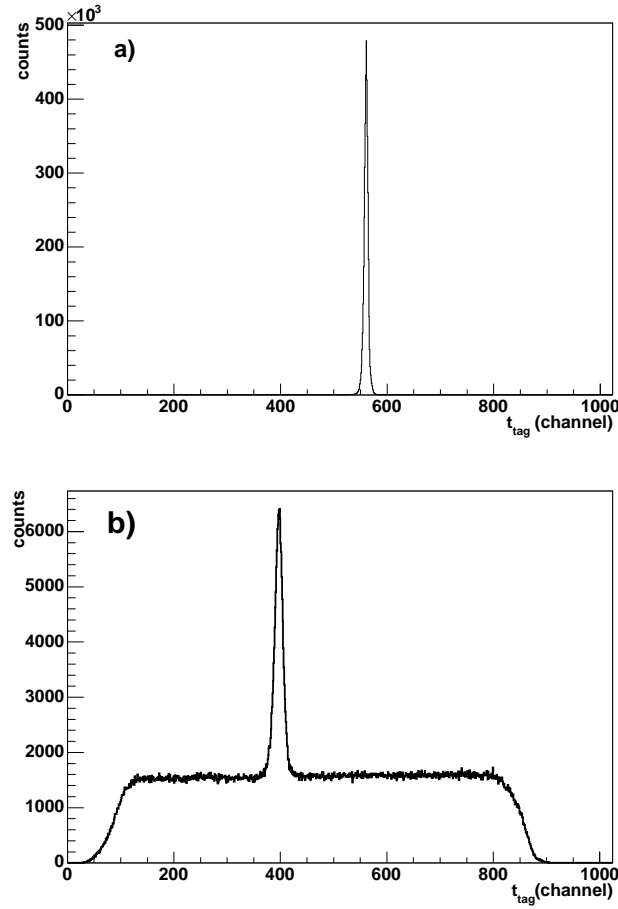


Figure 4.2: a) Time spectrum for coincidence between the tagger and the Pb-glass detector in a tagging efficiency run. b) Time spectrum for coincidence between the tagger and the start detector in a triple coincidence trigger run.

and the different PM gain, represents the time difference between the moment the electron hits one detector in the focal plane and the instant one of the reaction products reach the Germanium hodoscope, first level trigger. The actual time of flight of the photon to the vertex of the reaction from the radiator is then obtained from the difference between the time corrected t and the start time Δt_{start} :

$$t_{tag} = t - \Delta t_{start} \quad (4.3)$$

In figure 4.4 the t_{tag} histogram is shown. The prompt peak is due to the coincidence between electrons in the focal plane detector and photons at the target. The electrons which are not correlated with any photons are responsible for the background. These can be caused by electrons which undergoes collisions with the electrons in the radiator and electrons which are scattered from the environment in the hall and

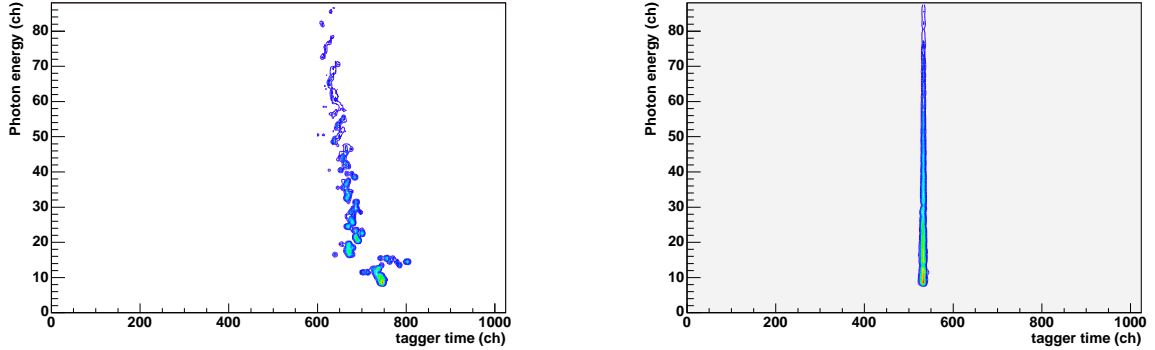


Figure 4.3: Photon energy versus the time of the tagger in coincidence with the Pb-glass in a tagging efficiency run. The upper panel is before channel alignment while the lower panel after.

electrons which produced photons in the tail of the angular distribution which are rejected by the collimator. For one event several electrons are detected in the focal plane only one of which is the one that produced the photon which induced the reaction or possibly none. For the spectrum in Fig. 4.4 the trigger is given by any proton detected in Panoramix. A cut on the proton ridge in the $\Delta E/E$ plot, Fig. 4.11 lower panel, is required. Since the low energy protons are also of interest some pions lying in the diagonal of the $\Delta E/E$ plot are selected as well. The light mark to the left of the proton peak is believed to be due to these pions because when the Fig. 4.4 is remade where pions are selected rather than protons the pion coincidence peak appears at the same channel number as this small bump. The width of the prompt peak gives the time resolution of the tagger in coincidence with the Germanium hodoscope. The width of the peak in Fig. 4.4 is fit with a Gaussian of $\sigma = 2.9$ ns, a factor three bigger than the sigma of previous (γ, NN) experiments using the same scintillator detectors, the PiP-TOF experiment of [62]. This is due to the fact that scintillator detectors have a faster time response than solid state detectors, but the latter give a better energy resolution.

4.2.3 Photon energy

The energy of the photon is the difference between the 855 MeV of the incoming electron beam and the energy of the deflected electron detected in the focal plane. During the experiment the strength of the magnetic field was constantly monitored using a nuclear magnetic resonance (NMR) probe. The value of the strength of the magnetic field was used to calculate the trajectories of the electrons to the focal plane detector. The hit position in the focal plane detector can be mapped to the electron energy. Every channel can measure an energy bite of circa 2 MeV, which

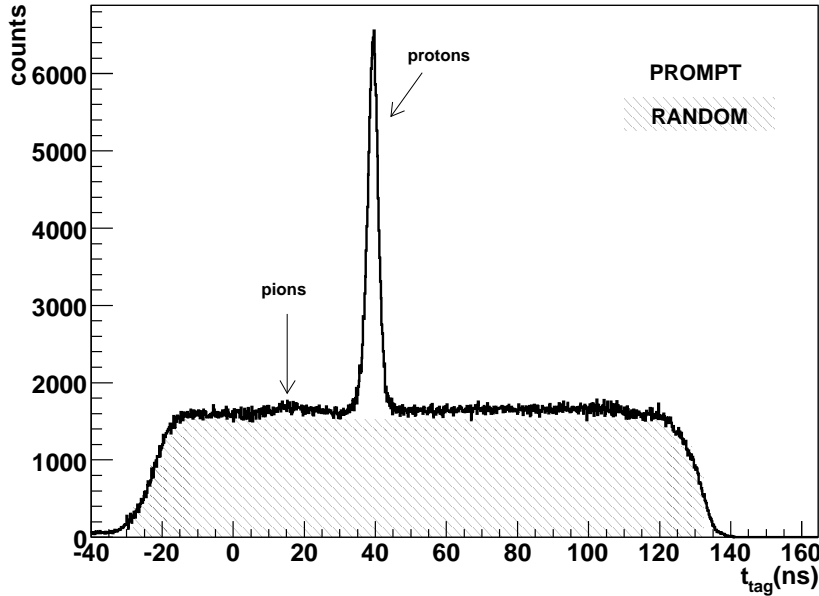


Figure 4.4: Time of the tagger after alignment in coincidence with the start detector.

sets the scale for the resolution of the photon energy.

4.3 DSSD

The DSSDs are used for tracing the trajectory of the particle from the target to the Germanium hodoscope. The energy deposition in the thin silicon layer is comparable to energy losses in other dead layers and is smaller compared to the particle energy range we are looking at; therefore no precise energy information is required. The particle energy losses in the strip detectors are then calculated as they would be in a dead layer and added to the energy measured in the Germanium hodoscope as will be explained in section 5.1.2.

4.3.1 Pulse-height calibration

The QDC signal of each strip channel needed to be mapped to physical units, MeV, representing the energy deposited in the silicon strip. Each QDC signal has a characteristic gain because each of the strip is single amplified and read-out. In a plot of the signal of the vertical strip against the signal of the horizontal strip it was possible to calibrate the gain of each QDC channel. In Fig. 4.5 in the left panel

the histogram for the non aligned channel is shown, in the right panel is the same plot after alignment which was reached by applying a correction factor at each QDC channel.

Each QDC signal showed a peak due to relativistic particles which was removed by applying a lower limit for each channel.

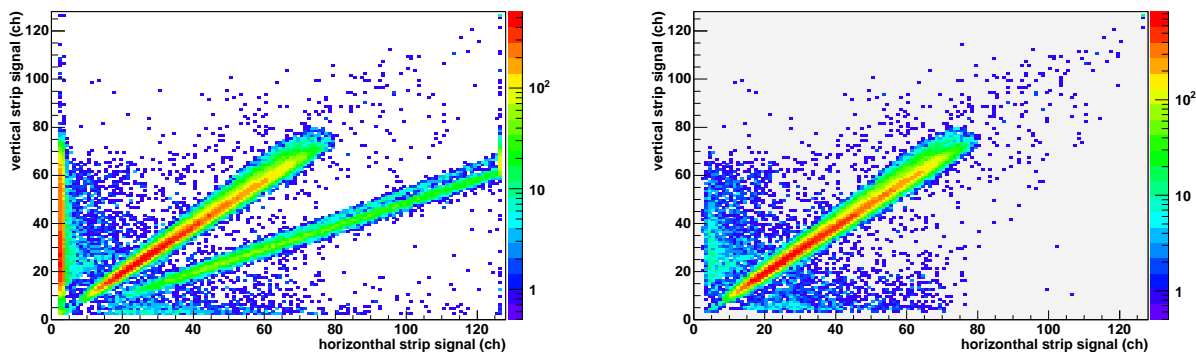


Figure 4.5: Vertical strip signal against horizontal strip signal before and after alignment.

4.4 Germanium hodoscope

For Germanium detectors the QDC signal, when the crystal is completely depleted, is directly proportional to the energy deposited by the charged particle. Before mapping the QDC channel number to the energy deposition it is necessary to check the linear response of the preamplifiers.

4.4.1 Linearity

In order to check the linear response of the preamplifiers a series of pulses were fed in into the pre-amp input test of each crystal on each detector. This procedure was done at two different signal attenuations, 18 dB (low) and 38 dB (high). The experimental data were collected with the high attenuation, while data taken with radioactive sources were taken with the low attenuation. In Fig. 4.6 an example of the pulser output for the second crystal of Panoramix is shown. As can be seen the behaviour is clearly linear, the axis intercept is close to zero and this value represents the pedestal of the signal which has to be subtracted from the raw data. However, the axis intercept of the linear fit to the high attenuation data differs from that of the fit to the low attenuation data. A correction for this difference was made when translating the peak position of the radioactive source from the low to the

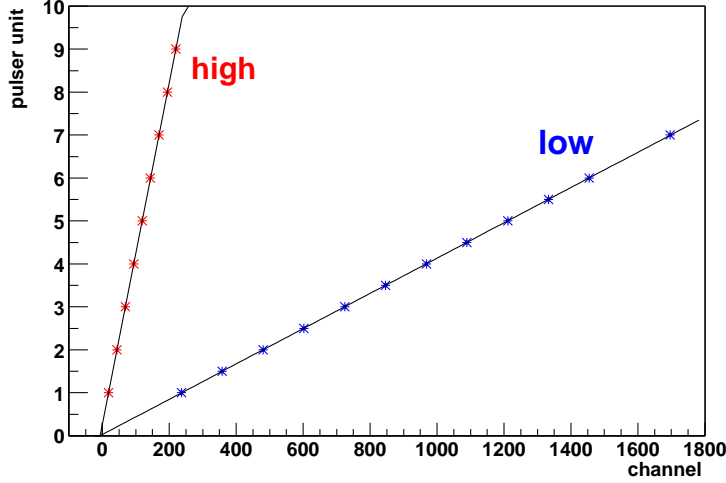


Figure 4.6: Pulser output of the 2nd crystal in Panoramix (stars) for two different attenuations. The lines are linear fits to the data.

high attenuation channel space. In this way the pedestal subtraction is no longer required as it is accounted for in the correction.

4.4.2 Energy calibration

An ionising particle in a material has a characteristic average energy loss per unit path length, normally called stopping power. The quantum mechanical calculation of the stopping power is from Bethe, Bloch and other authors. The formula is known as Bethe-Bloch formula [50]:

$$-\frac{dE}{dx} = k\rho\frac{Z}{A}\frac{z^2}{\beta^2}\left[\frac{1}{2}\ln\left(\frac{2m_e\gamma^2v^2T_{max}}{I^2}\right) - \beta^2 - \frac{\delta}{2} - \frac{C}{Z}\right] \quad (4.4)$$

with $k = 4\pi N_a r_e^2 m_e c^2$, where r_e and m_e are the classical electron radius and mass respectively, ρ is the density of the absorber, Z it's atomic number and A it's atomic weight. For the projectile z is the charge number in electron units and β is the velocity over c . γ is the Lorentz contraction factor, T_{max} is the maximum energy transfer in a single collision and I is the average ionisation potential. The δ and the C are shell and density correction factors. The δ is important at high energies while the C is important at low energies. At non-relativistic energies, as the energies in this experiment, the dE/dx is dominated by the z^2/β^2 term so the energy loss decreases with increasing particle velocity, or in other terms with increasing energy until a minimum is reached; this is called minimum ionising and it is equal for particles

with the same charge number. After this minimum the \ln -term becomes important therefore the range rises again but slowly because the density and shell corrections cancel this relativistic rise.

The quantity which describes the average penetration of a particle in a material is called the range and is dependent on the material type and on the energy and type of the particle. The range is calculated by integrating over the stopping power. The range is approximatively proportional to the incoming kinetic energy of the particle to the power of a constant b :

$$R \propto E^b \quad (4.5)$$

where the constant depends on the energy of the particle and on the medium. In

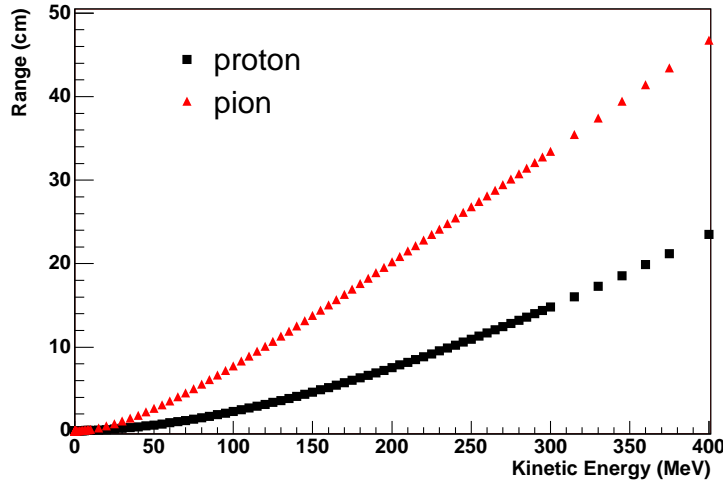


Figure 4.7: Range in Germanium for protons (black square) and pions (red triangles) as a function of their kinetic energy.

Fig. 4.7 the range as a function of the kinetic energy in Germanium for protons and pions is shown. Protons up to 250 MeV energy can be stopped in about 10 cm of Germanium which is the average total thickness of the Edinburgh hodoscope as reported in table 3.1. The relationship between range and energy is stored in range tables. In our case range tables are produced by integration of the stopping power formula as calculated by the method of Ziegler [71].

In a $\Delta E/E$ plot the energy loss in one crystal is plotted against the energy deposited in the following one. As one can see in the histogram of the upper panel of Fig. 4.8 the protons lose some energy in the second crystal show a typical dependence on the inverse of the proton energy as the energy loss is proportional to $1/\beta^2 \simeq 1/E$ at non-relativistic energies where E is the energy in the second layer. More energetic protons pass into the third layer represented by the second branch in the histogram. The point where the curve discontinues (changes direction) is called punch-through

and represents the point where the proton stops at the back in the second layer.

The range method

The range method which is based on the relationship between range and kinetic energy was used to calibrate the energy of the Germanium hodoscope. The range for a proton in Germanium for kinetic energies in the range from 1 MeV to a maximum of 250 MeV is extracted from range tables. Let E_1 be the energy of the incoming proton. At low energies the proton stops in the first crystal and are not seen in the $\Delta E/E$ plot of Fig. 4.8. For protons which pass through and stop in the second crystal the range R_1 corresponding to the incoming energy is extracted from range table. The energy the proton has just after leaving the first layer E_2 corresponds to the range $(R_1 - d_1)$ where d_1 is the active thickness of the first layer. The energy loss ΔE_1 in the first layer is then the difference between the incoming proton energy and the energy in the second layer

$$\Delta E_1 = E_1 - E_2 .$$

Since the proton stops in the second layer $\Delta E_2 = E_2$, therefore the two points describing the first branch in Fig. 4.8 are $(E_2, \Delta E_1)$. Protons with energy higher than the stopping power for the two crystals, around 100 MeV, pass to the third crystal. For these protons the energy loss ΔE_2 is calculated in the same way as ΔE_1 with incoming energy $E_2 = E_1 - \Delta E_1$ and active thickness of the layer d_2 . The two points describing the second branch in the spectrum of Fig. 4.8 are $(\Delta E_2, \Delta E_1)$ calculated as described. The red line in the spectra of Fig. 4.8 is the result of this calculation for the two Germanium crystals. The crosses trace the maximum of the measured ridge for a better understanding of the histogram. The conversion factors, gain and offset, from QDC channel to energy are adjusted until the calculated curve fits the measured one. In the $\Delta E/E$ spectrum of the upper panel in Fig. 4.8, showing the energy loss in the first Obelix crystal versus the energy deposited in the second Obelix crystal, the agreement between the expected behaviour and the measured data is achieved with a precision of 5%. The distribution of the difference between the theoretical points and the profile points in the measured curve was calculated and this shows a standard deviation from 0 of 0.05. In the lower panel, showing the $\Delta E/E$ plot for the first two crystals of Panoramix, the agreement between the calculated curve and the measured curve is not good for the branch of proton entering the third crystal. The disagreement is due to the presence of a dead layer either in front of the first crystal or at the rear of the second. The dead layer is caused by the applied voltage being too low, we had -1000 V instead of -1200 V, which made the crystal not completely depleted. It is not possible to correct for the dead layer but an estimate of the thickness of it could be made. In fact the blue line in the lower plot of Fig. 4.8 is a calculation using range method assuming the

active thickness of Germanium in the second layer is 1.2 mm thinner than given by the manufacturer. This line describes the measured data well so we concluded that a dead layer of 1.2 mm is present between crystal one and crystal two. The range method was iterated for all the six layers and was applied to $\Delta E/E$ plots of the other layers in order to determine the calibration coefficients.

Pion ridge method

A different method [54] from the range method was used to make the Germanium energy calibration. Our collaborator, N. Harrington, used pions from the $p(\gamma, \pi^+)n$ reaction from data taken with a CH_2 target, used for 20% of the running time of the ${}^3\text{He}(\gamma, \pi^+){}^6\text{He}$ experiment. Since this is a double coincidence experiment involving only the tagger for the detection of the photon and the Germanium hodoscope for the detection of pions the kinetic energy of the pion for the $p(\gamma, \pi^+)n$ reaction is over determined. Knowing the photon energy from the tagger and the measured pion angle the kinetic energy is known from kinematic calculations [54]. Therefore one can produce two-dimensional histograms of the calculated pion kinetic energy versus the measured kinetic energy at vertex, where the energy losses in the dead layer between the target and the Germanium are included and the 4.12 MeV given to the μ^+ by the pion decay was taken into account. In Fig. 4.9 the 2D plots of this before and after calibration are shown. The events on the diagonal dashed line correspond to pions from the $p(\gamma, \pi^+)n$ reaction, the other events arise from pions from reaction with Carbon present in the target. By adjusting the gain and the offset of the Germanium crystals the pion ridge was aligned to the diagonal. The calibration values found with this method agreed with the ones found with the range method used with protons. A cross-check was done by applying the range method with pions from data taken for the ${}^{16}\text{O}(\gamma, \text{NN})$ experiment. In the calculation of the energy loss also the kinetic energy of 4.12 MeV of the μ^+ was taken into account. In Fig. 4.10 the measured $\Delta E/E$ plot for Obelix is compared to the theoretical range method curves. The energy calibration values extracted using the proton data and the pion ridge method were the same.

4.4.3 Particle identification

The $\Delta E/E$ method is also used to identify particles. As explained in the previous section the energy loss per unit thickness of material at non relativistic energies is proportional to $z^2 m/E$ therefore for the same charge number heavier particles deposited higher energy per unit length. Heavier particles have then a shorter average penetration path in the material as one can see in Fig. 4.7 where 250 MeV protons are stopped in 10 cm Germanium while 250 MeV pions go through it. Therefore in a $\Delta E/E$ plot is possible to label the different particle types according to their mass.

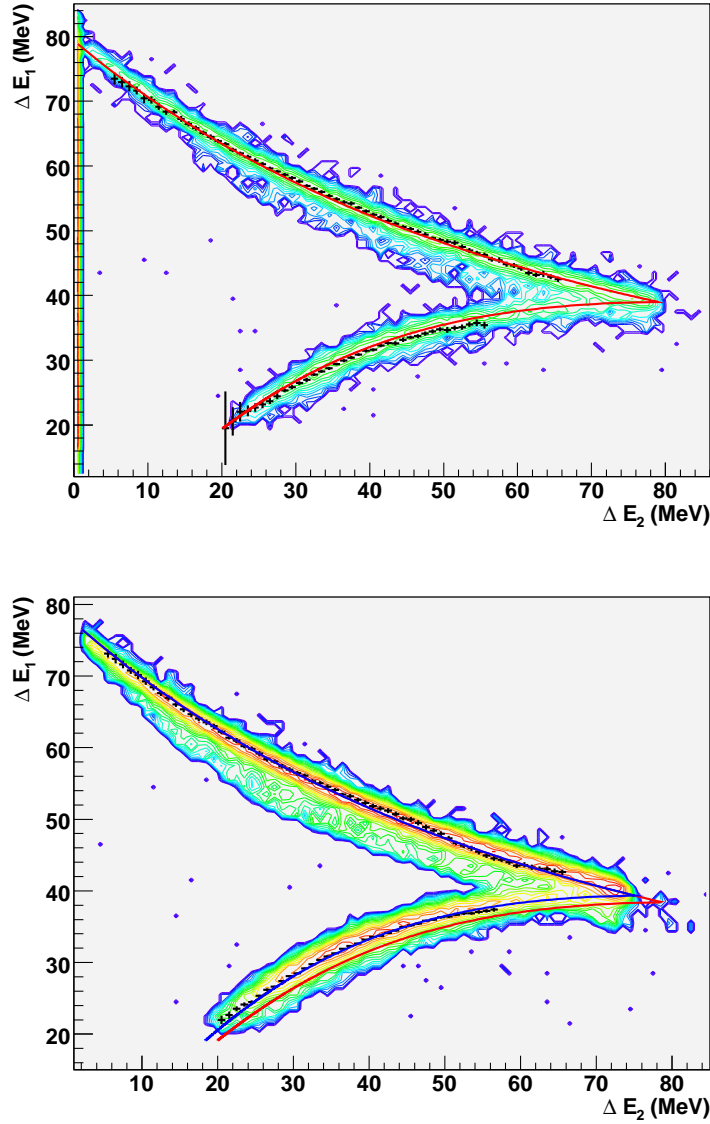


Figure 4.8: Upper panel: proton energy deposited in the first crystal of Obelix against energy loss in the second crystal. The red line is calculation from Bethe-Block formula. Lower panel: $\Delta E/E$ spectrum for Panoramax. The red line is a calculation assuming the declared Germanium thickness. The blue line is calculated assuming a 1.2 mm dead layer in the second crystal. In both figure the crosses are profile histograms.

Each particle will leave a well separated branch in the Germanium. In the upper panel of Fig. 4.11 the energy loss in one of the strip is plotted versus the energy deposited in the first Germanium crystal. The tritons are visible. In the lower panel of of Fig. 4.11 the energy deposited in the first crystal is plotted against the sum of

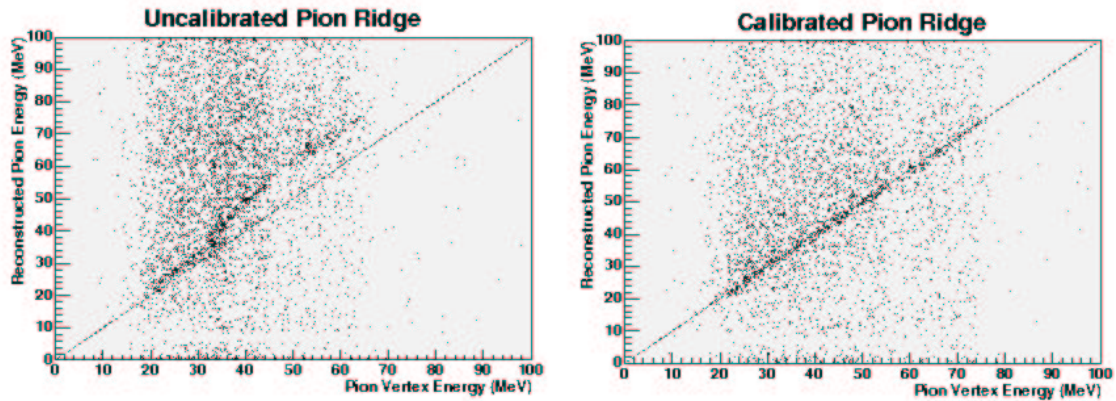


Figure 4.9: Calculated pion kinetic energy versus measured energy at the vertex for the first three crystals of Panoramix. The histogram on the left hand side is with approximate Germanium energy calibration and the histogram on the right hand side is after the final calibration [54].

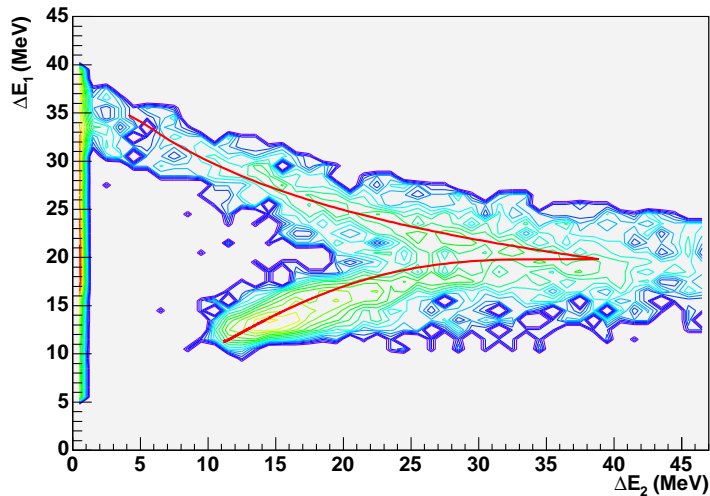


Figure 4.10: Pion energy deposited in the first crystal of Obelix against energy loss in the second crystal. The red line is a calculation assuming the declared Germanium thickness.

the deposited energy in each crystal. The diagonal represents the particles stopping in the first crystal, higher energetic particles can travel into the layers behind leaving the typical banana shape in the spectra. One can clearly distinguish the pion ridge at the bottom, the proton ridge in the middle is most populated and above this the deuteron ridge.

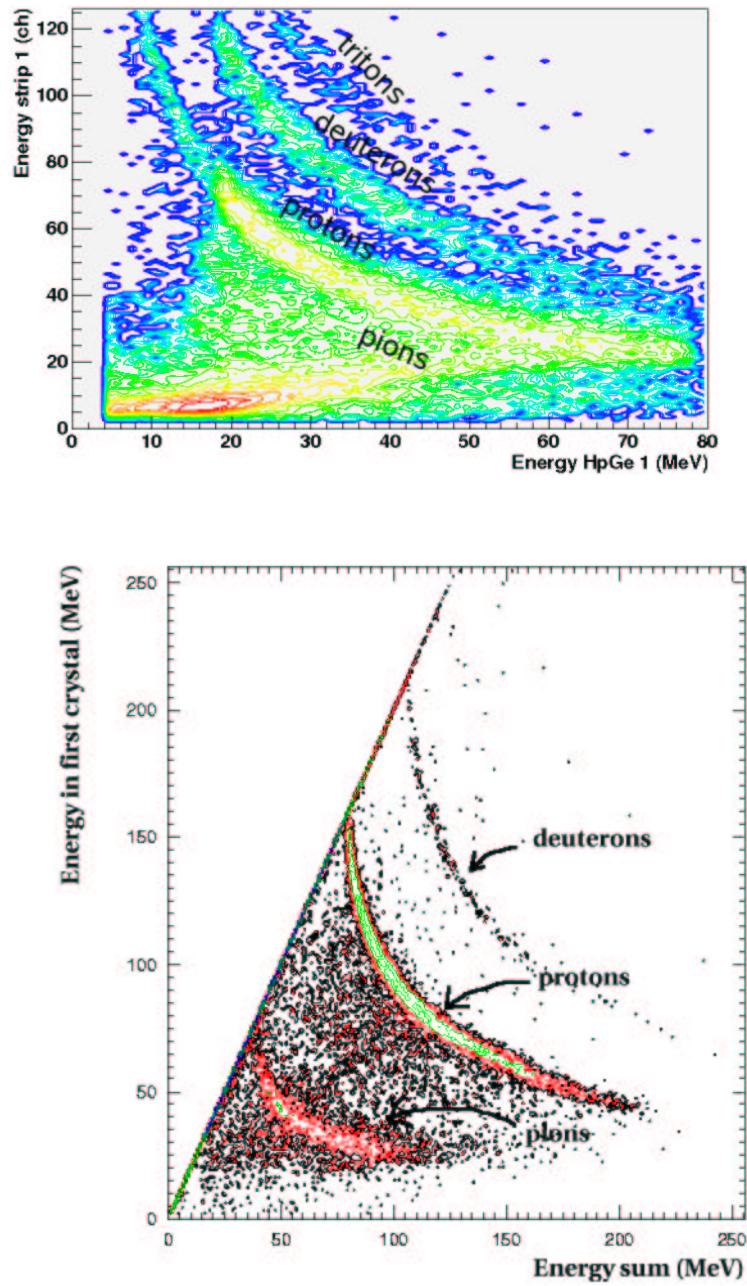


Figure 4.11: Upper panel:Energy in the horizontal strip 1 against the energy loss in the first $HpGe$ crystal. Lower panel:Energy loss in the first $HpGe$ crystal against the energy loss in all the crystals for Obelix.

4.4.4 Test at the PSI

The first Germanium hodoscope to be delivered has been tested [54, 55] at the Paul Scherrer Institut (PSI) in Villigen, Switzerland, where a main proton beam with 590 MeV energy produces seven secondary π^\pm and μ^\pm beams [56]. The detector was positioned in one of the seven secondary beam line with the axis along the beam such that the beam spot was in the middle of the first crystal. This secondary line delivers a π^+ beam with 5% proton contamination at 300 MeV/c proton momentum. A check of the linearity of the preamplifier with the pulser walk-trough as explained in section 4.4.1 was made. The QDC channels of the first crystal were mapped to the energy by using the contamination protons present in the beam. A proton beam momentum of 230.05 MeV/c was used and the contamination protons impinging in the first crystal have an energy of 26.3 MeV. By selecting different smaller beam momenta another three photon energies could be fixed. The 26.3 MeV protons are the highest energetic protons which reach the Germanium hodoscope and for this energy they are stopped in the first crystal therefore the calibration values for the other crystals were determined using the calibration of the 1st crystal and the pulser walk-trough.

In Fig. 4.12 the energy deposited in all the six crystals for a beam momentum of 215 MeV/c is shown. A well defined proton peak at 22.7 MeV and a pion peak at 120.7 MeV were seen. The broad peak at around 95 MeV are muons which deposited only part of their energy in the detector. A Gaussian fit to the proton peak showed a FWHM of 366 keV. The intrinsic proton energy resolution for the first crystal of the Germanium array is better than this since the beam energy resolution has to been taken into account.

4.4.5 Proton detection efficiency

The average energy to create an electron-hole pair in Germanium is 2.96 eV [50]. Since the lower proton energy threshold is 15 MeV (see section 3.6.1) there will be enough electron-hole pairs produced for the proton to be detected at this threshold and above. For this reason and neglecting the hadronic interaction the detection probability of charged particles with energies from 15 MeV is taken to be 100%.

4.5 TOF

The kinetic energy and momentum of the neutron are calculated via the time of flight, t_f , which is the time taken for the neutron to travel from the vertex of the reaction to the stopping point in the scintillator. The corresponding distance is

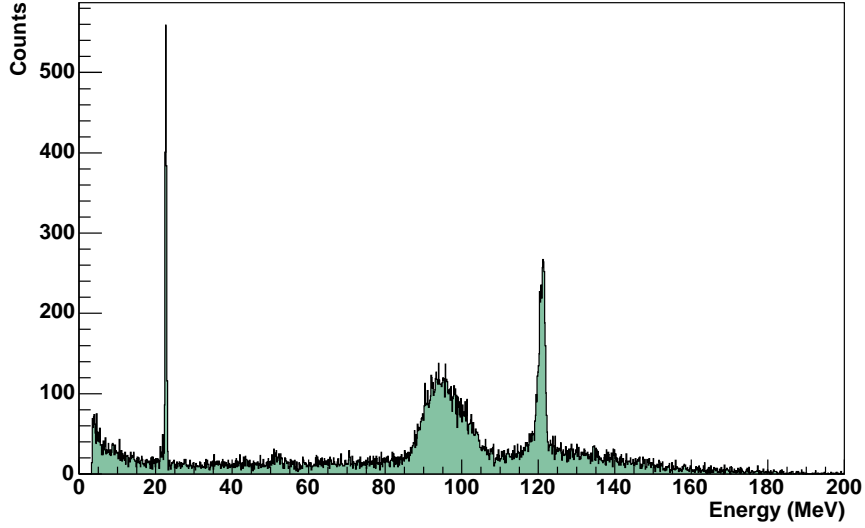


Figure 4.12: Energy deposited in the six Germanium crystals for a beam momentum of 215 MeV/c [54]

the flight path, f_p , this is the distance from the target to the impact point in the scintillator. From the f_p and the t_f is possible to calculate β :

$$\beta = \frac{v_N}{c} = \frac{1}{c} \frac{f_p}{t_f} \quad (4.6)$$

where c is the speed of light. The relativistic kinetic energy is then:

$$T_N = (\gamma - 1) m_N \quad (4.7)$$

where m_N is the mass of the nucleon and γ is the Lorentz contraction factor. The modulus of the relativistic momentum is:

$$p_N = m_N \gamma \beta. \quad (4.8)$$

The resolution of the time of flight is very important to achieve a high neutron energy resolution.

4.5.1 Walk correction

The time information from the TDC is affected by signal walk because comes from a leading edge discriminator. The walk parameters described in section 3.6.2 were determined by fitting the time-amplitude spectrum for each PM. The data were

taken using the light emitting diode flasher, see section 3.5.1. The intensity of the input light signal of the flasher was varied [60] by changing the distance between the light source and the connectors. The time corresponding to the different pulse-height amplitudes crossing the threshold, a_0 , of 16 mV, was measured. A fit to the data in the time versus pulse-height spectrum is made according the following parametrisation:

$$t = t_0 + r \sqrt{\frac{a_0}{q - p}} \quad (4.9)$$

where p is the QDC pedestal. In the calibration parameter file a rise time and pedestal value is stored for each PM.

4.5.2 The t_0 calibration

Using the walk corrected times t_1 and t_2 the mean value of the time information from the top and the bottom PMs is calculated:

$$t_m = \frac{(t_1 + t_2)}{2}. \quad (4.10)$$

The t_m represents the time from the start pulse to the PMs. Since the sum of the light propagating times from the hit position to the ends of the bar is constant the t_m is not dependent on the hit position in the material [58]. The time of flight is obtained from the t_m with the t_0 and the start time corrections:

$$t_f = t_m + \Delta t_{start} - t_0. \quad (4.11)$$

The reaction of interest takes place before the TDC started counting so the start time has to be added to the time information in order to get the time from the vertex to the hit position in the bar. The t_0 is an offset due to delays of the signal in the 25 m cables, in the electronics and in the trigger logic. Relativistic particles which originate mainly from photons that are produced from atomic scattering in the target or from the decay of pions are used to determine the t_0 values. Their velocity is c and the corresponding flight path from the target to the detector is known from the geometry of the experiment. The relativistic particles are then expected to arrive at a time $t_{rel} = \frac{f_p}{c}$. For each scintillator bar all the relativistic particles form a peak. The mean of the Gaussian fit to it gives the t_0 value. This is then entered in the calibration database.

A very suitable observable to check the t_0 calibration is the inverse velocity, defined as the ratio of the time of flight to the flight path, $\frac{tof}{f_p}$. Because the flight path dependence is removed the relativistic peak is aligned for every scintillator bar if the time offsets have been correctly determined. In Fig. 4.13 the inverse velocity for all the scintillator bars is shown. The relativistic peak sits atop the background

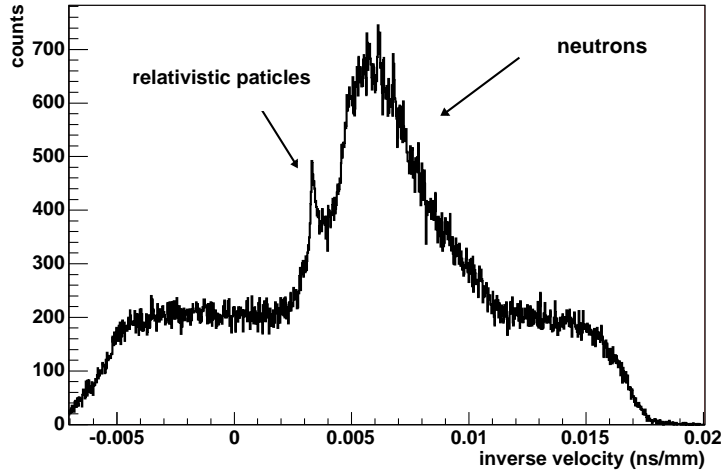


Figure 4.13: Sum of the inverse velocity for all the scintillator bars; full statistics with Panoramix as the start detector.

at the expected position of $\frac{1}{c}$ ($3.3365 \cdot 10^{-3}$ ns/mm). The correct position of the relativistic peak shows that the t_0 calibrations are reliable and the TOFs are correctly aligned. Behind the photon spike a broader peak is present which is due to detected neutrons, these are slower and spread out in a wider time range. A fine tuning of the t_0 values could be made by looking at every single inverse velocity spectrum. In Fig. 4.13 the start detector was Panoramix, where the DSSDs in front were installed and working. A condition in the analysis of the data was that the strips must have fired, this removes particles which do not originate in the target but the surrounding environment. In Fig. 4.14 the inverse velocity spectrum with Idefix as start detector is shown. Here the DSSDs were not mounted and the detector is positioned at forward angles. The ratio of photons to neutrons is greater than for Panoramix because the relativistic particles are predominantly ejected in a forward direction and the DSSDs filter some of them. The data where Idefix gave the start signal were used for calibration purposes since there are higher statistics. The Idefix data were not used to produce real triple coincidences because of the huge random background which was not easy to suppress in the absence of a DSSD.

4.5.3 Position calibration

Charpak [63] stated that in a long bar of plastic scintillator the impact position of an event can be determined using the difference of the two time signals from the PMs at both ends of the scintillator bar. The time difference is directly proportional to the position of the hit, defined as y in the following description. If one assumes

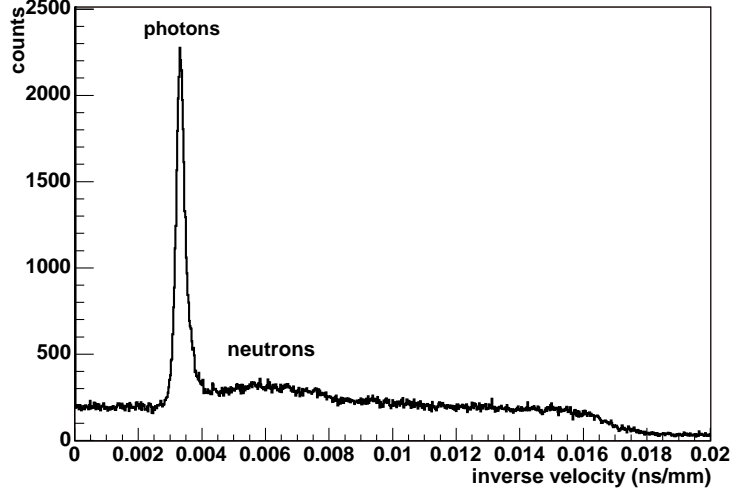


Figure 4.14: Sum of the inverse velocity for all the scintillator bars; full statistic with Idefix as the start detector.

the origin of the reference system of the bar to be in the middle, the time signals can be written:

$$\begin{aligned} t_1 &= \frac{L/2 - y}{c_{eff}} \\ t_2 &= \frac{L/2 + y}{c_{eff}} \end{aligned} \quad (4.12)$$

where c_{eff} is the effective velocity of light inside the scintillator material because the light takes, on average, a longer path than the direct way to the PM and is:

$$c_{eff} < \frac{c}{n}, \quad (4.13)$$

where c is the speed of light in vacuum and n the refractive index of the scintillator material. The linear dependence between time difference, $\Delta t = t_1 - t_2$, and y is the following

$$y = \frac{c_{eff}}{2} \Delta t \quad (4.14)$$

If the origin of the system is not in the middle of the bar an offset, y_0 , is needed in eq. 4.14. The two coefficients c_{eff} and y_0 are calculated by looking at two dimensional spectra of mean pulse-height versus position [65]. Here the two ends of the scintillator bar can be clearly seen as shown in Fig. 4.15, where the vertical lines mark the end of the scintillator bar. The calibration coefficients could be adjusted to reach the final hit y position between 0 and 300 cm. The position is known with a resolution

of in average 10 cm per bar.

Flight path calculation

For this experiment the origin of the y -axis in the laboratory system was at the height of the photon beam. To reconstruct the flight path f_p the z and x hit coordinates in the laboratory system are also necessary. The Cartesian components of the flight path are:

$$\begin{aligned} f_{px} &= f_{pb} \cdot \sin\theta_b + x_b \\ f_{py} &= y \\ f_{pz} &= f_{pb} \cdot \cos\theta_b + z_b \end{aligned} \quad (4.15)$$

where f_{pb} is the flight path at beam height; the distance between the target point and the point at the beam height in the middle plane of the bar, the middle plane is the plane surface half-way between the front and rear surfaces of the bar. θ_b is the in-plane angle, which gives the direction of the incident particle and x_b and z_b are the coordinates of the hit in the bar system with respect to the bar middle plane. The frame coordinates take into account the thickness of the bar and the incident angle of the incoming particle assuming the target is point like. If the incident particle is charged the front surface of the detector is used as reference plane in the bar system. The f_{pb} , the in-plane and the out-of-plane angles of each scintillator bar, with respect to the middle plane of the bar, are calculated via a triangulation of the frames from a base chosen along the photon beam line. The procedure is described in detail in [72]. In table 4.1 the values of the in-plane, out-of-plane and solid angles for each stand are reported.

The two major contributions to the uncertainty in the flight path are the uncer-

July setup	in-plane angle(degree)	out-of-plane angle(degree)	solid angle(sr)
Stand V	5.9 - 11.8	30.1 - 49.1	0.0258
Stand IV	15.7 - 21.8	17.8 - 24.2	0.0165
Stand III	26.5 - 32.8	12.7 - 15.8	0.0121
Stand II	35.6 - 43.8	13.2 - 15.7	0.0388
Stand I	42.9 - 52.6	13.4 - 15.7	0.0530

Table 4.1: In-plane and out-of-plane angles in the laboratory system for the TOF stands for the July setup. The first number of the in-plane angles is the middle plane angle of the left-most detector bar and the second of the right-most one. The maximum and minimum values of the out-of-plane angles are given. The solid angle is the average of the solid angles of each frame, and the solid angle for each frame is the sum of the solid angles of each detector bar.

tainty in the flight path measurement at beam height and the uncertainty in the hit position. The total uncertainty in the flight path at the beam height is determined to be 5 cm arising from the precision of the ultra sonic device, which was used to measure the distance for the triangulation, stated as being smaller than 1 cm and from the systematic uncertainty in the measurement. This arises from the dimension of the device and the way it was positioned on the detectors in order to measure. From the propagation of the error the contribution from the hit position uncertainty is a factor 10 smaller than the contribution from the uncertainty of the flight path at beam height. Therefore the f_p is known with an error not smaller than 5 cm.

4.5.4 The pulse-height calibration

The light produced in a scintillator bar from the impact position of the neutron propagates in all directions. Part of it reaches the PM directly while another part is reflected on the walls before reaching the PM. There can be total and partial reflections, depending on the incident angle, but the latter are minimised by the Aluminium foil used to wrap the scintillator. The attenuation of the light follows the exponential law for the bulk:

$$\begin{aligned} n_1 &= n_0 e^{-\frac{y}{\lambda}} \\ n_2 &= n_0 e^{-\frac{-(y+L)}{\lambda}} \end{aligned} \quad (4.16)$$

where n_i are the number of photons, y is the hit position in the bar, L the length of the bar and λ is the attenuation length which is less than the 6 m is given by the manufacture; the recent calibration of the TOFs showed an average attenuation length of around 3 m [64]. The exponential attenuation of the light makes the pulse-height, q , position dependent and with the use of discriminators the pulse-height threshold is position dependent also. Since the neutron detection efficiency depends on the pulse-height threshold a new position-independent observable can be created, the geometrical mean [59] of the two pulse-heights:

$$q_m = \sqrt{q_1 \cdot q_2} \quad (4.17)$$

since the product of the exponentials removes the position dependence [59]. In thick scintillation bars the geometrical mean is still position dependent [63] though. The intensity of q_m is larger when the particle hits the bar close to one end. This effect is due to the variation of the ratio of direct light to reflected light, and is called droop. The droop is visible in a plot where the pulse-height mean is plotted as a function of hit positions, in the upper panel of Fig. 4.15 an example is shown. The high pulse-height close to both ends of the bar decreases slowly towards the middle of the bar where it reaches a minimum. Corrections for the droop were done [65] and in the lower panel of Fig. 4.15 the pulse-height mean versus position for the same

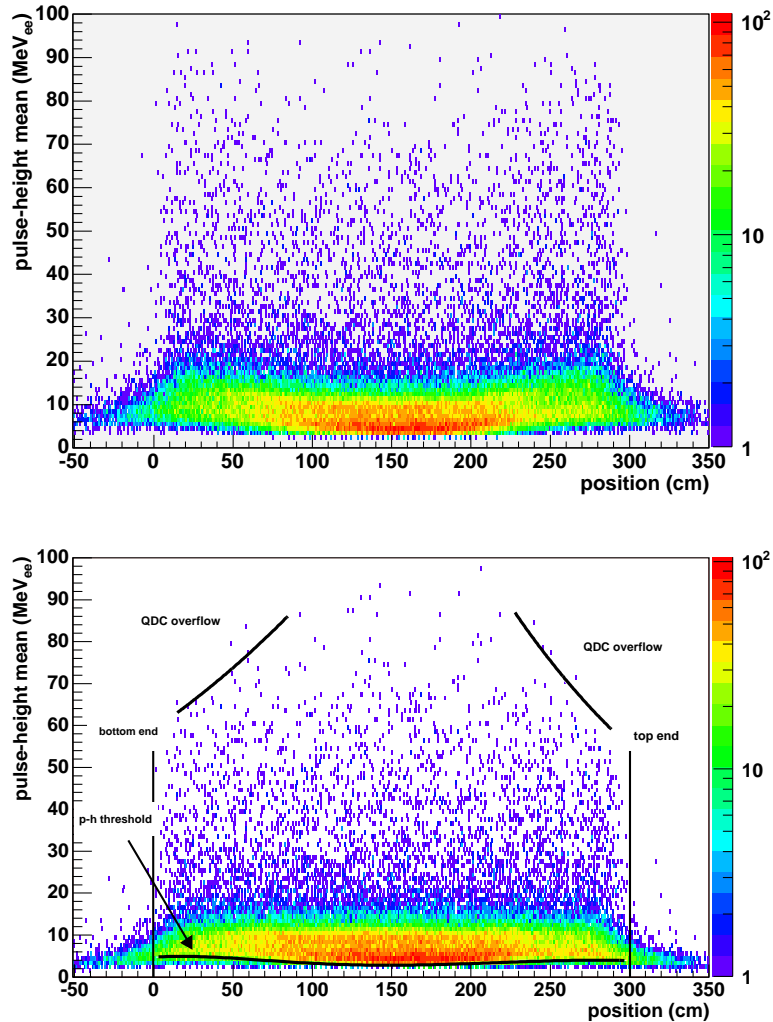


Figure 4.15: Light output of the mean pulse-height of the two PMs versus hit position in the bar before (upper panel) and after (lower panel) droop correction. The curved line on the bottom represents the hardware pulse height threshold whereas the two exponentials are fits of the QDC overflow. Vertical lines shows the very end of the scintillator.

bar after droop correction is shown, as can be seen the position dependence is now nearly all gone.

In order to calculate the neutron detection efficiency the hardware pulse-height thresholds are required and the pulse-heights are converted from channel space into physical units. Protons lose energy along their flight path in a scintillator bar and the energy deposited in the material thickness is described by the Bethe-Bloch formula [50]. In 5 cm organic scintillator protons up to circa 78 MeV can be stopped. The ‘sail’ spectrum where the q_m is plotted versus the time of flight is used to cal-

ibrate the pulse-height. In Fig. 4.16 a sail spectrum for one bar is shown. Protons with energies smaller than 78 MeV impinging perpendicular to the scintillator create an amount of light proportional to their energy until the punch-through point, which is where protons have enough energy to escape the detector. Protons with energies greater than this punch-through value create an amount of light inverse proportional to their energy forming the downward slope to the right of the peak. Incoming protons which are not perpendicular to the surface of the scintillator bar have longer flight paths in the material and consequently, deposit more energy. This gives rise to broad ridges in the sail spectrum, only the inner edges were used for the fit. The fit parameters are then used to rescale the PM pulse-height. A wider description of this method can be found in [60]. For the Veto detectors ‘banana’ plots were used for the pulse-height calibration. The pulse-height mean of the Veto layer was plotted against the pulse-height mean of the TOF bar directly behind the Veto.

Ideally the response of organic scintillator would be linearly proportional to the energy deposited by a charged particle. In reality there are quenching interactions between the excited molecules along the path of the charged particle, which reduce the particle energy and make the light output at the PM smaller. To avoid this problem the unit used for the pulse-height is the electron-equivalent energy since the light output of the PM is directly proportional to the energy deposited by the electrons. In that way the channel can be directly converted in light output.

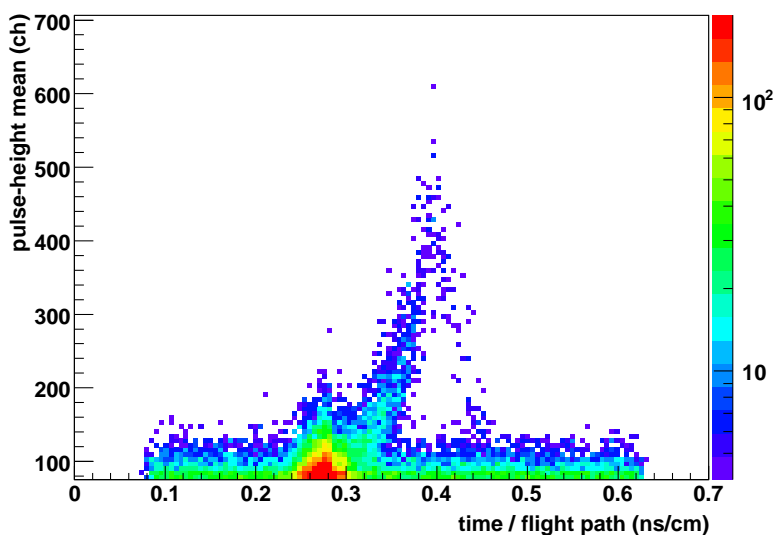


Figure 4.16: Pulse-height mean of two PMs versus the inverse velocity. The peak at 0.3 ns/cm is due to the relativistic particles.

4.5.5 The neutron detection efficiency

Plastic scintillation detectors are composed of hydrogen and carbon. As explained in section 3.5 the neutrons are detected dominantly via the recoil proton from the elastic scattering of the neutron with the hydrogen and from $^{12}\text{C} + \text{n} \rightarrow \text{X} + \text{p}$ reactions. Since these reactions are rarer than the Coulomb interaction the probability for detection is below 100% and is dependent on the thickness of the material. The neutron detection efficiency has to be corrected for and is simulated taking into account all possible reaction mechanisms as already listed in section 3.5. A Monte Carlo simulation developed by Stanton [69] and later improved by Cecil [70] was used to model the neutron detection efficiency for every stack of a complete stand. The neutron detection probability depends on the pulse-height threshold set in the discriminators because a neutron is detected only if its energy deposited is greater than the defined threshold. Therefore the hardware pulse-height threshold must be extracted and used in the STANTON code. In Fig. 4.15 (lower panel) the q_m , as a function of the position, for one scintillator bar is shown. The lower edge of the histogram is due to the hardware pulse-height threshold. Since the threshold varies along the bar a fit was used to describe, a 6th order polynomial giving the best result. In Fig. 4.15(lower panel) at the ends of the bar one can see a cut on the QDC overflow events. An overflow event is recorded when a particle hits the bar very close to one end so that the light signal at the corresponding PM exceeds the upper limit of the QDC. Two exponential curves were fitted to the QDC overflow events and the fit parameters used as a input for the STANTON code. The geometry and the type of scintillator material are also used as input parameters for the code. The neutron detection efficiency has been modelled for two different software thresholds, 5 and 7.5 MeV_{ee}. A higher threshold would improve the resolution but decrease statistics. The output of the code gives the neutron efficiency as a function of the position of the hit in the bar and of the neutron kinetic energy. In Fig. 4.17 an example of the simulation for the 4th stack in stand V, i.e. A4, B4, C4 and D4, with 5 MeV pulse-height threshold is shown. The z -axis gives the neutron detection efficiency. On the y -axis the position with a bin width of 10 cm is plotted, while on the x -axis the neutron kinetic energy with a bin width of 1 MeV is plotted. The maximum neutron detection efficiency is reached in the middle of the bar, where the light signal is least affected by the light attenuation since the path to the two PMs is the same. The dependence of the neutron detection efficiency on the neutron kinetic energy is shown in Fig. 4.18 for a 5 MeV_{ee}, black square, and 7.5 MeV_{ee}, red triangle, threshold. For the 5 MeV_{ee} pulse-height threshold a maximum neutron detection efficiency of 16% is reached for neutron kinetic energies around 50 MeV. For more energetic neutrons the efficiency falls smoothly until reaches a constant value of 12%. The neutron detection efficiency for 7.5 MeV_{ee} pulse-height threshold is smaller overall; the maximum of 14% is for a neutron kinetic energy of around 60 MeV. After the maximum the efficiency falls to a constant value of 11%.

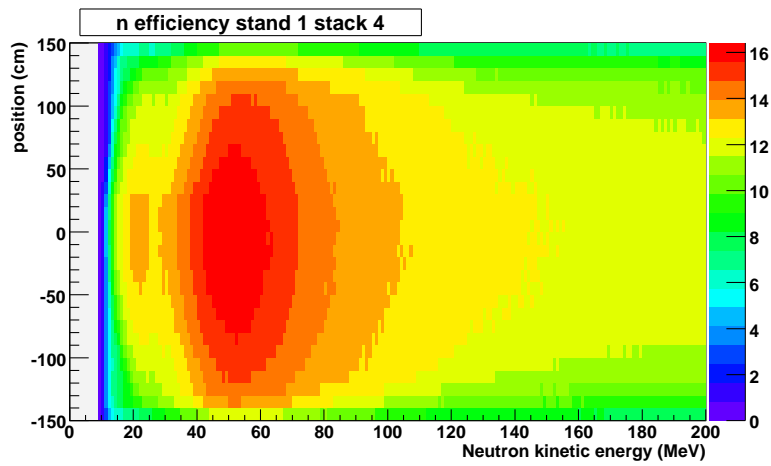


Figure 4.17: Neutron detection efficiency (z-axis) in dependence of incident position and kinetic energy. The software threshold was at 5 MeV_{ee} .

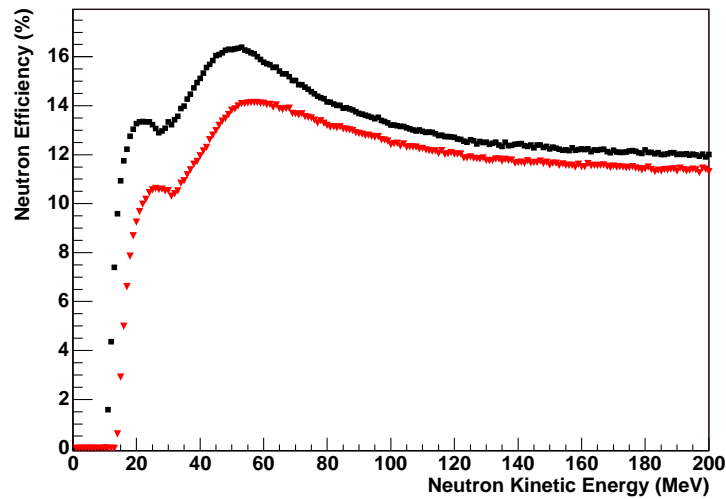


Figure 4.18: Neutron efficiency for one stack as a function of the neutron kinetic energy for two different pulse-height thresholds. The black square are for 5 MeV_{ee} threshold and the red triangle are for 7.5 MeV_{ee}

Chapter 5

Data Analysis

5.1 Particle four-vectors

Once the detectors have been calibrated the four-vector of each particle involved in the reaction can be determined. The four-vector contains the total energy and the momentum of the particle, where the vector is defined by the three Cartesian components in the laboratory system. The Cartesian components are a transformation from the polar coordinates since the azimuthal and polar angles are the variables measured in the detectors.

5.1.1 Photon

The photon is emitted in the forward direction from the radiator, the z -axis in the laboratory system. Since the photon is massless the energy and the absolute value of the momentum are equal and the direction of the momentum vector is in the direction of propagation. The four-vector for the photon is then

$$(E_{tot}, p_x, p_y, p_z) = (E_\gamma, 0, 0, E_\gamma) \quad (5.1)$$

Moreover for each photon there is an associated time, the t_{tag} from eq. 4.3, that distinguishes a prompt photon from a random one. In section 5.2 a detailed description concerning the treatment of prompt and random photons is given.

5.1.2 Proton

Polar and azimuthal angles

The incident angle of the proton on the x - z plane is determined using the two horizontal DSSDs and is found using the difference in hit pixel position between the two horizontal DSSDs. This can be seen in Fig. 5.1 which shows a schematic top view of the DSSDs. The particle from the target will hit the pixel x_1 then x_2 before impinging the Germanium hodoscope. If the separation between the two DSSDs is d the in-plane angle in the x - z -plane is calculated as:

$$\theta_{xz} = \text{atan}\left(\frac{p(x_2 - x_1)}{d}\right) \quad (5.2)$$

where the pixel difference is multiplied by the pitch $p = 1$ mm.

The θ_{xz} is the in-plane angle in the internal reference system of the Germanium hodoscope. The in-plane angle in the lab system is defined as the sum of θ_{xz} and θ_{Ge} , that is the angle at which the Germanium hodoscope is fixed on the experimental table:

$$\theta_p = \theta_{xz} + \theta_{Ge} \quad (5.3)$$

In Fig. 5.2 a sketch of the system in the hall is depicted. Fig. 5.2. The in-plane angle θ_p defines the incident direction of the proton hence the Cartesian coordinate of the hit in the laboratory system:

$$\begin{aligned} x &= l \cdot \sin(\theta_p) \\ y &= \Delta y \\ z &= l \cdot \cos(\theta_p) \end{aligned} \quad (5.4)$$

where l is the trajectory vector in the x - z plane and $\Delta y = p (y_2 - y_1)$ is the difference between the pixels of the two vertical strips with $p = 2$ mm. The polar angle and the azimuthal angle of the particle are extracted in the usual way:

$$\begin{aligned} \theta &= \text{atan}\left(\frac{\sqrt{(x^2 + y^2)}}{z}\right) \\ \phi &= \text{atan}\left(\frac{y}{x}\right) \end{aligned} \quad (5.5)$$

The solid angle of the proton is calculated via the simple formula r^2/D^2 where r is the radius of the first crystal in the Germanium hodoscope and D is the distance from the target to the Germanium hodoscope, as depicted in Fig. 5.2.

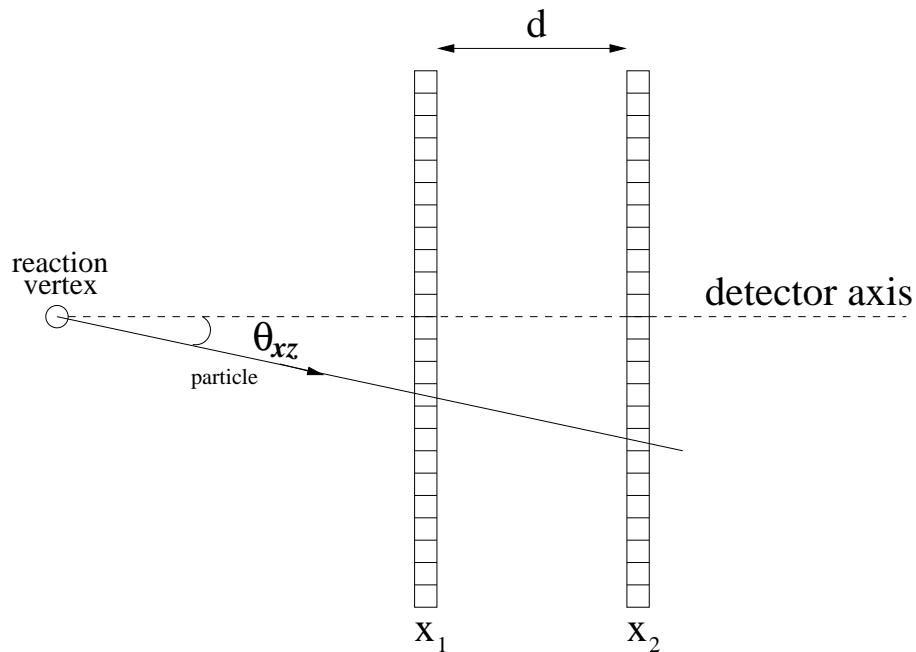


Figure 5.1: Schematic of a particle traversing the 2 horizontal DSSD.

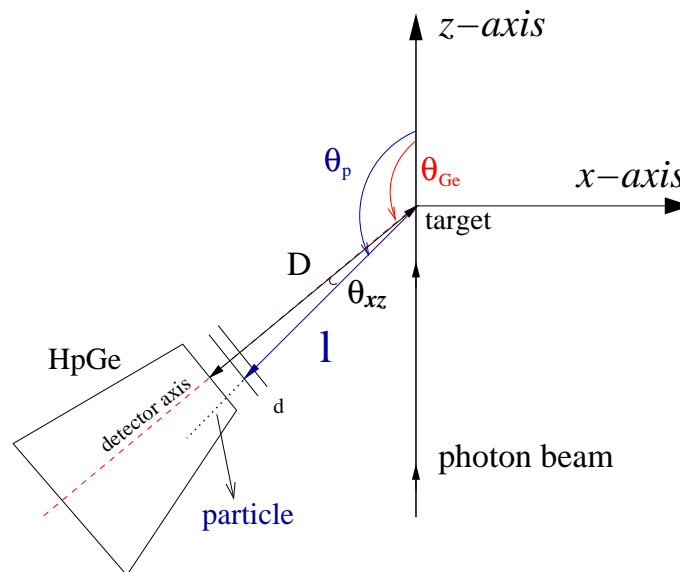


Figure 5.2: Sketch of one Germanium hodoscope and the DSSDs with the angles in the laboratory system.

Kinetic energy at the vertex

The kinetic energy of the particle at the vertex of the reaction has to be reconstructed since the energy measured in the Germanium hodoscope is the energy loss of the

particle in the Germanium material. Starting from this energy and assuming the particle stops in the Germanium hodoscope the energy loss in the individual layers from the target to the Germanium hodoscope can be reconstructed from range tables since the dimensions of the material are known. The kinetic energy of the particle at the vertex is the sum of the energy deposited in the Germanium and in the dead layers before. The dead layers considered are the target, the two DSSD and the beryllium window of the Germanium hodoscope. The layer of air between the target and the DSSD is not considered because the flight path is around 9 cm and for this the energy loss for a proton of 50 MeV is 0.11 MeV. For higher energy protons the energy loss in the air is a factor 10 smaller. The relative error goes from 0.3% for the low energetic protons up to 0.01% for 250 MeV protons. The target has an inclination angle θ_t with respect to the photon beam line so that an angular correction for the effective thickness of the material is required. In Fig. 5.3 a drawing of the target and the angles involved is shown; the triangles ABC and ADE are the two of interest. The particle traverses the path AE, the hypotenuse of the triangle ADE. If t is the effective thickness of the target, from trigonometry it follows that:

$$AE = \frac{t}{2} \frac{1}{\cos(\widehat{EAD})} \quad (5.6)$$

where the angle $\widehat{EAD} = \frac{\pi}{2} - \widehat{CAB}$. Considering the triangle ABC one finds that $\widehat{CAB} = \pi - \widehat{ACB} - \theta_{xz}$, where it is easy to see that $\widehat{ACB} = \theta_{Ge} - \theta_t$. With the known angles we can deduce the angle $\widehat{EAD} = \theta_{Ge} - \theta_t + \theta_{xz} - \frac{\pi}{2}$ and inserting this into equation 5.6 one can find the following correction factor for the effective thickness of the target:

$$AE = \frac{t}{2} \frac{1}{\sin(\theta_{Ge} - \theta_t + \theta_{xz})} \quad (5.7)$$

An angular correction is also required for the thickness of the DSSD and the cap of the Germanium hodoscope. The correction used is:

$$corr_{thick} = \frac{1}{\cos\alpha} \quad (5.8)$$

where α is the incident angle of the particle. Here $a = (x_2 - x_1)p$ is the horizontal pixel difference and $b = (y_2 - y_1)p$ the vertical pixel difference in mm. If the hypotenuse of the triangle with a and b as catheti is called c , i.e. $c^2 = a^2 + b^2$ the incident angle α can be written

$$\alpha = \text{atan}(c/d)$$

where d is the distance between the two DSSD as in Fig. 5.1.

The momentum of the particle is calculated relativistically from the kinetic energy T and the mass m :

$$p = \sqrt{(T^2 + 2Tm)} \quad (5.9)$$

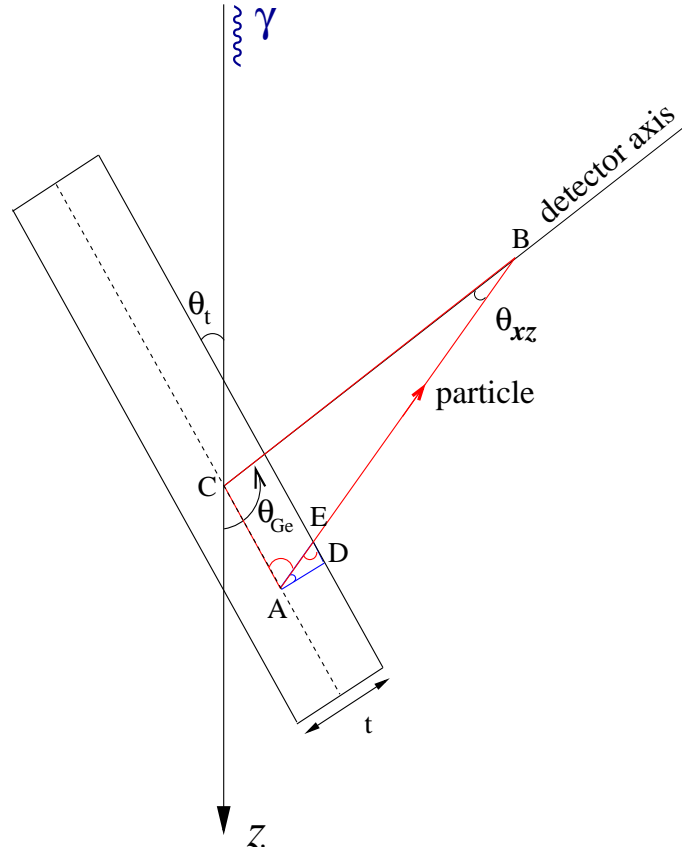


Figure 5.3: Schematic drawing of the target angular correction.

5.1.3 Neutron

The kinetic energy of the neutron is calculated with the relativistic formula 4.7 where the velocity of the neutron is the ratio of f_p to t_f . t_f is calculated via formula 4.11. In ACQU f_p and the polar and azimuthal angles are reconstructed on an event by event basis from the coordinates of the hit in the bar, eq. 4.15. The polar angle is then:

$$\theta_n = \text{acos}(f_{pz}/f_p) \quad (5.10)$$

and the azimuthal angle is:

$$\phi_n = \text{atan}(\text{hit}_z/f_p). \quad (5.11)$$

These angles give the direction of the momentum of the neutron, calculated as in eq. 4.8.

5.2 Background subtraction

As explained in section 4.2 there are several electrons registered in the focal plane detector but only one which produced the photon, or possibly even none. In the analysis it is possible to reject events which do not fall in a specific time region. For the present analysis the tagger time spectrum is divided into one prompt region, which also contains some randoms below the peak, and a wider region containing only randoms. In Fig. 5.4 the spectrum of the t_{tag} from eq. 4.3 with the prompt and random region chosen for this analysis is shown. The random region on the right hand side was chosen because on the left hand side a small bump is present which is caused by pions detected in the Germanium hodoscope. Since the two regions have different widths the weight associated with the photon energy is:

$$\text{Weight}_\gamma = \begin{cases} +1 & \text{if prompt} \\ -\frac{\Delta t_P}{\Delta t_R} & \text{if random} \end{cases} \quad (5.12)$$

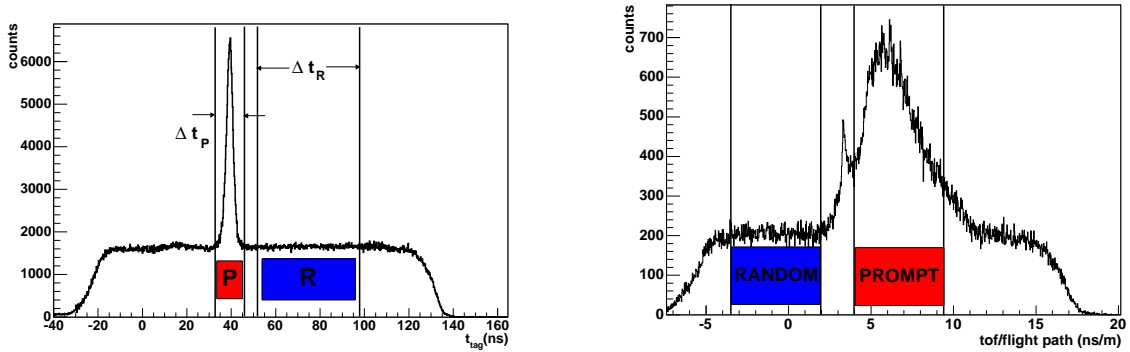


Figure 5.4: Left Panel: Spectrum of the time of the tagger in coincidence with the time of the Germanium hodoscope. The chosen prompt and random regions are shown. Right Panel: Time of flight divided by the flight of path for all the scintillator bars.

The time spectrum of the neutron shows a prompt peak for neutrons detected in TOFs in coincidence with the start detector, i.e. neutrons that come from the vertex of the reaction. The neutrons that do not have any time correlation with the start detector contribute to the background under and beside the coincidence peak. The background neutrons are a product other reactions in the target but have the time in the right window or are neutrons emitted before the start time and have been reflected back from the ceiling and walls of the hall to the TOF detectors. In figure 5.4 (right panel) the time of flight normalised to the flight path for all the scintillator bars shows the two regions of equal width. The prompt region is chosen in order to accept almost all neutrons in the peak and to avoid the relativistic peak that can

bring unwanted randoms, the thin sharp peak to the right of the neutron peak. The random region was chosen on the left side of the neutron peak before the relativistic peak because there the random plateau is longer than on the right hand side. In the analysis the regions are chosen from the t_m spectra on a frame-by-frame basis.

Each neutron falling in one of the regions was given a $\text{weight}_{\text{TOF}}$ which is +1 if it is in the time prompt region or -1 if it is in the random region. Because of the high multiplicity gained from the tagger when using the new neutron time variable 5.19 there was more than one neutron time per event, hence the final weight associated with each neutron had to be divided by the number of photons in the tagger for that event:

$$\text{Weight}_n = \begin{cases} \text{weight}_{\text{TOF}}/n_{\text{prompt}} & \text{if photon prompt} \\ \text{weight}_{\text{TOF}}/n_{\text{random}} & \text{if photon random} \end{cases} \quad (5.13)$$

where n_{prompt} is the number of prompt photons and n_{random} the number of random photons.

The weighting for photons and neutrons are calculated together and they are associated with the four-vector of an observable like the missing energy for each event. In Fig. 5.5 the two plots of Fig. 5.4 are combined to a 2D plot of neutron time versus tagger time. The region in the red rectangle is the region containing triple coincidence events between prompt photons, prompt protons and prompt neutrons. Following the vertical line of the prompts in the tagger we find the region marked in green where prompt events from tagger and Germanium detectors are in coincidence with a random in TOF. The region in the yellow rectangle is another double coincidence region with a prompt neutron, a prompt proton but a random photon. The region marked in black contains a random photon, a random neutron and a random proton. The corresponding region to the black one on the right side of the neutron prompts region contains randoms photons and neutrons but prompt protons. This region was not considered because the contribution to the cross section is equal to the one in the black region. The triple coincidence and the purely random region are given a positive weight while the double coincidence events are given a negative weight due to negative weight of the random events either in the tagger or in TOFs. The weights were calculated for each event and were associated to the desired observable.

5.3 Calculation of the cross section

After the four-vectors of every particle involved in the reaction are determined the observables, like the missing energy, are built per event. The value in histogram is the sum of all events and the characteristics of the target and the detectors are taken

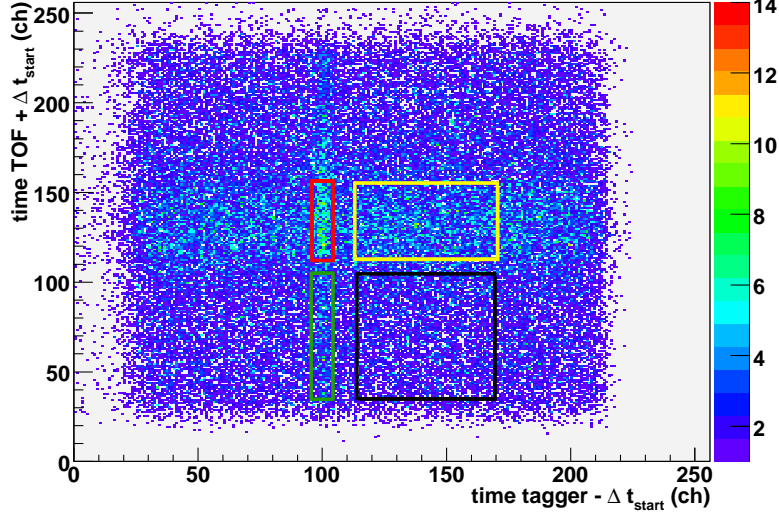


Figure 5.5: Two dimensional spectrum for the time of TOF against the time of tagger in coincidence with the start time. The red region is the true triple coincidence. The green and the yellow regions are double coincidence and the black one is the purely random region.

into account so that the yield of an observable is written:

$$Y = \frac{1}{n_t} \sum_i \left[\frac{1}{\epsilon_n(i) \sum_s(E_\gamma) \epsilon_t(i)} \right] \cdot \text{Weight}_\gamma(i) \cdot \text{Weight}_n(i) \quad (5.14)$$

where the index i represents one single event. The n_t represents the number of target atoms per cm^2 , ϵ_n is the neutron detection efficiency (see section 4.5.5), $\sum_s(E_\gamma)$ is the sum of the tagger free scalers, which gives the photon flux, and ϵ_t is the tagger efficiency (see section 3.2.1). The yield is multiplied by photon weight and the neutron weight for each event. The differential cross section as a function of a given observable X in $\mu\text{b}/\text{sr}^2[X]$ is then:

$$\frac{d^5\sigma}{d\Omega_p d\Omega_n dX} = \frac{Y \cdot 10^{30}}{\Delta\Omega_p \Delta\Omega_n \Delta X} \quad (5.15)$$

where $\Delta\Omega_p$ and $\Delta\Omega_n$ are the solid angles covered by the proton and neutron detectors at the reaction vertex. The ΔX gives the bin width of the cross section histogram. The observables, X , accessible in this experiment are the missing energy with $[X]$ being MeV and the missing momentum where $[X]$ is MeV/ c .

5.3.1 Experimental uncertainties

The overall experimental uncertainties of the measurement have contributions from both statistical and systematic origins. The systematic uncertainties arise from the calibration of the detectors and from the design of the experiment while the statistical uncertainty depends to the number of real and randoms events. The weighting and the correction factors, the efficiencies, contribute to the statistical error which is given by the formula 5.16 for each bin:

$$\Delta Y_s = \sqrt{\sum_i \left(\frac{\text{Weight}_\gamma(i)}{\epsilon_t(i)} \cdot \frac{\text{Weight}_n(i)}{\epsilon_n(i)} \right)^2} \quad (5.16)$$

the weight of the proton was taken to be +1 because the probability to detect it is assumed to be 100%, as explained in section 4.4.5.

Systematic uncertainties arise from:

- the determination of the target thickness, which is well defined from the geometrical construction. The uncertainty is mainly due to the evaporation of the water during the experiment. Considering that the target was refilled at constant time intervals and the formation of the bubble was almost above the beam spot we estimated the uncertainty to be well below 1% and can therefore be neglected.
- the reconstruction of the proton energy at the vertex. The correction factors for the inclination of the target with respect to the beam line and for the entrance proton angle give an uncertainty well below 1% and can therefore be neglected. Other systematic uncertainties come from neglecting of the energy loss in air. From range tables one can calculate that for the low energetic protons (around 50 MeV) the neglecting of the energy loss in air gives a 0.2% uncertainty and for the most energetic protons (250 MeV) the uncertainty is even smaller being 0.03%. This uncertainty can also be neglected.
- neutron detection efficiency. Comparison of the results of the STANTON code with real data have been made by Cecil [70] and shows an agreement within 10% over a wide neutron kinetic energies. No other sources of uncertainty in the determination of the neutron detection efficiency are of relevance.

5.4 Photo-disintegration of ^2H

Once the four-vector of each particle is known the missing energy can be determined on an event-by-event basis. For a two nucleon knock-out the missing energy of eq. 1.2

is written:

$$E_m = E_\gamma - T_n - T_p - T_{\text{rec}} = Q + E_x \quad (5.17)$$

Of particular interest is the missing energy for the total disintegration of the deuteron since the reaction is kinematically over-determined. The break-up of the two-body system is used to check the calibrations and to determine the energy resolution of the triple coincidence reaction. In a deuterium break-up reaction there is no recoil nucleus therefore the eq. 5.17 can be written $E_m = E_\gamma - T_n - T_p = Q = 2.2$ MeV, where the Q-value of the reaction is the binding energy of the deuteron.

Using kinematic calculations, i.e. energy and momentum conservation in a relativistic frame, it is possible to determine the four-vector of the neutron from the energy of the photon and the polar and azimuthal angles of the proton in the laboratory system. For our setup the most probable deuteron kinematics, where the neutron and the proton are emitted back to back in the c.m. system, corresponds to protons detected at $\theta_p = 150$ degrees and neutrons with θ_n from 13 to 25 degrees in the laboratory system. The detectors positioned at these angles are Panoramix for the proton and stand IV (EFGH) for the neutron; all the spectra shown in this section contain coincidence event from only these detectors.

The missing energy reproduced in Fig. 5.6 is calculated from the equation:

$$E_m = E_\gamma - T_n^{\text{cal}} - T_p. \quad (5.18)$$

with E_γ from the tagger, the proton kinetic energy from Panoramix and the neutron kinetic energy from kinematic calculations. Random subtraction is done by considering only the tagger time information. Due to this random subtraction one expects a zero contribution at negative missing energy while the structure present to the right of the peak is due to reactions in Oxygen nuclei. We observe a peak at 1.7 MeV with FWHM 1.9 MeV. The theoretical position of the peak is well within the errors indicating that the tagger and the Germanium hodoscope are well calibrated. The FWHM represents the energy resolution of the tagger in coincidence with the Germanium hodoscope. Since the energy resolution of the tagger is around 2 MeV, the energy resolution of the Germanium hodoscope is in the order of few keV, which is in agreement with the 366 keV found in the test of one of the Germanium hodoscope at PSI, see section 4.4.4. The FWHM of the deuteron missing energy peak with the neutron kinetic energy measured in the TOF gives the triple coincidence energy resolution, which is expected to increase from the 1.9 MeV because extra uncertainties come from the third detector.

Fig. 5.7 shows the missing energy using the neutron kinetic energy measured in the TOF. The photon energy is in the range 120 to 270 MeV. The proton must have a kinetic energy between 50 and 68 MeV. A cut on the neutron momentum has also been made; only the events where the measured neutron momentum is equal to the expected momentum as calculated from the deuteron break-up kinematics are included in the histogram. Despite of the applied cuts multiple structures are

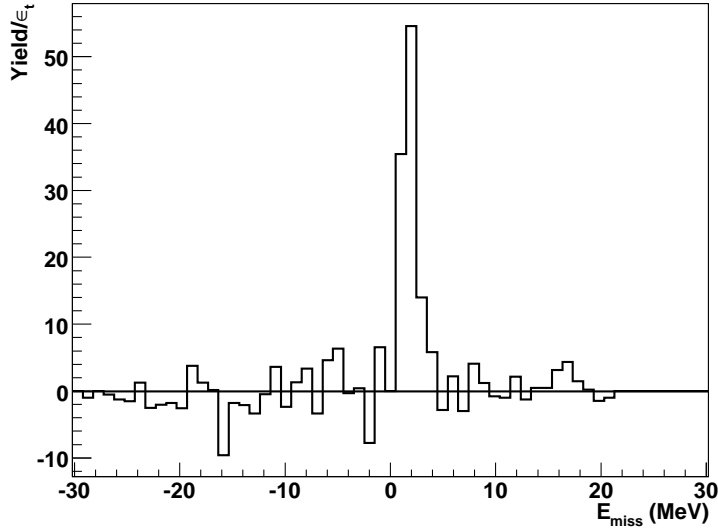


Figure 5.6: Missing Energy for the photo-disintegration of ^2H calculated from tagger and Germanium hodoscope only.

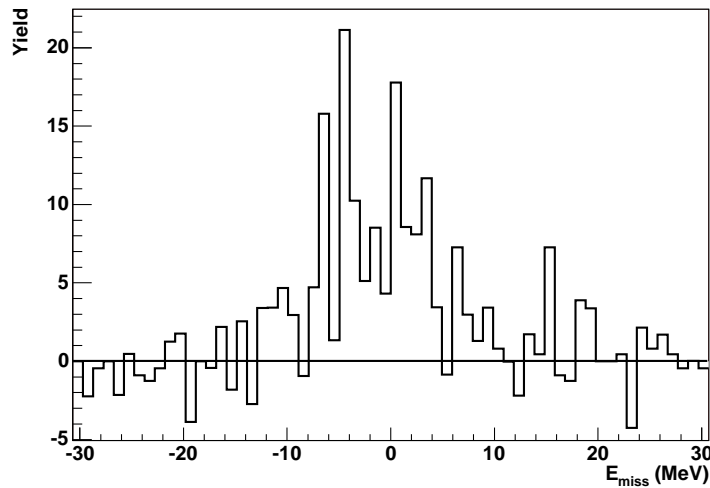


Figure 5.7: Missing Energy for the $^2\text{D}(\gamma, \text{pn})$ reaction. All the kinetic energies are measured in the respective detectors.

present in the histogram. The FWHM of the Gaussian fit to the peak is 11 MeV, the poorer resolution being caused by the poor time resolution of the start signal from the Germanium hodoscopes. As explained in section 4.1 the Germanium detectors showed an energy and position dependence which give a poor start time signal for

the reaction. In order to avoid this problem one can eliminate the dependence on the Germanium time signal in the offline analysis. The most reasonable solution we could think about was to couple the time of the TOF with the time of the tagger. Since the tagger was stopped by the Germanium hodoscope and the TOF started by this (see section 3.6) by adding the time of the TOFs, as in eq. 4.11, with the tagger time as expressed in eq. 4.3 the dependence on the Δt_{start} is eliminated. In Fig. 5.8 a sketch of the tagger time and TOF time with respect to the start time ($t=0$) and to the reaction vertex is shown. The t_m is the mean time of the two PMs; the time of flight t_f from the reaction vertex is obtained by adding the Δt_{start} . Differently the tagger time to the reaction vertex t_{tag} is obtained by subtracting the Δt_{start} from the TDC value. The green line represents the new time variable for the TOFs which is defined:

$$t_f^{tag} = t_f + t_{tag}. \quad (5.19)$$

The momentum and the kinetic energy of the neutron can be calculated from the time of flight in eq. 5.19 with the flight path being always the same. The improvement in the energy resolution of the triple coincidence is evident as can be seen in Fig. 5.9 where the missing energy calculated with photon energy from tagger, proton from Germanium and neutron from TOFs is shown. The windows for photon and proton energy are the same as in Fig. 5.6 and the same random subtraction method is used. There is no splitting of the peak and the energy resolution could still be improved using a better background subtraction. The result of this is shown and discussed in section 6.1.

Because of this shift in the start time two new time offsets are needed. One is the usual t_0 explained in section 4.5.2; the values found previously are no longer valid therefore new t_0 values were extracted using the procedure described in section 4.5.2 again. The other time offset is necessary to shift the t_f^{tag} created from random tagger

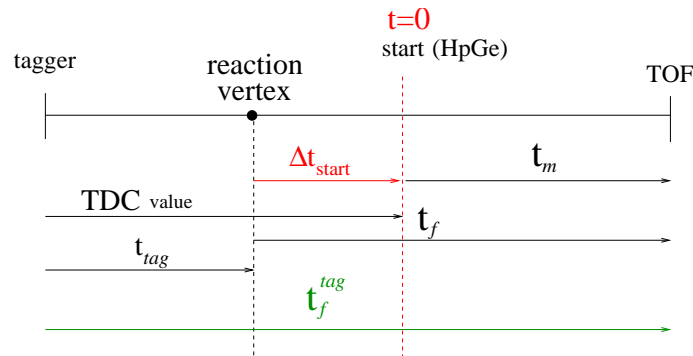


Figure 5.8: sketch of the time correlation between tagger, Germanium and TOF. The new TOF time is the sum of the tagger time and the old TOF time.

times to the values from prompt tagger times. The need for a second offset is clear when one looks at the distribution of the t_f^{tag} times from random tagger times,

they differ by a constant offset when compared to the results where prompt tagger times are used. Moreover t_0 values are extracted by using the latter time of flight distribution. The second time offset used is the separation between the lower limit of the prompt region and the lower limit of the random region. In Fig. 5.10 we see a schematic drawing of the tagger time with the prompt and random regions. If the neutron time is built from a channel in the random region it will be shifted to the prompt region. Another consequence of the creation of the observable t_f^{tag} is that it gains the multiplicity of the tagger since for one event there are several electrons detected at the focal plane. When doing background subtraction particular attention

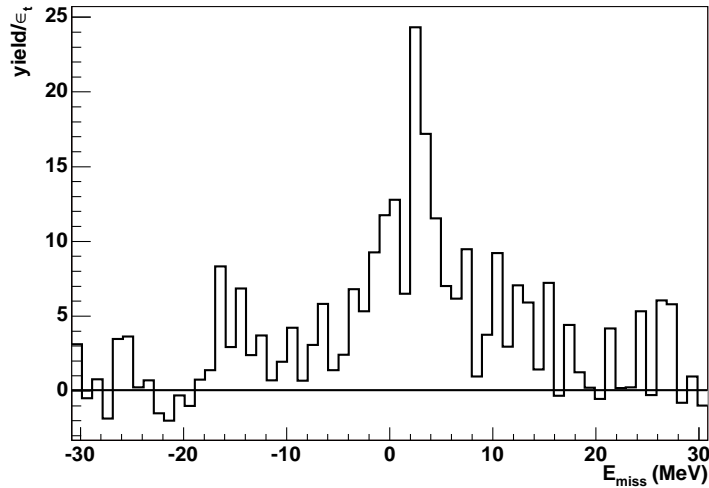


Figure 5.9: Missing Energy for the $^2\text{D}(\gamma,\text{pn})$ reaction. All the kinetic energies are measured in the respective detectors, the time of the TOF is calculated as in the formula 5.19.

has to be given to the acquired multiplicity of the neutron time of flight. As already seen in section 5.2 the weighting for the neutron is normalised by the number of photons in the tagger, eq. 5.13.

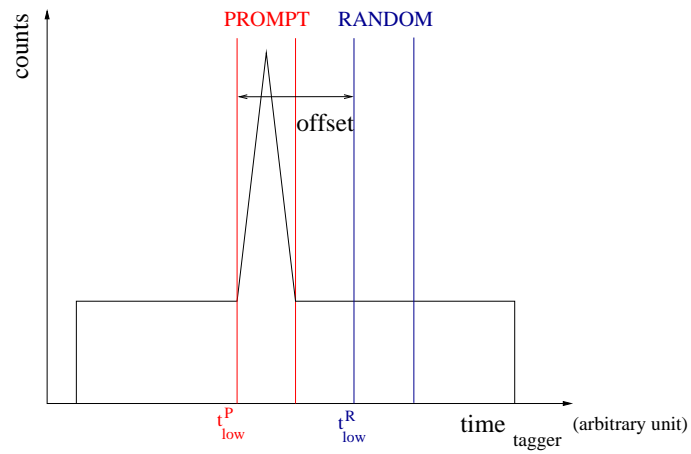


Figure 5.10: Sketch of the tagger time in coincidence with the start time. The prompt region and one random region are marked by delimiters. The neutron times determined in the random tagger time must be shifted to the prompt time using the offset.

Chapter 6

Results and discussion

In this chapter the results of the (γ, pn) and ${}^6\text{Li}(\gamma, \pi^+){}^6\text{He}$ reactions are presented.

6.1 ${}^2\text{H}(\gamma, pn)$ reaction

In Fig. 6.1 the cross section as a function of the missing energy for the disintegration of the deuteron is shown for back-to-back kinematics. The protons were detected in Panoramix and the neutrons in stand IV. The data used are those taken with the heavy water target. The gamma energy used was in the microscope region, which is between 150 and 250 MeV. The proton kinetic energy was chosen to be in the range 50 to 80 MeV which means only protons which stop in the first germanium crystal. This energy range is the expected energy range of the protons determined using kinematical calculations of deuterium break-up and avoids the use of the second and third germanium crystals where a dead layer is present. The neutron polar angle used was between 13 and 25 degrees in order to restrict the analysis to back-to-back kinematics. The neutron software pulse-height threshold was set to 5 MeVee. A complete background subtraction, as described in 5.2, has been done and the error bars shown are only statistical. In the unphysical region the average of the cross-section is zero showing the validity of the method used. To the right of the deuteron peak some structures appear from reactions on Oxygen nuclei which are not completely suppressed by the kinematical conditions. A Gaussian fit to the deuteron peak gives a mean peak position of 2.05 MeV with a FWHM of 8 MeV. The FWHM represents then the missing energy resolution for this data set. Of the 8 MeV 2 come from the double coincidence of tagger with germanium hodoscope as stated in section 5.4. The remaining 6 MeV are due to the time coincidence of the TOFs with the tagger since the dependence on the germanium hodoscope signal was eliminated with the procedure described in section 5.4. The change of the time coincidence from TOF and germanium to TOF and tagger improved the energy resolution by 3 MeV

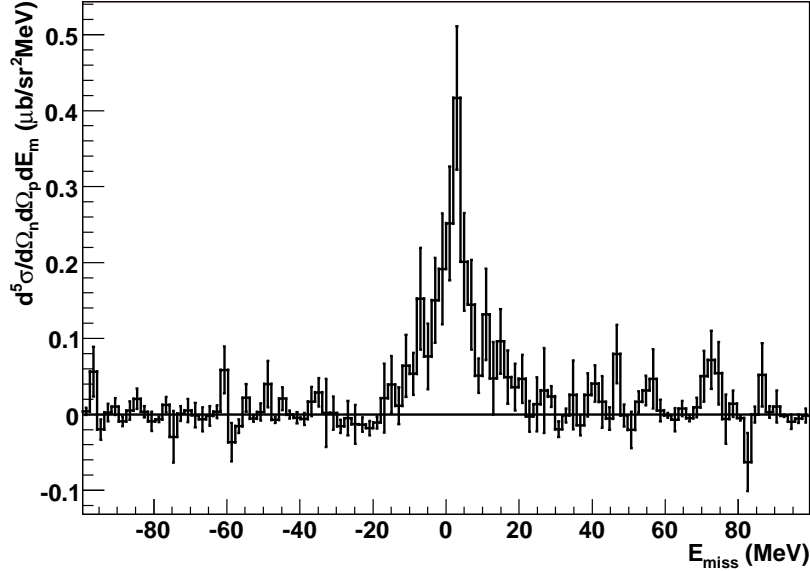


Figure 6.1: Cross section as function of the missing energy for the photodisintegration of the deuteron

compared to the peak shown in Fig. 5.7 which has a FWHM of 11 MeV.

In Fig. 6.2 the momentum distribution for the photodisintegration of the deuteron is shown. The half Gaussian around zero is the typical signature of the deuteron missing momentum distribution, which ideally would be a delta function centred at 0 MeV/c since there is no recoil nucleus. The sigma of the Gaussian gives the momentum resolution of the experiment and depends on the energy and angular resolutions of the detectors. The variance of the Gaussian fitted to the missing momentum is 26 MeV/c.

6.2 $^{16}\text{O}(\gamma, pn) ^{14}\text{N}$ reaction

In this section the results of photon induced proton-neutron knock-out reactions in the ^{16}O nucleus are discussed. The photon was detected in the tagger, the proton in the Germanium hodoscope Panoramix at 150° with respect to the beam line and the neutron in the TOFs which cover an angle from 8° to 32° in the forward direction. The kinematics were wider than the back-to-back kinematics investigated for the photo-disintegration of the deuteron though the majority of the neutrons were detected in the back-to-back kinematics.

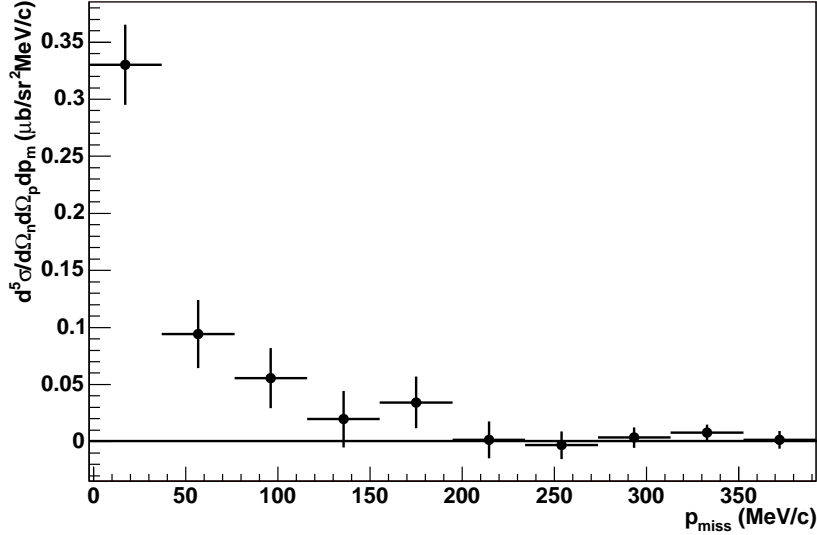


Figure 6.2: Missing momentum distribution for the photodisintegration of the deuteron cross section.

6.2.1 Missing energy distribution

In Fig. 6.4, 6.5 and 6.6 cross sections as function of the missing energy for different photon energy ranges are shown; 150 to 250 MeV, 180 to 250 MeV and 200 to 250 MeV for Figs 6.4, 6.5 and 6.6 respectively. The ground and the first three excited states of residual ^{14}N nucleus are marked with arrows.

For each histogram the neutron pulse-height threshold was 5 MeVee. The missing energy cross sections were also calculated using a high threshold, 7.5 MeVee, but these had poorer statistics so the 5 MeVee threshold was used. For each histogram a signal from the strip detectors was required in order to decrease the number of detected charged particles which did not originate at the vertex of the reaction. The information from the incident angle of a given particle was used to reconstruct the polar and azimuthal angles as described in section 5.1.2. No upper limit in the proton kinetic energy was set because a wider range is now expected from this reaction. The lower limit of 18 MeV was given by the trigger threshold. The background subtraction was done as described in section 5.2. In Fig. 6.3 the missing energy distribution has a longer negative x -axis showing the unphysical region. A flat fit to this region, red line, shows an average value of $0.0003 \mu\text{b sr}^2 \text{MeV}$, which represents a 0.1% of the maximum cross section value. This means that the background subtraction procedure used is correct and that the structures with E_m greater than that of the deuteron peak are due to real triple coincidences.

Figs 6.4, 6.5 and 6.6 show a wide peak around 0 from deuteron events. It is

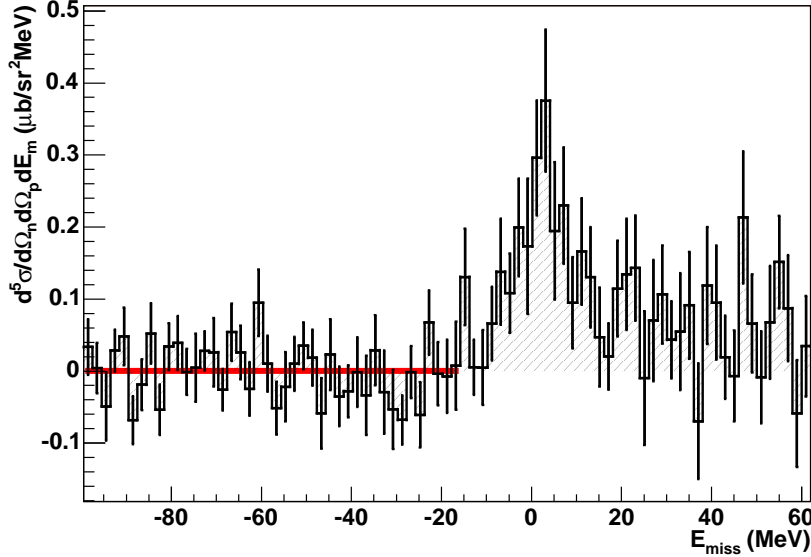


Figure 6.3: Missing energy distribution for $^{16}\text{O}(\gamma,\text{pn})\ ^{14}\text{N}$ reaction with protons in Panoramix and neutrons in TOFs. $150 < E_\gamma < 250$ MeV. The red line is a fit to the flat background.

wider than in Fig. 6.1 because Oxygen kinematics are employed, i.e. the recoil momentum of the residual nucleus is subtracted to determine the missing energy. The final states in the ^{14}N could not be resolved because the energy resolution of 2 MeV required for this was not achieved, groups of final states are visible though.

The arrows in Fig. 6.4 indicate the position of some final states in ^{14}N . Since the Q -value for the $^{16}\text{O}(\gamma,\text{pn})\ ^{14}\text{N}$ reaction is 22.9 MeV the first peak in Fig. 6.4 can be associated with the ground state. In the dip behind this peak would be the first excited state, 2.31 MeV (0^+). There is no visible population of this state in the figure. This result is similar to previous measurements where it was found to have 5% of the strength of the ground state [17] or not populated [19]. Theoretical calculations in a shell model framework [39] reported in Tab. 1.1 predict the first excited state to have a cross section a factor 4 lower than the cross section for the ground state. The observation in this experiment that the first excited state is located in a dip of the missing energy distribution confirms these calculations and the previous experimental results. The second peak in Fig. 6.4 may be the overlapping of the second 3.95 MeV (1^+) and the third 7.03 MeV (2^+) excited states. The strength of this peak is half of the strength of the first peak. This observation is not in agreement with the theoretical calculations of Ryckebusch *et al.* [39]. In Tab. 1.1 we see that the sum of the cross sections for the second and the third excited states gives a larger value than the cross section for the ground state. The missing energy distribution of the

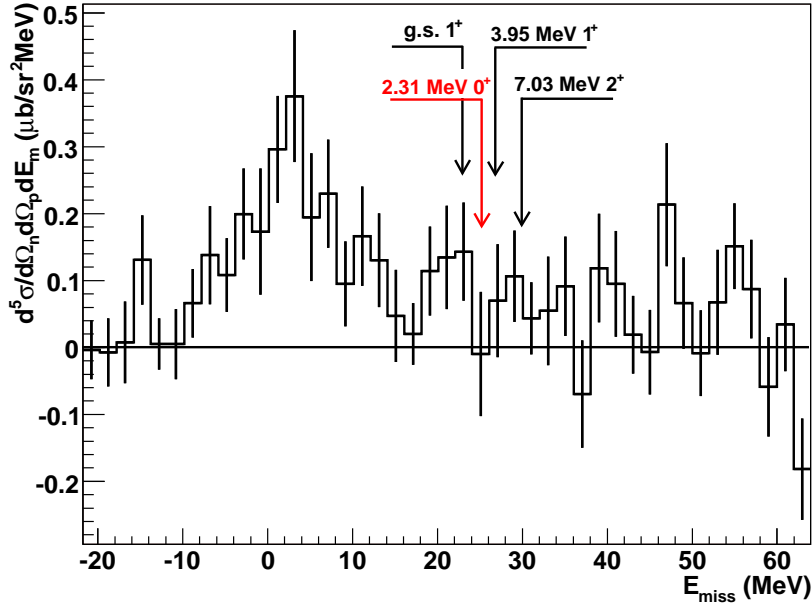


Figure 6.4: Missing energy distribution for $^{16}\text{O}(\gamma, pn)^{14}\text{N}$ reaction with protons in Panoramix and neutrons in TOFs. The photon energy is from 150 to 250 MeV.

previous experimental results from Ref. [17] shown in Fig. 1.7 showed comparable cross section strengths for the ground, second and third excited state.

In Fig. 6.5 the strength of the peak around the g.s. decreases compared to that in fig. 6.4, due to the higher photon energy used. This effect has been observed in previous $^{12}\text{C}(\gamma, pn)^{10}\text{B}$ experiments [73, 74] and in section 6.3 there is a discussion about this. The strength of the second peak is comparable to that of the same peak in Fig. 6.4 giving further weight to the statement that this is a real ^{14}N combination of final states. Another confirmation of this comes from the missing energy distribution for photon energies in the range 200 to 250 MeV shown in Fig. 6.6. Here the second peak is still present but with a smaller strength compared to Fig. 6.5. Again the cross section strength decreases with increasing photon energy.

For all the three missing energy distributions the peaks present after the 7.03 MeV state may be combination of higher excited states or from three nucleon knock-out reactions since the thresholds for the (γ, ppn) and (γ, pnn) reactions are 30.5 MeV and 33.5 MeV respectively.

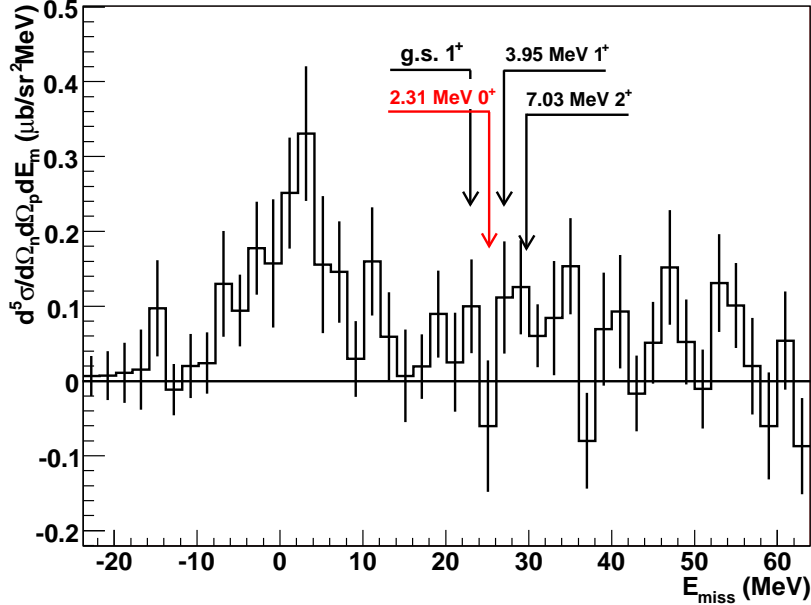


Figure 6.5: Missing energy distribution for $^{16}\text{O}(\gamma,\text{pn})^{14}\text{N}$ reaction with protons in Panoramix and neutrons in TOFs. The photon energy is from 180 to 250 MeV.

6.2.2 Missing momentum distribution

Even with the poor energy resolution and poor statistics it was still possible to produce a missing momentum distribution for a group of states in ^{14}N ; the second group of states of the ^{14}N residual nucleus were investigated. Fig. 6.7 shows the cross section as a function of the missing momentum for photon energies of 150 to 250 MeV and missing energies between 25 and 33 MeV. The cross section for low missing momenta increases from zero up to a maximum of about 150 MeV/c; the fourth point at 120 MeV causing a dip could be statistical. After this maximum the cross section decreases and at higher missing momentum it falls off to negative values. This behaviour is similar to previous results of the $^{12}\text{C}(\gamma,\text{pn})^{10}\text{B}$ reaction performed at MAMI in the photon energy range 200 to 400 MeV [73] and in the back-to-back kinematics [74]. A comparison to those experimental results is made in section 6.3.

6.3 Comparison with $^{12}\text{C}(\gamma,\text{pn})^{10}\text{B}$ reaction

As mentioned in section 6.2.1 it is worth comparing the results of this experiment with previous PiP-TOF experiments at MAMI where the $^{12}\text{C}(\gamma,\text{pn})^{10}\text{B}$ reaction

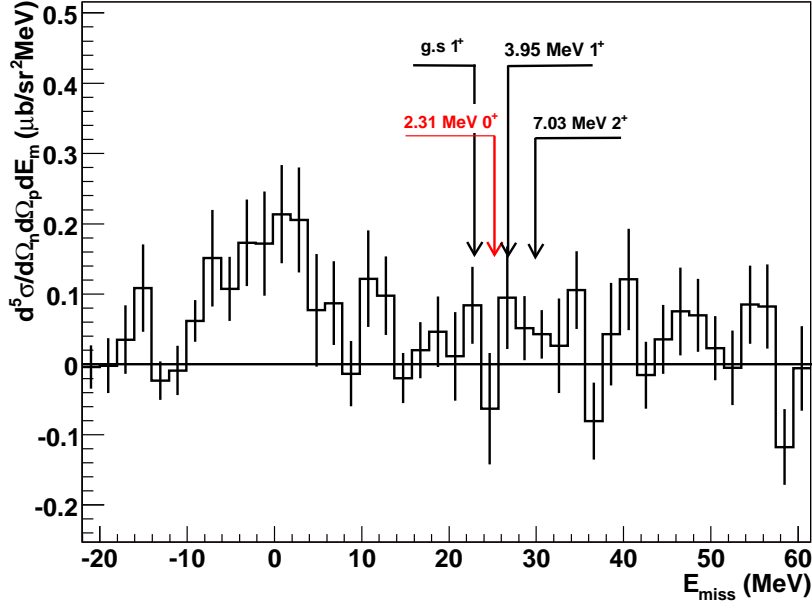


Figure 6.6: Missing energy distribution for $^{16}\text{O}(\gamma,\text{pn})^{14}\text{N}$ reaction with protons in Panoramix and neutrons in TOFs. The photon energy is from 200 to 250 MeV.

was investigated for several kinematics and photon energy ranges presented in [73] and [74]. In Fig. 6.8 left panel the visible cross section of Ref. [74] as function of the missing energy for different photon energy ranges is shown. The visible cross section is defined as the cross section which produces an event within the acceptance of the detectors. The kinematics used are the back-to-back kinematics as in the present experiment. The full circles are the data points and the various curves are different contributions to the cross-section from Valencia model (VM) calculations [75]. In the legend to the right of the picture the contributions are labelled: direct two-nucleon knock-out (2N), direct two-nucleon knock-out with final state interactions (2N+FSI), direct three-nucleon emission with or without FSI [3N+(FSI), initial π production with the π being reabsorbed in the nucleus (N π +ABS), initial π production with subsequent π rescattering in the nucleus (N π +EMIT) and initial NN π reactions. In Fig. 6.8 the missing energy distributions for $^{12}\text{C}(\gamma,\text{NN})$ reactions from Ref. [73] are presented, these were taken in a wide kinematics and are shown for different photon energy ranges.

In both pictures in Fig. 6.8 a strong peak is observable at low photon energy, in the figure on the left up to $E_\gamma=400$ MeV and in the figure on the right up to $E_\gamma=300$ MeV. This peak is interpreted to be the ground and low excited states of ^{10}B . The strength of this peak decreases as the photon energy increases. The same was observed in the present experiment when looking at Figs. 6.4, 6.5 and 6.6. Moreover the strength

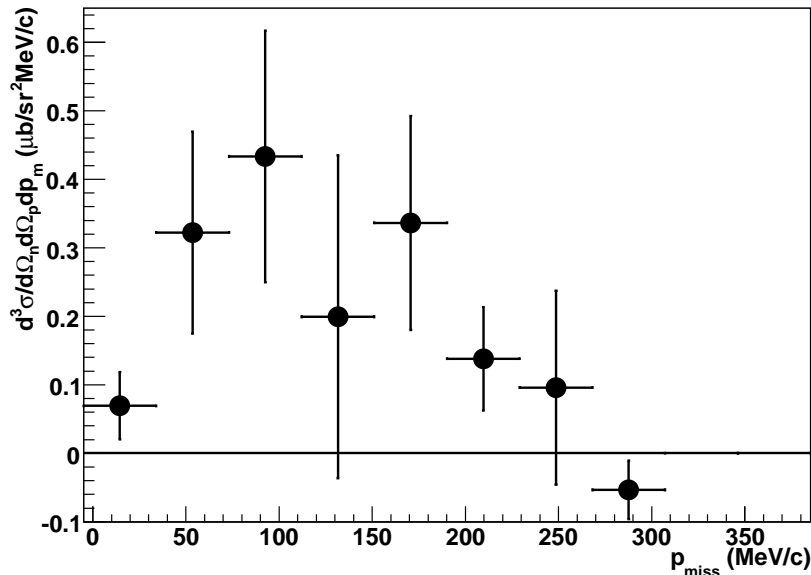


Figure 6.7: Momentum distribution for the missing energy from 25 to 33 MeV and photon energy from 150 to 250 MeV.

of the peak around the ground state in Fig. 6.4 is comparable to the strength of the peak in the left histogram of Fig. 6.8 for the lower photon energies. As the photon energy increases one can observe a shift of strength towards high missing energy. The comparison of the data with VM calculations, left panel of Fig. 6.8, showed that the strength arises from quasi free pion production followed by its reabsorption ($N\pi + \text{ABS}$), this was also reported in Ref. [73].

In Fig. 6.9 the cross section as function of the missing energy for photon energies of 150-200 MeV and 200-250 MeV for the present experiment with an E_m bin width comparable to Fig. 6.8 is shown. The deuteron peak is marked and the top of it cut off in order to concentrate only on the Oxygen events. The strength at low missing energies up to 80 MeV is comparable for the two photon energies. At high missing energy the cross-section becomes larger as observed in both pictures of Fig. 6.8.

In Fig. 6.10 the recoil momentum distributions in back-to-back kinematics for $E_m \leq 40$ MeV for photon energies of 150-200 MeV and 200-300 MeV from Ref. [74] are shown. The curves are simulations and calculations based on the VM. The solid line is a Monte Carlo simulation of direct two-nucleon knock-out and the dotted line is a phase space simulation of direct two-nucleon knock-out mechanism (2N-PS) where the energy in the final state is split between the two nucleons and the residual nucleus according to the available phase space. The other curves are predictions from the VM; the dot-dashed curve is the total cross section and the dashed line includes only direct two-nucleon knock-out. In Fig. 6.11 the recoil momentum distributions

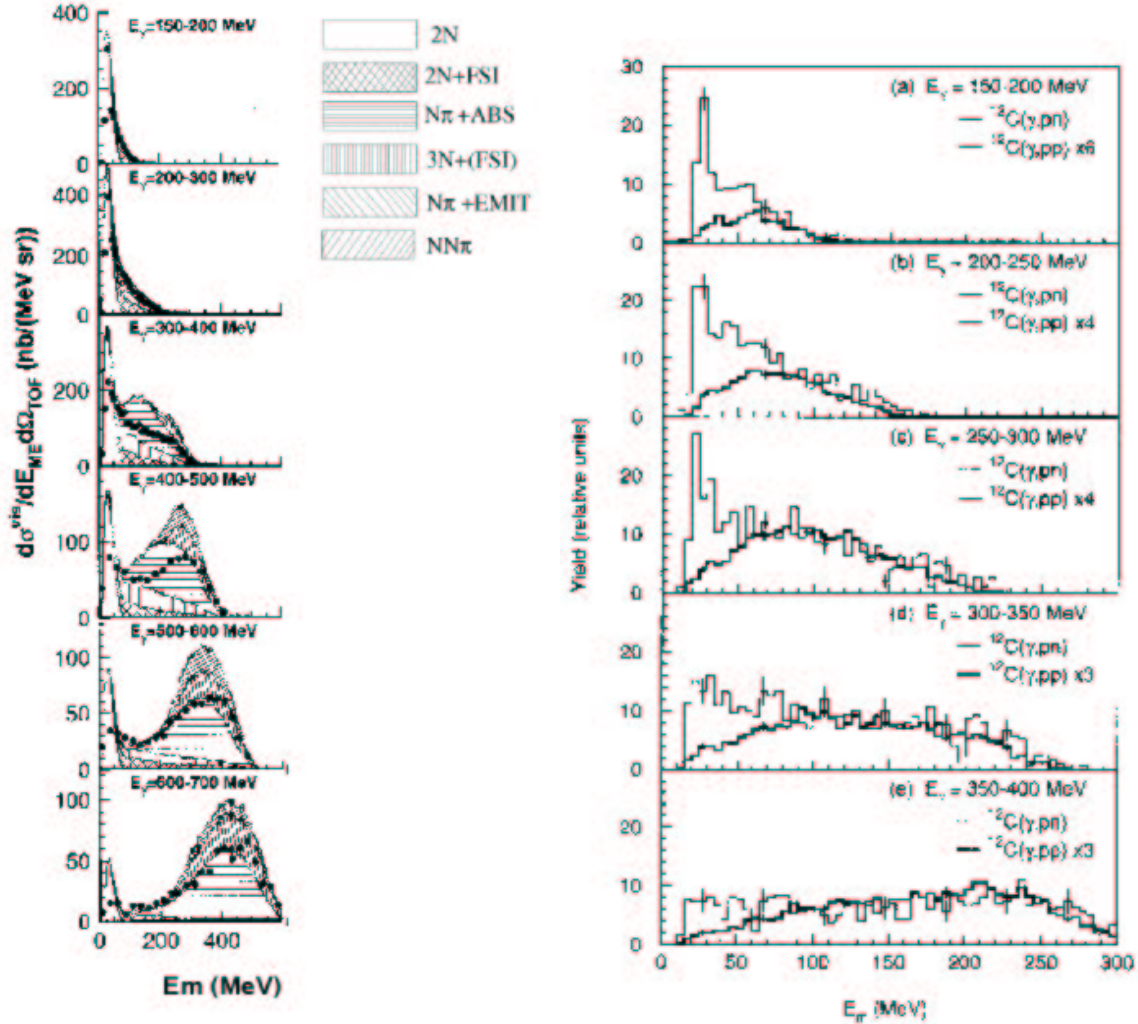


Figure 6.8: Left panel: Missing energy distributions for the $^{12}\text{C}(\gamma, \text{pn})^{10}\text{B}$ reaction at different photon energy ranges in a back-to-back kinematics [74]. Right panel: missing energy distributions for the $^{12}\text{C}(\gamma, \text{pn})^{10}\text{B}$ reaction at different photon energy ranges [73].

for wider kinematics for $E_\gamma = 200\text{--}400$ MeV and for $E_m < 40$ MeV from Ref. [73] are shown. The curves are based on the same Monte Carlo and phase space simulations as in Fig. 6.10, the solid line being the Monte Carlo for direct two-nucleon knockout, the dashed line the 2N-PS and the dot-dashed a phase space simulation of the emission of two nucleons and a pion. Since the shape of the missing momentum distribution depends on the cut in the missing energy one can compare the shape of the missing momentum distribution for the $^{16}\text{O}(\gamma, \text{pn})^{14}\text{N}$ reaction of Fig. 6.7 for $25 < E_m < 33$ MeV/c to Figs. 6.10 and 6.11. The shape is similar with a maximum at around 200 MeV/c with a decrease at high missing momenta though in Fig. 6.7

the decrease happens at lower p_m than for the $^{12}\text{C}(\gamma, pn)^{10}\text{B}$ reaction. This could be due to the lower missing energy range investigated. The maximum in Fig. 6.10 has a strength of 5 nb/MeV/c which is comparable to the strength of the maximum in Fig. 6.7 which is around 1 nb/MeV/c since the proton detector covers a solid angle of 60 msr and the three TOF stands in the forward direction cover 50 msr. Monte Carlo simulations of direct two-nucleon knock-out, solid line in Fig. 6.10 and Fig. 6.11, show very good agreement with the data points. The simulation is done assuming the pn pair is knocked-out from a 1p-shell. Due to the similarity in shape we could expect that the pn pair from the $^{16}\text{O}(\gamma, pn)^{14}\text{N}$ reaction leaving the ^{14}N nucleus in low excited states were also coupled in a 1p-shell. This is also expected from effective interaction calculations of the coefficients of fractional percentage (cfp) for two nucleons emitted from a 1p-shell made by Cohen and Kurath [18]. For the emission from ^{16}O the second excited state of ^{14}N has a cfp of 2.675 for $L=0$ transfer and the third excited state has 0.2753. Unfortunately the statistics of the present measurement were not good enough to make a comparison with any theoretical calculations.

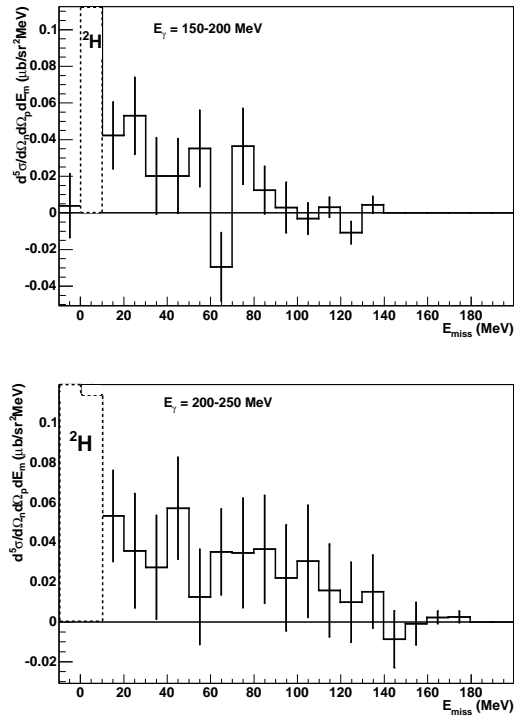


Figure 6.9: Cross section as function of the missing energy for $E_\gamma = 150-200$ MeV (upper panel) and $E_\gamma = 200-250$ MeV (lower panel) for the present experiment.

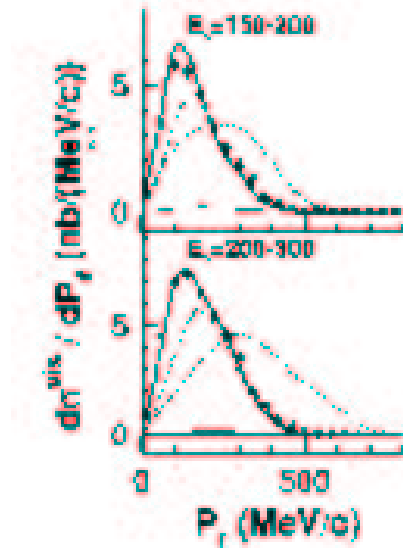


Figure 6.10: Cross section as function of the recoil momentum for the ${}^{12}\text{C}(\gamma, \text{pn}){}^{10}\text{B}$ reaction for photon energies 150-200 MeV and 200-300 MeV, in a back-to-back kinematics and for $E_m \leq 40$ MeV [74]. The solid line is a Monte Carlo simulation of the direct 2N knock-out, the dotted line a 2N knock-out phase space model, the dot-dashed line is the total cross-section from VM calculations, the dashed line is only the direct 2N knock-out from VM. The VM predictions have been multiplied by a factor of 0.5.

6.4 ${}^6\text{Li}(\gamma, \pi^+){}^6\text{He}$ reaction

The ${}^6\text{Li}(\gamma, \pi^+){}^6\text{He}$ reaction was investigated during the same beam-time as the present experiment. Pions were detected in the Germanium hodoscopes and the energy of the photons were determined using the microscope. The missing energy for this reaction is:

$$E_m = E_\gamma + M_T - E_\pi - E_{rec} \quad (6.1)$$

where M_T is the mass of the target nucleus, E_π is the total energy of the outgoing pion and E_{rec} is the total energy of the recoil nucleus. Again for the calculation of the π^+ kinetic energy the 4.1 MeV kinetic energy of the μ^+ was taken into account. The ground state and the first excited state of 1.80 MeV of ${}^6\text{He}$ were of interest here. In Fig. 6.12 the missing energy for the detectors positioned at 100° , Obelix, and at 150° , Idefix, is shown. A background subtraction similar to the one described in section 5.2 was done; in this case the two dimensional time histogram is generated by the tagger time in coincidence with the Germanium time and the microscope in coincidence with the Germanium time. For the pion detected at 100° only one peak corresponding to the first excited state is visible. In the other kinematics, π^+ at 150° , the ground and the 1.80 MeV excited states were both populated. The mean

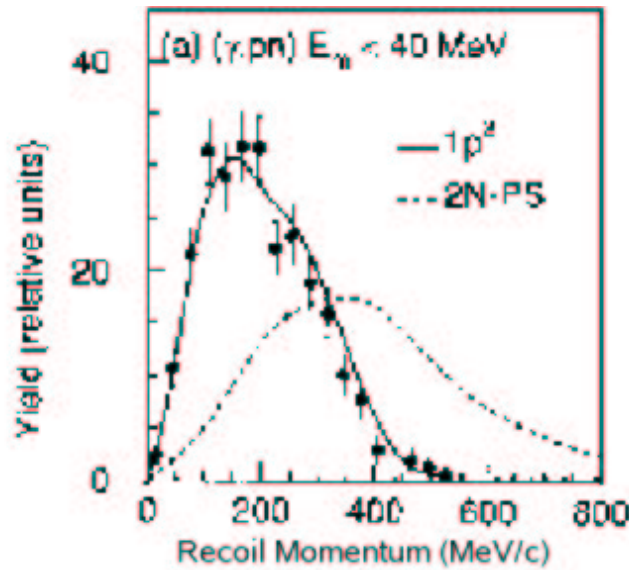


Figure 6.11: Recoil momentum distributions for the $^{12}\text{C}(\gamma, pn)^{10}\text{B}$ reaction at $E_\gamma = 200\text{--}400$ MeV and $E_m < 40$ MeV [73]. The curves are calculations based on direct 2N knock-out (solid) and on 2N knock-out phase space model (dashed).

values of Gaussian fits to the peaks were where they were expected to be and gave a missing energy resolution of 1.4 MeV FWHM which is close to the ~ 1 MeV required to separate the ^6He final states [55]. The events in the unphysical region belong to the background and are due mainly to interactions in the air. A line fitted to the background showed that it is flat. In the missing energy region above 1.86 MeV events from the excitation of continuum were fitted by a sloping line.

The differential cross section for the $^6\text{Li}(\gamma, \pi^+) ^6\text{He}$ reaction leading to the ground and 1.80 MeV states as a function of the pion detection angle is shown in Fig. 6.13. The cross section is normalised to the differential cross section for the $p(\gamma, \pi^+)n$ reaction measured with the CH_2 target. The result of this measurement are the black circles for the g.s. and the black triangles for the 1.80 MeV state. For comparison previous experimental points are also shown; the green inverted triangles and diamonds are from Shoda *et al.* [76] and the red I symbols are from Shaw *et al.* [77]. The lines are theoretical calculations of the reaction: the dashed and the long-dashed lines are calculations of DWIA using an harmonic oscillator (dashed) and a Wood-Saxon potential (long-dashed) [78], the solid line is a PWIA calculation based on cluster wavefunctions [79].

In Fig. 6.13 for the reaction leading to $^6\text{He}_{g.s.}$ there is a good agreement between all the data sets and the theoretical curves for forward angles up to 100° . The two points at the most backward angles of 120° and 150° of this measurement are a factor 5 higher than the point from Shaw *et al.*. This disagreement could be due to the different experimental method used in the experiment from Shaw *et al.* which

can be less reliable. Shaw *et al.* used the “End Point Technique” which showed no clear end point in the π^+ spectrum and an unexplained background [54]. At these backward angles there is also a disagreement between the different theoretical calculations indicating that the cross section is more sensitive to the radial extension of the halo nucleus. Therefore from the observation that the 120° and 150° points are also higher than the recent calculation in PWIA one can assume that either the ${}^6\text{He}$ halo nucleus has a larger radius than is presently assumed or the theoretical models do not work in this region, which corresponds to high momenta transfers.

Fig. 6.13 also shows the differential cross section for the ${}^6\text{He}$ 1st excited state compared to the results from Shoda *et al.*. The points are compared to theory: DWIA calculations based on Cohen-Kurath wavefunctions (published in [76]), solid line, and to a SM calculation phenomenologically adjusted to electron scattering data [80], dot-dashed line. The current data show an order of magnitude agreement with the previous data and no strong deviation from both the theoretical curves. There are no previous data sets and no theoretical calculation to compare the 120° and 150° pion detection angles with.

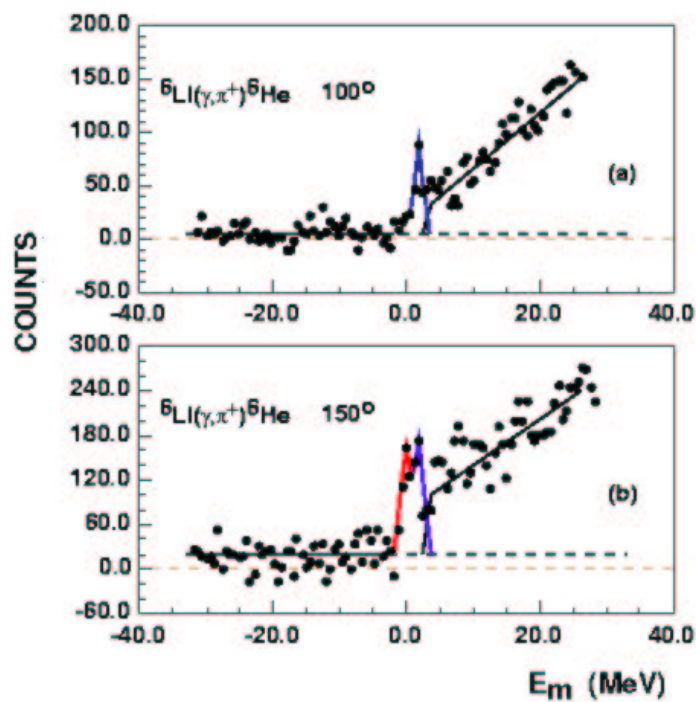


Figure 6.12: Missing energy distribution for the ${}^6\text{Li}(\gamma, \pi^+){}^6\text{He}$ reaction, for π^+ detected at 100° and at 150° . The red line is Gaussian fit to the ground state of ${}^6\text{He}$ and the blue line to the 1.8 MeV excited state. Background events below the ground state are fitted with a flat line while events in the continuum above 1.86 MeV are fitted with a sloping line.

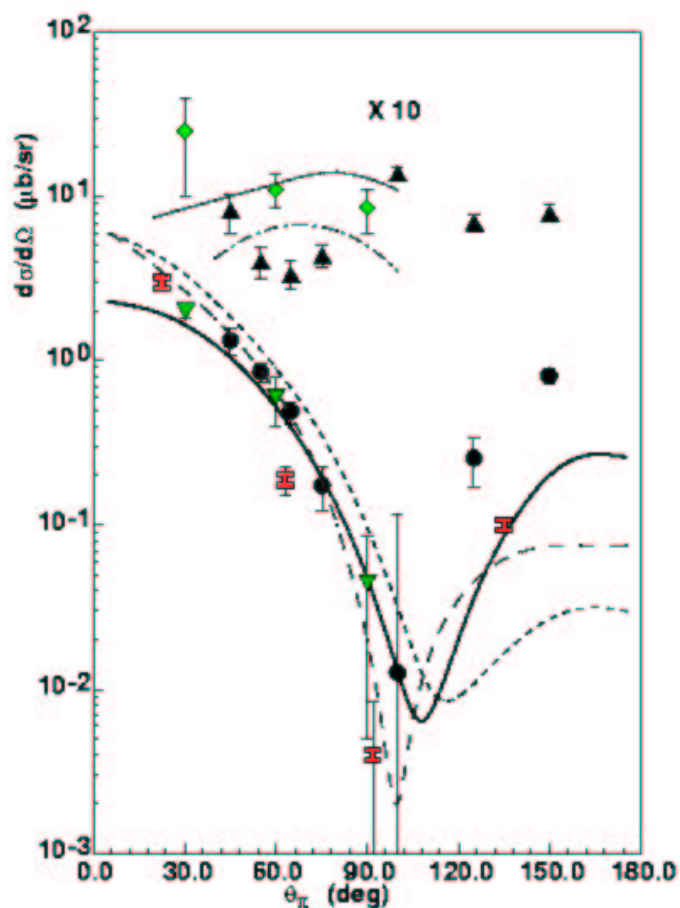


Figure 6.13: Differential cross section for the ${}^6\text{Li}(\gamma, \pi^+){}^6\text{He}$ reaction leading to the ground and 1st excited ($\times 10$) states. The black circles and triangles are the results of this measurement. The green inverted triangles and diamonds are the results of the previous experiment from Shoda *et al.* [76]. The red I symbols are experimental points from Shaw *et al.* [77]. The dashed curve is a DWIA calculation based on an harmonic oscillator [78] and the long-dashed curve based on an Wood-Saxon potential [78]. The solid curve use the results of recent PWIA calculations [79] done for this experiment. For the 1st excited state the solid curve are results from DWIA calculations based on Cohen-Kurath wavefunctions (published in [76]) and the dot-dashed curve from SM calculations [80].

Chapter 7

Conclusions and outlook

Measurements of the $^{16}\text{O}(\gamma, \text{NN})$ reactions were performed at MAMI in 2002 in collaboration with Mainz University, Glasgow University and Edinburgh University. These measurements were made in the real-photon (A2) experimental hall in conjunction with the Glasgow-Tübingen TOF detectors, the Glasgow tagged spectrometer and, for the first time, a new array of stacked Germanium detectors from Edinburgh. The goal of the experiment was to reach a high energy resolution, 2 MeV, to be able to resolve the different final states of the residual nuclei.

Germanium hodoscopes were chosen to replace the scintillator detector for proton detection used in the previous PiP-TOF experiments [62] because of their high intrinsic energy resolution. Unfortunately the combination of the tagger with the segmented Germanium detectors did not give the resolution in coincidence timing that was expected. Underestimation of the applied voltage and a short integration time, chosen to improve the events rate, lead to a energy and depth dependent Germanium detectors which eventually delivered a very poor time signal. This lead to the poor energy resolution of the measurement. The microscope, the tagged spectrometer with thinner scintillator fibres, improved the photon energy resolution of a factor 3 as explained in section 3.2.2 and reported in [52].

Missing energy distributions for the $^{16}\text{O}(\gamma, \text{pn})^{14}\text{N}$ reaction in back-to-back kinematics were plotted. Groups of states in ^{14}N could be resolved. The first excited state, 2.31 MeV (0^+), was not populated. This result is in agreement with the previous experimental results [17, 19]. The group of the ground state showed more strength than the group of the second and third excited states. The missing momentum distribution for the second group of ^{14}N final states, the 3.95 MeV (1^+) and the 7.03 MeV (2^+), showed a similar progression than in previous results [73].

Comparison with theoretical calculations were not made because of the poor statistics.

This first measurement with the new Edinburgh Germanium hodoscope did not work as well as was expected, it was not possible to resolve the separate excited

states in the residual ^{14}N nucleus as was planned but it was possible to confirm an older experimental observation. With the understanding of the problems of this measurement if a second run were made these problems could be addressed and the desired results achieved.

The double coincidence $^6\text{Li}(\gamma, \pi^+)^6\text{He}$ experiment, which was run in the same beam time as the (γ, NN) experiment, achieved a missing energy resolution good enough to be able to resolve the ground and the first excited state of the halo ^6He nucleus. Comparison of the differential cross section for backward pion-detection angles, 120° and 150° , to the most recent PWIA calculations [79] showed either a larger ^6He halo radius than what is presently assumed or that the theoretical models do not work in this region, which corresponds to high momentum transfer.

Bibliography

- [1] N.Bohr, Nature 137, 344 (1936)
- [2] C.F. von Weizsäcker, Z. Physik 96, 431 (1935)
- [3] O.Haxel *et al.*, On the “magic numbers” in nuclear structure, Phys. Rev. 75 (1949) 1766
- [4] M. Goeppert Mayer, On closed shells in nuclei, Phys. Rev. 75 (1949) 1969
- [5] H. Mütter, Exploring nucleon-nucleon correlations in (e,e'NN) reactions, 4th Workshop on “e-m induced Two-Hadron Emission”, Granada May 1999
- [6] L. Lapikas, Quasi-elastic electron scattering off nuclei, Nucl. Phys. **A553** (1993)
- [7] P.K.A. de Witt Huberts, Journ. Phys. **G16** (1990) 507
- [8] E. Quint, PhD. thesis, NIKHEF 1988
- [9] H. Mütter, A.Polls, Correlation derived from Modern Nucleon-Nucleon Potentials, Phys.Rev. C **61** (2000)
- [10] D. P. Watts *et al.*, Three-nucleon mechanisms in photoreactions, Phys. Lett. B **553** (2003) 25
- [11] K. Amir-Azimi-Nili *et al.*, Correlations and the Cross Section of Exclusive (e,e'p) Reactions for ¹⁶O, Nucl. Phys. **A625** (1997) 633
- [12] K.I. Blomqvist *et al.*, High-momentum components in the 1p orbitals of ¹⁶O, Phys. Lett. B **344** (1995) 85
- [13] D. Rohe, Habilitation Thesis, Universität Basel 2004
- [14] O. Benhar, A. Fabrocini, S. Fantoni and I. Sick, Spectral function of finite nuclei and scattering of GeV electrons, Nucl. Phys. A **579** (1994) 493.

- [15] K.I. Blomqvist *et al.*, The three-spectrometer facility at the Mainz microtron MAMI, Nucl. Instr. Meth. **A403** (1998) 263
- [16] L. Isaksson, Ph.D. thesis, Lund 1996
- [17] L. Isaksson *et al.*, pn -pair coupling in the (γ, pn) reaction at 72 MeV, Phys. Rev. Lett. 83 Number 16 (1999)
- [18] S. Cohen and D. Kurath, Two-nucleon transfer in the 1p shell, Nucl. Phys. **A141** (1970) 141
- [19] K.R. Garrow *et al.*, High resolution measurement of the $^{16}\text{O}(\gamma, pn)^{14}\text{N}_{0,1,2,\dots}$ reaction, Phys. Rev. C **64** (2001) 064602
- [20] G. Rosner, Investigation of short-range NN correlations via the $(e, e'pp)$ reaction, 4th Workshop on “e-m induced Two-Hadron Emission”, Granada May 1999
- [21] D.G. Middleton *et al.*, First measurements of the $^{16}\text{O}(e, e'pn)^{14}\text{N}$ reaction, Eur. Phys. J. A **29** (2006), 261-270
- [22] C. Giusti, H. Mütter, F. D. Pacati and M. Stauf, Short-range and tensor correlations in the $^{16}\text{O}(e, e'pn)$ reaction, Phys. Rev. C **60** (1999) 054608
- [23] J. Ryckebusch *et al.*, Tensor correlations in nuclei and exclusive electron scattering, Phys. Rev. C **61** (2000) 021603
- [24] S. Boffi, C. Giusti, F.D. Pacati and M. Radici, Electromagnetic response of atomic nuclei, Oxford Press 1996
- [25] C. Giusti *et al.*, Selectivity of the $^{16}\text{O}(e, e'pp)$ reaction to discrete final states, Phys. Rev. C **57** (1998) 1691
- [26] H. Feshbach, Ann. Phys. 5 (1958) and Ann. Phys. 19 (1962)
- [27] C. Giusti and F.D. Pacati, Two-proton emission induced by electron scattering, Nucl. Phys. **A535** (1991) 573
- [28] C. Giusti and F.D. Pacati, Photon-induced two-nucleon knockout reactions to discrete final states, Nucl. Phys. **A641** (1998) 297
- [29] S.C. Pieper *et al.*, Quantum Monte Carlo calculations of light nuclei, Eur. Phys. J. A13 (2002)
- [30] T.E.O. Ericson and W. Weise, Pions and nuclei, Clarendon Press, Oxford (1998)

- [31] P. Wilhelm, H. Arenhovel, C. Giusti and F. D. Pacati, Treatment of the Delta current in electromagnetic two-nucleon knockout reactions, *Z. Phys. A* **359**, 467 (1997)
- [32] C. Giusti and F.D. Pacati, Complete determination of scattering amplitudes and nucleon polarization in electromagnetic knockout reactions, *Nucl. Phys. A* **504** (1989) 685
- [33] W.J.W.Geurts *et al.*, Two-nucleon spectral function of ^{16}O at high momenta, *Phys. Rev. C* **54** (1996) 1144
- [34] H. Mütter and P. U. Sauer, *Computational Nuclear Physics*, edited by K. H. Langanke, J. A. Maruhn and S. E. Kaonin, Springer, New York, 1993
- [35] M. Schwamb, S. Boffi, C. Giusti and F. D. Pacati, On the NN-final-state-interaction in the $^{16}\text{O}(e,e'pp)$ reaction, *Eur.Phys.J. A* **17** (2003)
- [36] M. Schwamb, S. Boffi, C. Giusti and F. D. Pacati, NN final-state interaction in two-nucleon knockout from ^{16}O , *Eur. Phys. J. A* **20** (2004) 233
- [37] R. Machleidt, *The Meson Theory Of Nuclear Forces And Nuclear Structure*, *Adv. Nucl. Phys.* **19** (1989) 189.
- [38] R. B. Wiringa, R. A. Smith and T. L. Ainsworth, Nucleon Nucleon Potentials With And Without Delta (1232) Degrees Of Freedom, *Phys. Rev. C* **29** (1984) 1207.
- [39] J. Ryckebush *et al.*, Effects of the final-state interaction in (γ,pn) and (γ,pp) processes, *Nucl. Phys.* **A568** (1994) 828
- [40] J. Ryckebush *et al.*, Electroinduced two-nucleon knockout and correlations in nuclei, *Nucl. Phys.* **A624** (1997) 581
- [41] J. Ryckebush and W. Van Nespen, The $^{16}\text{O}(e,e'pp)^{14}\text{C}$ reaction to discrete final states, *Eur. Phys. J. A* **20** (2004) 435
- [42] T. Frick, PhD. thesis, Universität Tübingen 2004
- [43] T. Frick and H. Muther, A Self-Consistent Solution to the Nuclear Many-Body Problem at Finite Temperature, *Phys. Rev. C* **68** (2003) 034310
- [44] T. Frick, H. Muther and A. Polls, Sum rules and short-range correlations in nuclear matter at finite temperature, *Phys. Rev. C* **69** (2004) 054305
- [45] T. Frick, Kh.S.A. Hassaneen, H. Mütter and D. Rohe, Spectral function at high missing energies and momenta, *Phys. Rev. C* **70** (2004) 024309

- [46] A. Ramos, A. Polls and W.H. Dickhoff, Single-particle properties and short-range correlations in nuclear matter, Nucl. Phys. **A503** (1989) 1
- [47] H.Herminghaus, First operation of the 850 MeV C.W. electron accelerator "MAMI", Proceedings of the linear accelerator conference, NM, 1990
- [48] I. Anthony *et al.*, Designed of a tagged photon spectrometer for use with the Mainz 840 MeV microtron, Nucl. Instr. Meth. **A301** (1991) 230
- [49] S.J. Hall *et al.*, A focal plane system for the 855 MeV tagged photon spectrometer at MAMI-B, Nucl. Instr. Meth. **A368** (1996) 698
- [50] W.R. Leo, Techniques for nuclear and particle physics experiments, Springer-Verlag, 1994
- [51] A. Reiter, Internal report (The tagger microscope: an almost complete users guide), 2003
- [52] A. Reiter *et al.*, A microscope for the Glasgow photon tagging spectrometer in Mainz, Eur. Phys. J. A (2006)
- [53] K.Livinstong, HPGe strip detector setup, internal report 2002
- [54] ,A high resolution study of the Halo Nucleus ${}^6\text{He}$ using the reaction ${}^6\text{Li}(\gamma, \pi^+){}^6\text{He}$, N. Harrington, Ph.D thesis, University of Edinburgh 2005
- [55] D.Branford, The Ge6 array an array of stacked Ge detectors for high resolution photonuclear studies, 5th Workshop on electromagnetically induced two-hadron emission, Lund 2001
- [56] H.C. Walter *et al.*, PSI - Users's Guide - Accelerator Facilities, Paul Scherrer Institut 1994
- [57] R. A. Cecil, B. D. Anderson and R. Madey, Improved predictions of neutron detection efficiency for hydrocarbon scintillators from 1 MeV to about 300 MeV, Nucl. Instr. Meth. 161 (1979) 429
- [58] S. Cierjacks *et al.*, A large area position sensitive time-of-flight counter for energetic neutrons and charged particles, Nucl. Instr. Meth. **A238** (1985) 354
- [59] P. Grabmayr *et al.*, A high-resolution, large acceptance scintillation time-of-flight spectrometer, Nucl. Instr. Meth. **A402** (1998) 85
- [60] T. Hehl, P. Grabmayr, M. Sauer and G. J. Wagner, A Gain monitoring system for scintillation detectors using ultrabright LEDs, Nucl. Instrum. Meth. A **354** (1995) 505.

- [61] J.R.M. Annand *et al.*, ACQU a data acquisition and analysis system for medium energy physics experiments, Nucl. Instr. Meth. **A368** (1996) 385
- [62] F.A. Natter, Study of reaction mechanisms and short range correlations in two nucleon emission off ^3He using polarized photons, Ph.D. Thesis, Tübingen University, Germany (2001)
- [63] G. Charpak *et al.*, Location of the position of a particle trajectory in a scintillator, Nucl. Instr. Meth. **15** (1962) 323
- [64] I. Martin, Internal report 2/2003, Tübingen University
- [65] I. Martin, Internal report 1/2004, Tübingen University
- [66] W. Braunschweig *et al.*, A large area time-of-flight system with a resolution of 0.5 ns FWHM, Nucl. Instr. Meth. **134** (1976) 261
- [67] C. Kittel, Introduction to solid state physics
- [68] T. Hehl, Internal report 6/1996, Tübingen University
- [69] R. M. Edelstein *et al.*, Calibration of the neutron detection efficiency of a plastic scintillator 1 to 200 MeV, Nucl. Instr. Meth. **100** (1972) 355
- [70] R.A. Cecil *et al.*, Improved predictions of neutron detection efficiency for hydrocarbon scintillators from 1 MeV to about 300 MeV, Nucl. Instr. Meth. **161** (1979) 439
- [71] J.F. Ziegler, HYDROGEN, stopping powers and ranges in all elements (Pergamon Press)
- [72] F. Moschini, master degree thesis, Trento and Tübingen University, 2001 (<http://www.uni-tuebingen>)
- [73] P.D. Harty *et al.*, The contribution of 2N photon absorptio in $^{12}\text{C}(\gamma, 2N)$ reactions for $E_\gamma = 150\text{-}400$ MeV, Phys. Lett. B **380** (1996), 247
- [74] D.P. Watts *et al.*, The $^{12}\text{C}(\gamma, NN)$ reaction studied over a wide kinematic range, Phys. Rev. C **62** (2000), 014616
- [75] R.C. Carrasco, Inclusive (γ, N) , (γ, NN) and $(\gamma, N\pi)$ reactions in nuclei at intermediate energies, Nucl. Phys. **A570** (1994) 701
- [76] K. Shoda, O. Sasaki and T. Kohmura, Momentum Transfer Dependence Of Li-6 (γ, Pi^+) He-6 Cross-Sections, Phys. Lett. B **101** (1981) 124.
- [77] J. Shaw *et al.*, Measurement of $^6\text{Li}(\gamma, \pi^+)^6\text{He}_{g.s.}$ at 200 MeV, Phys. Rev. C **43** (1991), 1800

- [78] S. Karataglidis, P.J. Dortmans, K. Amos and C. Bennhold, Alternative evaluation of halo nuclei, *Phys. Rev. C* **61** (2000), 024319
- [79] S. Young, Ph.D. Thesis, University of Surrey, UK (2004)
- [80] J.C. Bergstrom, Electroexcitation of ${}^6\text{Li}$ with application to the reactions ${}^6\text{Li}(\pi^-, \gamma)_{1s} {}^6\text{He}(0^+, 2^+)$, *Phys. Rev. C* **21** (1980), 2496
- [81] N.P. Harrington *et al.*, Study of the halo nucleus ${}^6\text{He}$ using the ${}^6\text{Li}(\gamma, \pi^+) {}^6\text{He}$ reaction, to be published

Acknowledgments

First of all many thanks go to my supervisor Prof. Dr. Peter Grabmayr for his constant help and the many discussions about the experimental analysis and physics in general. Special thanks go to my analysis mate, Ingolf Martin, who was always ready to help me with the many questions I had about root and also to Dr. Torsten Hehl, whose knowledge and experience in the field was very helpful. I would like to thank Dr. Duncan Middleton, who shared the office with me in the last year and corrected most of the bad English of this thesis. I would also like to thank all the others who helped me with this work, Dr.'s Derek Branford, Nicholas Harrington, Daniel Watts and Klaus Föhl from Edinburgh, Dr.'s Douglas MacGregor, Cameron McGeorge, John Annand, Ken Livingston and the students Steven Waddell and Kris Monstad from Glasgow, the MAMI operators and all the people from the A2-collaboration in Mainz.

I particularly enjoyed my time at the Institut in Tübingen and outside together with the former Ph.D. students (now Dr. or almost) of the european graduate school Johannes Breitschopf, Larisa Pacearescu, Francesco Giacosa, Holger Denz, Arthur Erhardt, Olena Khakimova and Jochen Krimmer. Special thanks go to the "mädels" of the Edith-Stein Haus Isa, Moni, Sandy, Jenni and Sophie, who coloured my life in Tübingen and animated a lot of my evenings. I would like to thank Michael Schultze, Ludwig Niedermeier and David Moser for the nice coffee breaks combined with always nice conversations. For the Italian life style dinner, which would lift my mood, I have to thank Damiano and his gorgeous omelettes. I would also like to thank Elena, who, like me was "lost in translation", helped me a lot with the moments of homesickness. A very special thank goes to my best friend Emanuela, with whom I shared my happiness, my fears, my thoughts and with whom I learned how to be close without physically being there. My last thank goes to the man, whose constant encouragement and trust in me made me come to the point of writing the very last chapter of this work. Ti amo Burghard.

Lebenslauf

Federica Moschini
weiblich
geboren am 17.04.1975
in Cavalese (Trento), Italien
italienisch

Schulbildung

09/1981 - 06/1986 Grundschule in Trento (Italien)
09/1986 - 06/1989 Mittelschule in Trento (Italien)
09/1989 - 06/1994 Liceo scientifico L. Da Vinci in Trento (Italien), Abitur

Studium

09/1994 - 12/2001 Studium der **Physik**
an der Università degli Studi di Trento,
Facoltà di Scienze Matematiche Fisiche e Naturali, "Laurea in Fisica"
03/2000 - 09/2000 Erasmus Jahr an der Universität Tübingen
Diplomarbeit: *Two nucleon knock out by virtual photons*,
angefertigt am Physikalischen Institut der Universität Tübingen

Promotion

04/2002 Beginn der Dissertation "High resolution $^{16}\text{O}(\gamma, pn)^{14}\text{N}$ reaction at MAMI"
unter Prof. Dr. Peter Grabmayr Anleitung
an dem Physikalischen Institut der Universität Tübingen
12/2006 Ende

Akademischen Lehrer

- in Trento Prof. G. Anzellotti und Prof. M.P. Moschen - Analisi Matematica I
Prof. G. Vigna Suria - Geometria
Prof. M. Montagna und Prof. S. Oss - Fisica Generale I
Prof. P. Fornasini und Prof. G.A. Prodi - Esperimentazione di Fisica I
Prof. R. Leonardi und Prof. L. Vanzo - Fisica Generale II
Prof. F. Serra Cassano und S. Baldo - Analisi Matematica II
Prof. A. Fontana und Prof. O. Pilla - Esperimentazione di Fisica II
Prof. G. Guella und Prof. I. Mancini - Chimica generale ed inorganica
Prof. E. Pagani - Meccanica Razionale con elem. di meccanica statistica
Prof. S. Zerbini und G. Nardelli - Metodi matematici della fisica
Prof. M. Toller und G. Cognola - Istituzioni di fisica teorica
Prof. G. Orlandini und Prof. F. Dalfovo - Istituzioni di fisica nucleare
Prof. D. Bassi und R. Grisenti - Esperimentazione di fisica III
Prof. G. Viliani und C. Tosello - Struttura della materia
Prof. G. Orlandini und Prof. M. Traini - Fisica Nucleare
Prof. Ronchetti - Sistemi di elaborazione dell'informazione
Prof. I. Lazzizzera - Particelle elementari
Prof. A. Zecca und M. Scotoni - Laboratorio di fisica della materia
Prof. G. Lane - Inglese scientifico
- in Tübingen Prof. G. Orlandini, Lectures on Few-Body Systems
Prof. A. Fässler, Neutrinos in Cosmology, Astro, Particle, Nuclear Physics
I. Sick, Lectures on Electron scattering
P. Grabmayr, Femtophysik mit elektromagnetischen Sonden
R. Maier

List of publications

- High resolution $^{16}\text{O}(\gamma, NN)$ experiments at MAMI in Mainz, Proceeding of the “6th Workshop on electromagnetically induced two-hadron emission”, 2003
- First measurements of the $^{16}\text{O}(e, e'pn)^{14}\text{N}$ reaction, Eur. Phys. J. A **29** (2006), 261-270
- Study of the halo nucleus ^6He using the $^6\text{Li}(\gamma, \pi^+)^6\text{He}$ reaction, to be published

Conferences

- Annual seminars at the Workshops of the European Graduate School Basel-Tübingen „Hadronen im Vakuum, in Kernen und Sternen“
- Seminar at the “Student’s Workshop on the electromagnetic interaction” in Bosen, September 2002
- Poster at the DPG Spring Meeting in Tübingen, March 2003
- Invited talk at the “6th Workshop on electromagnetically induced two-hadron emission” at Pavia University, September 2003
- Participation at the DPG Spring Meeting in Köln, March 2004
- Participation at the “Nobel laureates meeting”, Lindau, June 2004
- Seminar on the occasion of the Evaluation of the European Graduate School Basel-Tübingen, January 2005